Werkstoffanwendungen im Maschinenbau

Band 41

Shufan Wang

Numerical Simulation of Rapid-Heating-Enhanced Densification and Grain Growth during Electric Current Assisted Sintering of Oxide Ceramics

Institut für Werkstoffanwendungen im Maschinenbau

RWTH AACHEN UNIVERSITY

Institut für Anwendungstechnik Pulvermetallurgie und Keramik an der RWTH Aachen e.V.

Herausgeber: Prof. Dr.-Ing. C. Broeckmann

Numerical Simulation of Rapid-Heating-Enhanced Densification and Grain Growth during Electric Current Assisted Sintering of Oxide Ceramics

Numerische Simulation der durch schnelles Aufheizen verbesserten Verdichtung und des Kornwachstums während des stromunterstützten Sinterns von Oxidkeramiken

Von der Fakultät für Maschinenwesen der Rheinisch-Westfälischen Technischen Hochschule Aachen zur Erlangung des akademischen Grades eines Doktors der Ingenieurwissenschaften genehmigte Dissertation

vorgelegt von

Shufan Wang

Berichter: Univ.-Prof. Dr.-Ing. Christoph Broeckmann

apl. Prof. Dr.-Ing. Martin Bram

Tag der mündlichen Prüfung: 13.05.2026

Diese Dissertation ist auf den Internetseiten der Universitätsbibliothek online verfügbar.

Werkstoffanwendungen im Maschinenbau
hrsg. von Prof. Dr.-Ing. Christoph Broeckmann

Band 41

Shufan Wang

Numerical Simulation of Rapid-Heating-Enhanced Densification and Grain Growth during Electric Current Assisted Sintering of Oxide Ceramics

Shaker Verlag
Düren 2026

Bibliographic information published by the Deutsche Nationalbibliothek
The Deutsche Nationalbibliothek lists this publication in the Deutsche Nationalbibliografie; detailed bibliographic data are available in the Internet at http://dnb.d-nb.de.

Zugl.: D 82 (Diss. RWTH Aachen University, 2026)

Copyright Shaker Verlag 2026
All rights reserved. No part of this publication may be reproduced, stored in a retrieval system, or transmitted, in any form or by any means, electronic, mechanical, photocopying, recording or otherwise, without the prior permission of the publishers.

Printed in Germany.

Print-ISBN	978-3-8191-0778-8
PDF-ISBN	978-3-8191-0815-0
ISSN	2195-2981
eISSN	2944-8573

Shaker Verlag GmbH • Am Langen Graben 15a • 52353 Düren
Phone: 0049/2421/99011-0 • Telefax: 0049/2421/99011-9
Internet: www.shaker.de • e-mail: info@shaker.de

Acknowledgment

The research presented in this dissertation was carried out during my time as a research assistant at the Institute for Materials Applications in Mechanical Engineering (IWM) at RWTH Aachen University. I am sincerely grateful to everyone who contributed to this work and supported me throughout my doctoral journey.

First and foremost, I would like to express my deepest gratitude to my supervisor, Prof. Christoph Broeckmann, for his continuous guidance, valuable comments on this dissertation, and steady support throughout my PhD. I am especially grateful for the trust and academic freedom he gave me. I would also like to thank Prof. Martin Bram for reviewing this dissertation and for the pleasant and long-standing collaboration in our joint research activities. My thanks also go to Prof. Johannes Schleifenbaum for chairing the examination committee and accompanying the doctoral procedure.

I am particularly grateful to Anke Kaletsch for her constant support and for always being helpful and approachable, especially in difficult situations. I would also like to express my special thanks to Yuanbin Deng, my group leader, for bringing me into this journey from my early time as a student assistant and for his comprehensive help throughout my doctorate. His advice and guidance have been invaluable to me.

I sincerely acknowledge the funding from the Deutsche Forschungsgemeinschaft (DFG, German Research Foundation) under the Priority Programme (SPP) 1959/2. I also take this opportunity to express my gratitude for the support of my research stay in the United States, which was a highly valuable experience for me both professionally and personally.

Furthermore, I would like to extend my warmest thanks to my dear colleagues for their friendship and professional support. I would like to thank Vanessa Gebhardt for her support with specimen preparation and Jiali Zhang for her assistance with microstructural characterization. I also want to thank my office colleagues, Chao Liu, Siyuan Qin, and Soheil Rooein, for creating such a warm and light-hearted working environment.

Finally, I would like to thank my parents in China for their unconditional love and support while I was studying abroad far from home. My heartfelt thanks go to my partner, Iven, for always believing in me, proofreading my work, helping me with programming and technical matters, and, above all, for always making time for me during the final stage of my PhD.

Aachen, May 2026 Shufan Wang

Abstract

Electric current assisted sintering (ECAS) is a promising powder consolidation technique that achieves short-term sintering with high heating rates. Currently, the main methods of performing ECAS are direct heating with current flowing through the powder compact and indirect heating of the powder compact in a conductive tool. Various influencing factors, such as ultra-high heating rate, extra-high temperature, and electric field, have been identified as contributors to rapid densification during ECAS. However, the dominant densification enhancing factor remains a subject of ongoing debate.

This work aims to understand the key influencing factors for the enhanced densification during ECAS of two oxide ceramics: 8 mol.% Y_2O_3 stabilized ZrO_2 (8YSZ) and strontium titanate ($SrTiO_3$). Two different heating modes—flash sintering (FS, direct heating) and ultrafast high-temperature sintering (UHS, indirect heating)—were investigated. A systematic comparative study of FS and UHS was conducted on 8YSZ to evaluate the roles of thermal and non-thermal effects. The results indicate that the ultra-high heating rate is the dominant factor driving rapid densification in both techniques for 8YSZ. This finding was further verified by UHS experiments on $SrTiO_3$.

Additionally, the finite element method (FEM) combined with a newly developed constitutive model was employed to predict the temperature distribution, densification, and grain growth of the samples. Electrical polarity-induced microstructural asymmetry was observed in 8YSZ during FS, with enhanced grain growth occurring in the anode region. This phenomenon was successfully modeled and simulated. Furthermore, the role of high heating rate in enhancing densification was analyzed for $SrTiO_3$ through modeling. The Skorohod-Olevsky Viscous Sintering (SOVS) model was modified to account for pore structure effect. The model's capability to predict densification during both conventional sintering and UHS was validated by experimental results of $SrTiO_3$. This finding demonstrates the correlation between the rapid-heating-induced unique porosity shape and the enhanced densification during UHS, providing deeper insights into the underlying mechanism of ECAS.

Zusammenfassung

Das stromunterstützte Sintern (Electric Current Assisted Sintering, ECAS) ist eine vielversprechende Technologie zur Konsolidierung von Pulvern, welches durch kurze Sinterzeiten und hohe Heizraten gekennzeichnet ist. Derzeit werden beim ECAS hauptsächlich zwei Verfahren angewandt: die direkte Erwärmung, bei der Strom durch einen Pulverpressling (Grünkörper) fließt, und die indirekte Erwärmung, bei der Pulver bzw. ein Pulverpressling in einem leitfähigen Werkzeug erhitzt wird. Verschiedene Einflussfaktoren wie ultrahohe Heizraten, besonders hohe Temperaturen und elektrische Felder wurden als treibende Kräfte für die schnelle Verdichtung während des ECAS identifiziert. Dennoch bleibt der dominante Mechanismus, der die Verdichtung maßgeblich beschleunigt, Gegenstand laufender Diskussionen.

Diese Arbeit zielt darauf ab, die wichtigsten Einflussfaktoren für die beschleunigte Verdichtung während des ECAS zweier Oxidkeramiken zu untersuchen: 8 mol.% Y_2O_3-stabilisiertes ZrO_2 (8YSZ) und Strontiumtitanat ($SrTiO_3$). Zwei verschiedene Heizmodi – Flash Sintering (FS, direkte Erwärmung) und Ultrafast High-Temperature Sintering (UHS, indirekte Erwärmung) – wurden dazu untersucht. Eine systematische Vergleichsstudie von FS und UHS wurde an 8YSZ durchgeführt, um die Beiträge thermischer und nicht-thermischer Effekte zu bewerten. Die Ergebnisse zeigen, dass die ultrahohe Heizrate der Schlüsselfaktor für die schnelle Verdichtung in beiden Verfahren für 8YSZ ist. Diese Erkenntnis wurde durch UHS-Experimente an $SrTiO_3$ weiter bestätigt.

Darüber hinaus wurde die Finite-Elemente-Methode (FEM) in Kombination mit einem neu entwickelten konstitutiven Modell eingesetzt, um die Temperaturverteilung, die Verdichtung und das Kornwachstum in den Proben vorherzusagen. Während des FS wurde in 8YSZ eine durch elektrische Polarität induzierte Mikrostrukturasymmetrie beobachtet, wobei ein verstärktes Kornwachstum im Anodenbereich auftrat. Dieses Phänomen wurde erfolgreich modelliert und simuliert. Darüber hinaus wurde die Rolle der hohen Heizrate bei der Förderung der Verdichtung für $SrTiO_3$ durch Modellierung analysiert. Das Skorohod-Olevsky Viscous Sintering (SOVS)-Modell wurde modifiziert, um die Wirkung der Porenstruktur zu berücksichtigen. Die Fähigkeit des Modells, die Verdichtung sowohl während des konventionellen Sinterns als auch des UHS vorherzusagen, wurde durch experimentelle Ergebnisse an $SrTiO_3$ validiert. Diese Ergebnisse zeigen die Korrelation zwischen der durch schnelles Aufheizen erzeugten einzigartigen Porenform und der verstärkten Verdichtung während des UHS und liefern tiefere Einblicke in die zugrunde liegenden Mechanismen des ECAS.

Table of Contents

Table of Contents ..... **I**

List of Figures ..... **V**

List of Tables ..... **XI**

Symbols and Abbreviations ..... **XIII**

1 Introduction **1**

2 Fundamentals and state of the art **5**

2.1 Sintering 5

2.1.1 Stages of sintering 6

2.1.2 Transport mechanisms during sintering 7

2.1.3 Simulation of sintering 10

2.2 Electric current assisted sintering (ECAS) 15

2.2.1 Fundamentals of ECAS 15

2.2.2 Densification enhancement mechanisms during ECAS 17

2.2.3 Flash sintering (FS) 21

2.2.4 Ultrafast high-temperature sintering (UHS) 26

2.2.5 Simulation of ECAS 28

2.3 Summary of fundamentals and state of the art 32

3 Motivation and objectives **35**

3.1 Motivation and research questions 35

3.2 Objectives 36

4 Materials **39**

4.1 8 mol.% yttria-stabilized zirconia (8YSZ) 39

4.2 Strontium titanate ($SrTiO_3$) 41

5 Experimental and numerical methods **43**

5.1 Sintering experiments 43

5.1.1 Flash sintering (FS) 43

5.1.2 Ultrafast high-temperature sintering (UHS) 45
5.2 Characterization methods 48
5.2.1 Microstructural characterization 48
5.2.2 Thermophysical characterization 48
5.3 Numerical modeling 50
5.3.1 Finite element modeling 50
5.3.2 Constitutive model 52
5.3.3 Constitutive model with pore shape impact 53
6 Experimental results 59
6.1 Experiments of 8YSZ 59
6.1.1 Thermophysical characterization 59
6.1.2 Sintering and microstructural characterization 60
6.1.3 Densification kinetics 67
6.1.4 Grain growth kinetics 69
6.1.5 Comparative study and interim summary 71
6.2 Experiments of $SrTiO_3$ 76
6.2.1 Sintering and microstructural characterization 76
6.2.2 Densification kinetics 78
6.2.3 Grain growth kinetics 79
6.2.4 Interim summary 80
7 Numerical results 83
7.1 Simulations of 8YSZ 83
7.1.1 Onset temperature of FS 83
7.1.2 Temperature distribution of FS 84
7.1.3 Densification and grain growth of FS 85
7.1.4 Temperature distribution of UHS 88
7.1.5 Densification and grain growth of UHS 89

7.1.6 Interim summary 93
7.2 Simulations of $SrTiO_3$ 94
7.2.1 Temperature distribution of UHS 94
7.2.2 Densification and grain growth of UHS 97
7.2.3 Interim summary 100
8 Summary and outlook 103
8.1 Summary 103
8.2 Outlook 105
9 References 107
10 Appendix 127
10.1 Thermophysical properties 127
10.2 Determination of densification kinetic parameters 133

List of Figures

Figure 2.1: Schematic overview of the pore structure evolution during different sintering stages [4]. 6

Figure 2.2: Transport mechanisms of sintering in two-sphere sintering model (E-C: evaporation-condensation; SD: surface diffusion; VD: volume diffusion; PF: plastic flow; GB: grain boundary diffusion) [4]. 7

Figure 2.3: The equilibrium shapes of the pores governed by the balance between the surface and interfacial energies (γs: surface energy, γb: grain boundary energy, θ: dihedral angle) [5]. 9

Figure 2.4: Schematic comparison of various sintering techniques in terms of sintering time and furnace temperature: The progression from conventional sintering (CS) to ultrafast high-temperature sintering (UHS) with a significant reduction in processing time (from hours to seconds) and furnace/mold temperature requirements (from ~2000°C to room temperature). 16

Figure 2.5: Schematic illustration of electric field-related mechanisms in ECAS: (a) Joule heating effect; (b) Frenkel defect generation; (c) phonon mode excitation; and (d) electrochemical reduction and blackening. Adapted from [59]. 17

Figure 2.6: Schematic illustration of heating rate-related mechanisms in ECAS: (a) low heating rates: increased pore rounding due to neck formation and delayed densification caused by surface diffusion; and (b) high heating rates: limited pore rounding with rapid densification via immediately activated grain boundary and volume diffusion. Adapted from [59]. 20

Figure 2.7: Schematic illustration of external pressure-related mechanisms in ECAS: (a) pressure enhanced mechanisms and (b) pressure induced mechanisms. Adapted from [59]. 21

Figure 2.8: (a) Schematic setup of a typical FS and (b) three stages during voltage-to-current flash experiment. 22

Figure 2.9: Onset of flash in different ceramics during constant heating rate experiments. The onset temperatures fall within a narrow power range, regardless of variations in the applied electric fields. The numbers above each curve denote the applied electric field in V/cm [86]. 24

Figure 2.10: Relationship between onset temperature and applied electric field for various dense polycrystalline and single crystal specimens of 3YSZ and 8YSZ [68]. 25

Figure 2.11: Schematic of a typical UHS setup with two carbon strips. 26

Figure 4.1: Scanning electron micrographs of the 8YSZ powders: (a) as-received condition and (b) after dispersing by ultrasonification for 3 min [137]. 39

Figure 4.2: Particle size distribution of the 8YSZ powder after ultrasonic treatment. 40

Figure 4.3: The fluorite crystal structure of 8YSZ [138]. 40

Figure 4.4: Powder characterization of $SrTiO_3$: (a) the scanning electron micrograph and (b) the size distribution. 41

Figure 4.5: The crystal structure of $SrTiO_3$ perovskite compound [142]. 41

Figure 5.1: (a) Schematic diagram of the experimental setup of FS (Source: Tarini Prasad Mishra, Forschungszentrum Jülich, 2020, personal communication) and (b) specimen geometry of dog-bone shaped sample. 43

Figure 5.2: (a) The custom made UHS apparatus used in this study; (b) schematic diagram of the UHS experimental setup and specimen geometry [76]... 45

Figure 5.3: Simulation model with defined boundary conditions for (a) FS setup and (b) UHS setup. 51

Figure 5.4: 2D scheme of pore structure with minimal and full spheroidization. 54

Figure 6.1: Thermophysical properties of 8YSZ as a function of temperature with (a) the coefficient of thermal expansion (CTE), (b) specific heat capacity, and (c) thermal conductivity at different relative densities (RD). 59

Figure 6.2: Young's modulus of 8YSZ as a function of temperature. 60

Figure 6.3: Experimental results for CS of 8YSZ: (a) sintering shrinkage and RD as a function of time; (b) sintering trajectory at different sintering temperatures and with different dwell times. The dwell time (min) is indicated by the number at each colored point. 61

Figure 6.4: Grain sizes of 8YSZ samples sintered by CS at temperatures ranging from 1300°C to 1450°C and dwell times of 0, 12, 30, and 60 min. 61

Figure 6.5: Microstructural evolution of 8YSZ samples conventionally sintered at 1350°C for (a) 0 min, (b) 12 min, (c) 30 min, and (d) 60 min. 62

Figure 6.6: RD of flash-sintered 8YSZ samples: (a) RD as a function of current density; and (b) RD as a function of temperature. The temperatures are simulated average temperatures of the gauge sections of the dog-bone samples during the isothermal period..... 63

Figure 6.7: Grain size analysis for flash-sintered 8YSZ samples: (a) schematic representation of the measured positions of the gauge section (15 mm) of dog-bone shaped samples; (b) microstructure at position A (near anode) of the sample flash sintered at 125 mA/mm² for 30 s; (c) grain sizes at position A, B, and C (corresponding to the positions on the dog-bone sample) at different current densities for the dwell time of 30 s; (d) microstructure at position C (near cathode) of the sample flash-sintered at 125 mA/mm² for 30 s..... 64

Figure 6.8: Experimental results of RD of UHS-sintered samples at different maximum currents and dwell times. Pre-sintered green bodies had a RD of 45% ± 2%. The top axis indicates the simulated average temperatures of the samples..... 65

Figure 6.9: Grain sizes of 8YSZ samples sintered by UHS at maximum currents between 11–13 A and dwell times between 30–120 s..... 66

Figure 6.10: SEM micrographs of the UHS-sintered 8YSZ samples at the maximum currents of 11 A, 12 A, and 13 A for 120 s in argon atmosphere..... 66

Figure 6.11: Parameter identification for densification: Determination of parameter m and the apparent activation energy of densification Qd for (a, d) conventional sintering (CS); (b, e) flash sintering (FS); and (c, f) ultrafast high-temperature sintering (UHS). 68

Figure 6.12: Determination of activation energy Qg for grain growth for (a) conventional sintering (CS) and (b) ultrafast high-temperature sintering (UHS)..... 70

Figure 6.13: Determination of activation energy Qg for grain growth for flash sintering (FS) near the (a) anode, (b) middle, and (c) cathode side of the sample during FS..... 70

Figure 6.14: Comparison of sintering trajectories of 8YSZ: (a) flash-sintered in air and UHS-sintered in argon; (b) conventionally sintered in air and UHS-sintered in argon. 71

Figure 6.15: (a) Uniaxial shrinkage and densification curves from dilatometer sintering of $SrTiO_3$ at the heating rate of 25 K/min, maximum temperature of 1500° C, and 1 min holding time in argon; (b) Relative density of the UHS-sintered samples as a function of the maximum current, with a 10 s holding time at the maximum current. The top axis indicates the simulated average temperature of the samples at each current. 76

Figure 6.16: Grain sizes of UHS-sintered $SrTiO_3$ samples at different maximum currents. The top axis indicates the simulated average temperature of the samples at each current. 77

Figure 6.17: SEM micrographs of UHS-sintered $SrTiO_3$ samples at different maximum currents [76]. 77

Figure 6.18: Parameter identification for densification: Determination of parameter Qb for CS of $SrTiO_3$. 79

Figure 6.19: Parameter identification for grain growth: Determination of parameter Qg for UHS of $SrTiO_3$. 80

Figure 7.1: Comparison of simulation results and experimental values from ref. [68] of the flash-onset temperatures of 8YSZ with respect to different electric fields. 84

Figure 7.2: Temperature simulation during FS: (a) mean temperature evolution for 25 mA/mm², 50 mA/mm², 75 mA/mm², and 100 mA/mm² with a dwell time of 120 s; (b) temperature distribution in the dog-bone sample sintered at 100 mA/mm² for 120 s, cut along its xy-symmetry plane. 85

Figure 7.3: Experimental and simulation results for (a) densification of CS at 1200°C, 1250°C and 1300°C for 2 h, (b) densification of FS at 25, 50, 75, and 100 mA/mm² with dwell times of 30, 60, and 120 s, (c) grain growth of CS at 1350°C, 1400°C, and 1450°C for 0, 12, 30, and 60 min and (d) grain growth of FS at 50, 75, 100, and 125 mA/mm² for 120 s. 86

Figure 7.4: Simulation results of flash-sintered samples at 100 mA/mm² for 120 s: (a) density distribution in the entire dog-bone sample; (b) grain size distribution in the half of dog-bone sample cut along its xy-symmetry plane. Position

A, B, and C indicate the locations where grain sizes were measured and analyzed, corresponding to the anode, center, and cathode, respectively. 87

Figure 7.5: Simulation results of a flash-sintered sample at 100 mA/mm² for 120 s with the partial reduction of the electrical resistivity near the cathode side: (a) density distribution in the entire dog bone sample and (b) grain size distribution in the half of dog-bone sample cut along its xy-symmetry plane. 88

Figure 7.6: (a) Simulated temperature distribution in the UHS setup at the maximum current of 13 A for 30 s, cut along the length of the carbon felt at the half-width position; and (b) experimental and simulation results of the stabilized temperatures on the surface of the carbon felt and those of the sample at different maximum currents..... 89

Figure 7.7: Optical image (top), simulation of RD distribution (middle), and simulation of temperature distribution (bottom) for UHS-sintered 8YSZ samples at 11 A for 120 s (left) and 13 A for 120 s (right)..... 91

Figure 7.8: (a) Comparison of simulation and experimental results of grain sizes of UHS-sintered 8YSZ samples at 11 A, 12 A, and 13 A. (b) Simulation result of grain size distribution in the UHS-sintered 8YSZ sample at 12 A for 120 s and the comparison between experimental and simulation results of the grain size at the position x, y, and z. 92

Figure 7.9: Experimental measurements and simulation results of the temperature inside the carbon felt and on the top surface of the felt during UHS at the maximum currents ranging from 5 to 24 A. At 12 A, the temperature inside the felt falls between the melting points (T_m) of Pt and Ni-Cr. At 16 A, the temperature inside the felt is higher than the T_m of Pt. 95

Figure 7.10: (a) Temperature evolution of the carbon felt (center of the inner surface) and $SrTiO_3$ samples (averaged over the entire pellet) during UHS at different maximum currents, as obtained from FEM simulation; and (b) comparison of optical images and simulation results for UHS-sintered $SrTiO_3$ samples at the maximum currents of 18 A and 24 A. The sample densified by UHS at 24 A has partially melted, whereas the samples densified at 18 A remains stable. 96

Figure 7.11: Densification of $SrTiO_3$ samples sintered by DIL and UHS at 18 A: experimental results vs. MATLAB simulation results using original SOVS model. 97

Figure 7.12: Simulation results of temperature and grain growth: (a) sample temperature evolution from FEM and grain growth calculated at 22 A; (b) comparison of experimental data and MATLAB simulation for grain sizes after the tests at maximum currents of 16, 18, 20, and 22 A. 98

Figure 7.13: MATLAB simulation results of densification by modified SOVS model for (a) UHS and (b) CS. 99

Figure 7.14: FEM simulation results using the modified SOVS model: (a) temperature distribution of UHS-sintered sample at 18 A before cooling; and (b) density distribution of the sample after UHS sintered at 18 A. 100

Figure 10.1 Determination of densification kinetic parameters for FS: (a) densification curve fitting and data extraction at 1000°C, 1100°C, and 1200°C; (b) extracted relative densites as function of dwell times; (c) determination of parameter m; (d) determination of paremter Qd. 133

List of Tables

Table 2.1: Material transport mechanisms in polycrystalline [5]..... 9

Table 5.1: Summary of experimental design for flash sintering (FS) and conventional sintering (CS) experiments of 8YSZ..... 45

Table 5.2: Summary of experimental design for ultrafast high-temperature sintering (UHS) and conventional sintering (CS) of 8YSZ..... 47

Table 5.3: Summary of experimental design for ultrafast high-temperature sintering (UHS) and conventional sintering (CS) of $SrTiO_3$ 47

Table 6.1: Comparison of conventional sintering (CS) and flash sintering (FS) at similar temperatures in air..... 73

Table 6.2: Comparison of conventional sintering (CS) and ultrafast high-temperature sintering (UHS) at similar temperatures in argon..... 73

Table 6.3: Summary of activation energy parameters used for simulations of 8YSZ 74

Table 6.4: Summary of activation energy parameters used for simulations of $SrTiO_3$ 80

Table 6.5: Comparison of CS and UHS of $SrTiO_3$ at similar sintering temperatures 81

Table 7.1: Comparison of simulation and experimental results of densification for UHS-sintered 8YSZ samples..... 90

Table 10.1 Temperature dependent properties of 8YSZ used in simulations: Specific heat, Young's modulus, and the coefficient of thermal expansion (CTE) 127

Table 10.2 Temperature dependent properties of 8YSZ used in simulations: Thermal conductivity and elctrical conductivity [157]. Thermal conductivity is also density dependent, and both property data above 900°C are extrapolated from the values below 900°C. 128

Table 10.3 Temperature dependent properties of $SrTiO_3$ used in simulations: Thermal conductivity and specific heat [150,151]. The thermal conductivity data above 900°C are extrapolated from the values below 900°C. 129

Table 10.4 Temperature dependent properties of carbon felt used in simulations: Specific heat [147], thermal conductivity [146], and electrical conductivity.

The electrical conductivity was experimentally measured using UHS test runs without any sample at the maximum currents ranging from 5 to 24 A, and the temperatures were estimated through pyrometer and thermocouple measurements..... 130

Table 10.5 Temperature dependent properties of Cu used in simulations: Thermal conductivity and specific heat [148,149] 131

Symbols and Abbreviations

Symbols

A	[1/sPa^n]	creep law deformability term
a	[-]	fitting constant
b	[-]	fitting constant
C_{s1}	[-]	material constant for viscosity
C_{s2}	[-]	material constant for viscosity
c_p	[J/kgK]	specific heat capacity
D	[m^2/S]	diffusion coefficient
f	[-]	porosity factor
G	[m]	grain size
G_e	[Pas]	effective shear viscosity
H	[-]	numerical constant
K	[-]	rate constant
K_0	[-]	pre-exponential constant
K_{1-4}	[-]	numerical constant
K_e	[Pas]	effective bulk viscosity
k	[J/K]	Boltzmann constant
m	[-]	density exponent
m_0	[-]	grain size exponent
N_s	[-]	density exponent
n	[-]	density exponent
n_0	[-]	stress exponent
p	[-]	grain growth exponent
Q_b	[kJ/mol]	activation energy for grain boundary diffusion
Q_d	[kJ/mol]	apparent activation energy for densification
Q_g	[kJ/mol]	activation energy for grain growth

$\dot{q}_{cond}$	[W/m^2]	surface heat flux due to conduction
$\dot{q}_{conv}$	[W/m^2]	surface heat flux due to convection
$\dot{q}_e$	[W/m^2]	rate of electrical energy due to Joule heating
$\dot{q}_{rad}$	[W/m^2]	surface heat flux due to radiation
R	[J/molK]	gas constant
r	[-]	density exponent
$\bar{r}$	[m]	effective pore radius
S	[m^2]	surface area
T	[K]	absolute temperature
t	[s]	time
T	[m^3]	volume

Greek letters

α	[m^2/s]	thermal diffusivity
γ_b	[J/m^2]	grain boundary energy
γ_s	[J/m^2]	surface energy
δ_{ij}	[-]	Kronecker delta
$\dot{\varepsilon}_{ij}$	[1/s]	strain rate tensor
$\dot{\varepsilon}_{kk}$	[1/s]	the first invariant of the strain rate tensor
$\dot{\varepsilon}_{eq}$	[1/s]	equivalent strain rate
$\dot{\varepsilon}_z$	[1/s]	axial strain rate tensor component
η_0	[Pas]	shear viscosity of the fully dense material
θ	[°]	dihedral angle
λ	[W/mK]	thermal conductivity
ξ	[-]	correction factor
ρ	[-]	relative density
ρ_0	[-]	initial relative density
ρ_c	[-]	critical relative density

ρ_v	[kg/m^3]	density of the control volume
σ_{eq}	[N/m^2]	equivalent stress
σ_{ij}	[N/m^2]	stress tensor
σ_m	[N/m^2]	hydrostatic stress
σ'_{ij}	[N/m^2]	deviatoric stress tensor
σ_s	[N/m^2]	effective sintering stress
σ_z	[N/m^2]	externally applied stress
ϕ	[-]	stress intensification factor
φ	[-]	normalized shear viscosity modulus
ψ	[-]	normalized bulk viscosity modulus

Abbreviations

AC	Alternating Current
AFM	Atomic Force Microscopy
CRFS	Current-Rate Flash Sintering
CS	Conventional Sintering
CTE	Coefficient of Thermal Expansion
DC	Direct Current
DEM	Discrete Element Modeling
DFT	Density Functional Theory
DIL	Dilatometer
DSC	Differential Calorimeter
ECAS	Electric Current Assisted Sintering
FAST	Field-Activated Sintering Techniques
FAST/SPS	Field-Assisted Sintering Technology/Spark Plasma Sintering
FEM	Finite Element Method
FIB	Focused Ion Beam
FS	Flash Sintering

FSPS	Flash Spark Plasma Sintering
GDC10	10 mol.% Gadolinium-Doped Ceria
GDC	Gadolinium-Doped Ceria
kMC	kinetic Potts Monte Carlo
LFA	Laser Flash Analysis
MC	Monte Carlo
MD	Molecular Dynamics
MSC	Master Sintering Curve
MWS	Microwave Sintering
NTC	Negative Temperature Coefficient
PF	Phase Field
RD	Relative Density
SEM	Scanning Electron Microscopy
SCF	Shrinkage-Rate Controlled Flash
SOFC	Solid Oxide Fuel Cell
SOVS	Skorohod-Olevsky Viscous Sintering
$SrTiO_3$	Strontium Titanate
UHS	Ultrafast High-Temperature Sintering
YSZ	Yttria-Stabilized Zirconia
Y_2O_3	Yttrium oxide
ZrO_2	Zirconia
3YSZ	3 mol.% Yttria-Stabilized Zirconia
8YSZ	8 mol.% Yttria-Stabilized Zirconia

1 Introduction

The increasing global demand for energy, and the urgent need to address climate change and reduce carbon footprints, have placed significant demand on industries to develop energy-efficient and sustainable technologies. High performance ceramic materials, such as 8 mol.% yttria-stabilized zirconia (8YSZ) and strontium titanate ($SrTiO_3$), play pivotal roles in enabling such technologies. 8YSZ is widely used in solid oxide full cells (SOFCs), which provide a clean and efficient technology for converting electrochemical energy to generate electricity and heat. $SrTiO_3$ has great potential for applications in environmental remediation, renewable energy generation and valuable chemical production from greenhouse gas conversion. However, processing these materials presents major challenges. Conventional sintering techniques for these oxide ceramics typically require extremely high temperatures (often exceeding 1400°C) and prolonged dwell times, resulting in significant energy consumption and high production costs. This energy-intensive approach not only increases the economic burden but also contributes to higher greenhouse gas emissions, making the development of more efficient processing methods a pressing need.

In response to these challenges, advancements in sintering technologies have focused on reducing energy consumption and processing times without compromising material properties. Among these, electric current assisted sintering (ECAS) has emerged as a promising technique for the rapid consolidation of ceramics. ECAS refers to “a class of consolidation methods in which mechanical pressure is combined with electric and thermal fields to enhance interparticle bonding and densification” [1]. Field-assisted sintering technology/spark plasma sintering (FAST/SPS) is a widely used ECAS technique that applies mechanical pressure in combination with Joule heating to achieve rapid densification. However, recent developments in ECAS have introduced sintering methods that do not rely on external pressure, such as flash sintering (FS) and ultrafast high-temperature sintering (UHS). FS utilizes high electric fields to achieve rapid densification within a few seconds at low furnace temperatures [2]. UHS, a recently developed novel sintering technique [3], achieves extremely high heating rates (up to 10^4 K/min) by direct contact of the sample to electrically heated thin carbon strips, enabling high temperature sintering (up to 3000°C) and full densification in seconds. While these techniques have demonstrated remarkable potential, understanding the mechanisms behind their enhanced densification remains challenging due to the interplay of multiple physical fields and the instantaneous nature of ECAS, which limits real-time experimental observations.

Multiphysics simulations based on the finite element method (FEM) provide a robust framework for analyzing the complex processes involved in ECAS. They are particularly suitable for modeling the coupled thermal, electrical, and structural interactions that occur during sintering. FEM simulations enable the prediction of critical parameters, such as temperature evolution, current density distribution, densification behavior, and grain growth, under the unique conditions of ECAS. Although numerous simulation studies of ECAS have been conducted in the past decade, most research has concentrated on pressure-assisted techniques with moderate heating rates, such as FAST/SPS. For ultrafast ECAS techniques like FS and UHS, simulations have largely been limited to analyzing temperature and current density distributions. To model the densification and grain growth, particular constitutive equations need to be implemented in FEM software, such as ABAQUS and COMSOL Multiphysics. Furthermore, developing more sophisticated models that incorporate the influence of key influencing factors, such as external pressure, ultra-high heating rates, and electric fields, remains essential.

This dissertation aims to study the mechanisms driving enhanced densification during ECAS, specifically focusing on FS and UHS. Two oxide ceramics, 8YSZ and $SrTiO_3$, were selected for sintering experiments. Comparative studies of various sintering techniques were systematically conducted to evaluate the contributions of thermal effects (e.g., ultra-high heating rate) and non-thermal effects (e.g., electric field). Multiphysics simulations were conducted to model temperature evolution during FS and UHS, forming the basis for analyzing sintering kinetics. Constitutive models incorporating a grain growth law were implemented in the FEM simulations to predict densification and grain growth. Furthermore, the model was modified to account for the impact of ultra-high heating rate on porosity structure, providing valuable insights into the mechanisms of ECAS through theoretical modeling.

This dissertation is organized into eight chapters. Following this introduction, Chapter 2 provides a detailed review of the fundamental principles of sintering and the advancements in ECAS technologies. The simulation methods of different sintering techniques are also summarized. Drawn from the state of the art, the motivation, research questions and objectives are presented in Chapter 3. In Chapter 4, a brief introduction of the studied materials, including their general properties and the characterization of the starting powders is given. Chapter 5 outlines the experimental and numerical methodologies employed in this study, including material preparation, sintering setups, and modeling approaches. Chapter 6 presents the results of different sintering experiments for both materials, with a focus on the analysis of densification and grain growth kinetics. The

thermal and non-thermal effects are evaluated in this Chapter. Chapter 7 discusses the FEM modeling results for 8YSZ and $SrTiO_3$, analyzing temperature distribution, densification and grain growth. It also explores the role of ultra-high heating rate in influencing pore shape and densification during sintering through modeling. Finally, Chapter 8 concludes the dissertation by summarizing the key findings and proposing directions for future research in ECAS technologies.

2 Fundamentals and state of the art

2.1 Sintering

Sintering is a manufacturing process used to create solid objects from powdered materials. It plays an essential role in materials engineering, especially in the manufacturing of ceramics. Sintering is defined as “a thermal treatment for bonding particles into a coherent, predominantly solid structure via mass transport events that often occur on the atomic scale” [4]. This bonding results in changes to the microstructure and enhanced strength. Understanding the theoretical foundations of sintering is central to optimizing this process for improved performance and greater manufacturing efficiency.

The driving force for sintering is the reduction of free energy of the system. Sintering lowers the system energy primarily through the reduction of surface energy. As particles sinter, the system seeks to minimize the total surface area, which corresponds to high energy states. This reduction in surface area can be induced by three main factors: the curvature of the particle surfaces, externally applied pressure, and chemical reactions. The curvature of particle surfaces is associated with the Laplace pressure, which is inversely proportional to the radius of curvature of these interfaces. Smaller particles or those with irregular shapes have higher curvatures and thus higher Laplace pressures, which leads to accelerated diffusion rates and densification. In the case of the application of external pressure, the contribution of surface curvature becomes insignificant, and the pressure provides the major driving force for sintering. Chemical reactions can also drive the sintering process. However, in practice, they are rarely used deliberately to enhance densification in advanced ceramics because controlling the microstructure becomes challenging when a chemical reaction occurs concurrently with sintering [5].

Depending on specific materials and applications, sintering processes are commonly classified into different categories. One common sintering method is solid-state sintering, during which the material is heated to a temperature between approximately 50% and 80% of its melting temperature. Both mixed-phase and single-phase materials can be sintered in the solid state. The bonding of particles and the reduction of porosity during solid-state sintering occur through atomic diffusion. For many ceramic materials, achieving the required density or microstructure of the final product through solid-state sintering can be challenging, or the necessary sintering temperature is too high for the practical fabrication process. To address these limitations, one approach is to introduce an additive that forms a minor liquid phase between particles or grains at the sintering temperature. This technique, known as liquid-phase sintering, enhances densification by providing a high-

diffusivity pathway for matter transport into the pores. Another solution to the inadequate densification is pressure-assisted sintering. At lower pressure, densification is controlled by diffusional creep, whereas higher pressure induces plastic flow. For non-crystalline material, such as amorphous glasses, viscous sintering is the common sintering process where mass transport occurs predominately via viscous flow. [4,5]. Each of these methods has distinct mechanisms and applications, tailored to overcome specific challenges in the sintering process. The sintering theory and modeling methods elaborated in this work are specifically focused on solid-stage sintering.

2.1.1 Stages of sintering

Solid-state sintering typically progresses through three sequential stages: the initial stage, the intermediate stage, and the final stage. In certain analyses, an additional preliminary stage, often referred to as stage 0, is considered. Stage 0 describes the instantaneous point contact between particles that occurs when the powders are initially mixed and poured into the die [5]. **Figure 2.1** illustrates the sintering stages, transitioning from a loose powder configuration to a structure characterized by isolated and almost spherical pores [4].

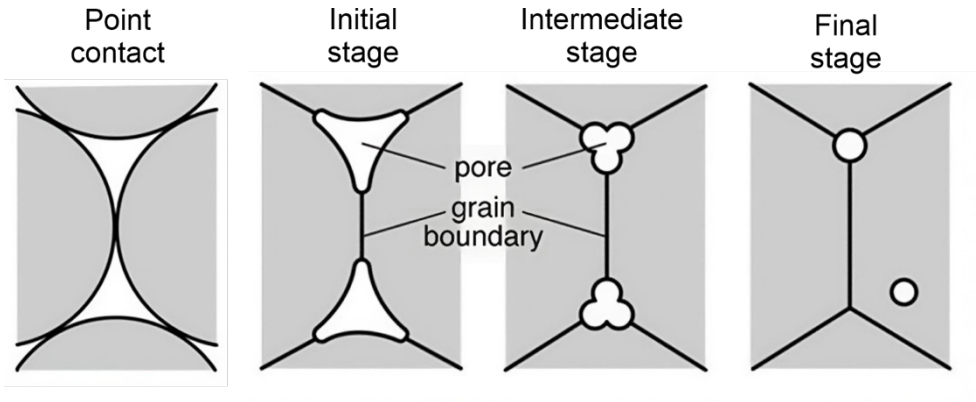

Figure 2.1: Schematic overview of the pore structure evolution during different sintering stages [4].

During initial stage sintering, the necks at the sinter bond form and grow from the initial single point contact. The pores maintain a concave shape with sharp edges, and mass transport is primarily restricted to surface diffusion due to the relatively low temperature, resulting in minimal shrinkage and more surficial necking. Depending on the initial packing and the characteristics of the powder, the density during the initial stage can reach up to 65% of the theoretical density.

In the intermediate stage, the necks formed during the initial stage continue to grow, leading to a decrease in pore volume and smoother pore shapes. Prominent diffusion takes place during this stage, causing the particles' centers of mass to move closer together, which results in substantial densification. The relative density achieved in the intermediate stage

is 65–90%. Larger necks start to form a network of cylindrical pores that eventually closes up as the density exceeds 90%, signaling the onset of the final stage.

During final stage sintering, the cylindrical pores pinch off and form spherical pores at the grain corners. As the pore spheroidization process reaches its end, open porosity is converted into closed porosity. This stage is characterized by significant grain growth and the elimination of most remaining porosity. The densification rate slows significantly as the coarsening events hinder further densification. Diffusion mechanisms in this stage include both grain boundary and volume diffusion, with the material approaching its theoretical density.

2.1.2 Transport mechanisms during sintering

Sintering of polycrystalline materials takes place through diffusional transport of matter along specific paths that define the sintering mechanisms. During the sintering process, mass is transported from regions with higher chemical potential (the source) to regions with lower chemical potential (the sinks). As sketched in **Figure 2.2**, the transport mechanisms during sintering can be broadly classified into surface transport mechanisms (non-densifying mechanism) and bulk transport mechanisms (densifying mechanism).

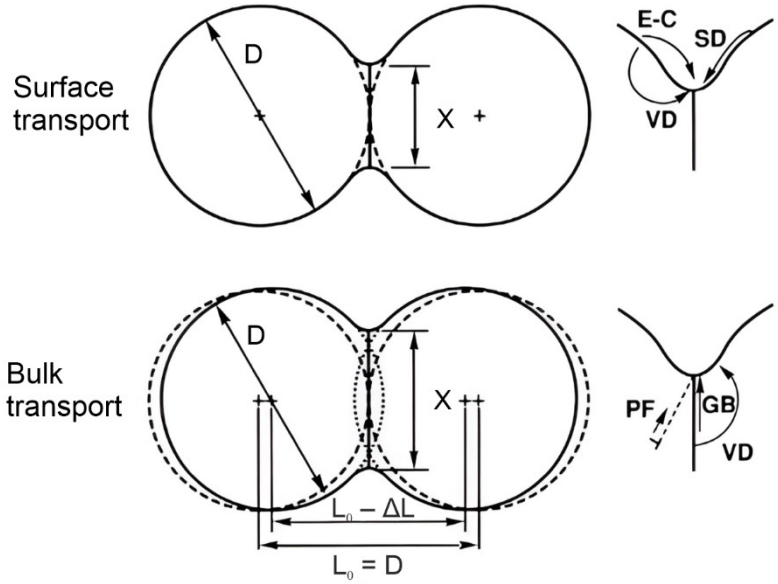

Figure 2.2: Transport mechanisms of sintering in two-sphere sintering model (E-C: evaporation-condensation; SD: surface diffusion; VD: volume diffusion; PF: plastic flow; GB: grain boundary diffusion) [4].

Surface transport mechanisms include surface diffusion, evaporation–condensation, and volume diffusion from the surface to the sinter neck. These mechanisms contribute to neck growth without changing particle spacing and thus result in no densification. In contrast,

grain boundary diffusion, volume diffusion from the grain boundary to the pore, and plastic flow by dislocation motion are categorized as bulk transport mechanisms. These mechanisms facilitate both neck growth and the approach of the two particles, leading to densification.

Surface transport processes normally occur in the early stages of sintering. Surface diffusion and evaporation-condensation are the two primary mechanisms involved in surface-transport-controlled sintering. In the evaporation-condensation mechanism, atoms or molecules evaporate from the surface, travel through the vapor phase, and eventually condense onto neighboring particle surfaces. This process is particularly significant in systems with high vapor pressures; otherwise, it plays a relatively minor role.

On the other hand, surface diffusion is an initial contributor to the sintering of nearly all materials. The activation energy for surface diffusion is generally lower than that for other mass transport processes because surface atoms have fewer neighboring atoms than those in the bulk of the lattice. As a result, surface diffusion initiates at lower temperatures compared to other sintering mechanisms. Since surface diffusion involves mass flow from surface sources to surface sinks without causing shrinkage, it is considered undesirable in systems where densification is required but advantageous when shrinkage is unfavorable. Rapid heating techniques are used to minimize the action of low-temperature surface diffusion when densification is desired. Most covalent ceramics undergo surface-diffusion-controlled sintering and require doping to achieve densification.

As sintering progresses, surface diffusion becomes less significant, and densification of crystalline materials occurs through bulk transport mechanisms such as grain boundary diffusion and volume diffusion. Vacancies migrate from the pores through the lattice or along grain boundaries, resulting in a reverse flow of mass into the pores. When vacancies migrate through a crystalline structure, it is called volume diffusion or lattice diffusion. The movement of vacancies from the neck surface through the particle interior, with subsequent emergence at the grain boundary, helps to reduce the surface energy of the system and leads to densification. When vacancies migrate along the grain boundaries of a material, it is called grain boundary diffusion. Due to the disordered atomic structure of the grain boundary, vacancies move more rapidly along grain boundaries than through crystal lattice. Thus, grain boundary diffusion has a generally higher rate than volume diffusion.

Although volume diffusion is active in most materials at high temperatures, it often does not dominate the mass transport process during sintering. The activation energy for grain boundary diffusion usually lies between the activation energies for surface and volume

diffusion. Consequently, interfacial diffusion processes (surface and grain boundary diffusion) are generally more active. **Table 2.1** summarizes different sintering mechanisms in polycrystalline solids, characterized by the source and the sink of material transport and their contributions to the densification or shrinkage.

Table 2.1: Material transport mechanisms in polycrystalline [5]

Sintering mechanism		Source of matter	Sink of matter	Densifying
Surface transport mechanisms	Evaporation-condensation	Surface	Neck	No
	Surface diffusion	Surface	Neck	No
	Volume diffusion	Surface	Neck	No
Bulk transport mechanisms	Volume diffusion	Grain boundary	Neck	Yes
	Grain boundary diffusion	Grain boundary	Neck	Yes
	Plastic flow	Dislocation	Neck	Yes

The sinter bond between the contacting particles is the critical region for mass transport and neck growth during sintering. It is the region where atoms are deposited to minimize surface energy. As the surface area (solid-vapor) decreases, the grain boundary area (solid-solid) increases. For sintering and neck growth to proceed, the change in the free energy of the system has to be negative. As soon as the neck size reaches an equilibrium state dictated by the solid-vapor dihedral angle θ, as illustrated in **Figure 2.3**, further neck growth relies on grain growth.

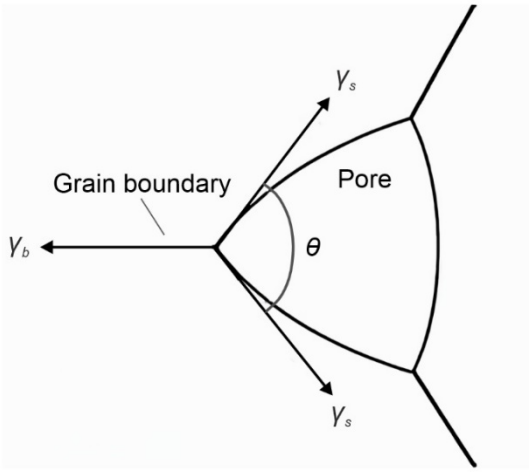

Figure 2.3: The equilibrium shapes of the pores governed by the balance between the surface and interfacial energies (γ_s: surface energy, γ_b: grain boundary energy, θ: dihedral angle) [5].

The dihedral angle describes the angle at which a grain boundary intersects at a pore. It is a geometric parameter that characterizes the equilibrium shape of pores and grains within the microstructure. Neck growth occurs until the surface energy, dihedral angle, and grain boundary energy reach a force equilibrium defined as:

$$\gamma_b = 2 \cdot \gamma_s \cdot \cos\left(\frac{\theta}{2}\right) \tag{2.1}$$

The equilibrium dihedral angle is material-dependent. In oxide ceramics, θ is typically greater than 120°. For most analytical calculations of mass transport during sintering, θ is assumed equal to 180° [5], which represents a circular cross-section of the pores with $\gamma_b = 0$. Understanding the equilibrium dihedral angle is crucial for predicting the kinetics of neck growth and the overall densification behavior during sintering.

2.1.3 Simulation of sintering

Numerical simulation is a powerful tool to understand and optimize sintering processes. It offers various benefits, such as insights into underlying mechanisms, cost-effectiveness, predictive capabilities, and multi-physics integration. Typically, the models developed over the last several decades fall into three categories based on the length scale of the simulations: atomic scale, microscopic scale, and macroscopic scale [6].

Atomic-scale simulation

At the atomic level, molecular dynamics (MD) simulations have been widely used for early stage sintering [7,8]. In this method, each particle is modeled as a cluster of numerous atoms or molecules, and the motion of each atom is tracked during the simulation of sintering processes. Newton's equations of motion are solved to calculate the atomic trajectories within a short time periods, typically less than a microsecond. MD simulations provide valuable mechanistic insights into the sintering process at the atomic scale, including atomic diffusion, grain boundary dynamics, and particle rearrangement. However, due to the substantial computational resources required, the simulations are restricted to small length scales (nanometers to micrometers) and short time scales (nanoseconds to microseconds).

Another method applicable at the atomic scale is density functional theory (DFT) [9,10]. It is a first-principles method that has also been used for sintering studies. DFT is a quantum mechanical modeling approach that calculates the electronic structure with high accuracy. It provides predictions of interatomic interactions, binding energies, and reaction pathways. By solving the Schrödinger equation within the framework of approximations like the local

density or generalized gradient approximations, DFT enables detailed investigations into atomic diffusion, surface energy variations, and defect dynamics during sintering. Furthermore, DFT-derived data can be used to parameterize microscale models, ensuring continuity across simulation scales.

Microscale simulation

Simulations at the microscopic level focus on predicting microstructural evolution during sintering. The properties and performance of the final sintered products are determined by various microscopic factors, including grain shape, grain size, particle arrangement, impurities, and porosity. In order to effectively analyze these factors and their influence on the sintering behavior, different modeling approaches have been developed based on the numerical techniques employed. Generally, microstructure-scale methods rely on the constructed free energy, thermodynamic driving force, or interactions between particles.

Discrete element modeling (DEM) is used to model the behavior of discrete particles, making it ideal for studying particle rearrangement and packing during sintering [11–13]. Monte Carlo (MC) simulations, on the other hand, employ stochastic techniques to model the evolution of microstructures during sintering [14–16]. MC methods are particularly useful for studying microstructural evolution, grain growth, and re-crystallization of polycrystalline materials, providing insights into the statistical nature of sintering and the kinetics of microstructural evolution. However, due to their discrete nature, MC methods lack physical correlations such as temporal resolution and continuous representation. To address some of these challenges, phase field (PF) modeling offers an alternative approach by using order parameters that vary continuously across the simulation domain to reflect microstructural evolution, thereby avoiding issues associated with discretization [17–19]. PF modeling is a mechanistic-based modeling method that provides a quantitative and material-specific framework for studying microstructural evolution. Additionally, PF models can easily incorporate multiple physical phenomena, such as diffusion, mechanical deformation, and chemical reactions. The continuous nature of the fields facilitates the coupling of these processes, leading to more comprehensive and accurate simulations. However, the continuous fields also demand significant computational resources and extensive parameter calibration, making the process both computationally and experimentally expensive.

Macroscale simulation

At the macroscopic level, constitutive laws or analytical expressions are developed to describe the macroscopic behavior of real sintering processes. Unlike microstructural

approaches, which aim for a general understanding of the underlying mechanisms rather than a precise description of actual sintering processes, macroscopic models provide a more practical advantage. By adjusting model parameters based on experimental data, these models can accurately predict the effective properties of the sintering process without necessarily considering the physical meaning behind every parameter.

One of the fundamental approaches at the macroscopic scale is the theoretical sintering kinetics model, which employs analytical or semi-empirical equations to characterize the sintering process at discrete stages. The model addresses individual mechanisms such as grain boundary diffusion, volume diffusion, and surface diffusion, which are dominant at various stages of sintering. Numerous analytical models have been proposed to describe sintering at the initial [20–22], intermediate [23–25], and final stages [23,26], respectively. To provide a continuous description across these stages, Hansen et al. [27] proposed a combined-stage sintering model that quantifies sintering as a continuous process from beginning to end. Building on this work, Su and Johnson [28] derived the master sintering curve (MSC) for free sintering conditions. The MSC defines sintered density as a unique function of the integral of a temperature function over time with the assumption that a single dominant diffusion mechanism controls densification during sintering. This method has found wide application in practical sintering processes due to its simplicity and effectiveness.

The concept in combined-stage sintering theories can also be extended to pressure-assisted sintering by introducing a unique porosity function, known as the stress intensification factor ϕ. This factor, defined as the ratio of the total external cross-sectional area of an element unit cell to its grain boundary area, quantifies how stress is distributed and amplified within the microstructure of the material. By incorporating this factor and assuming that the externally applied stress is much greater than the driving force due to surface curvature, the macroscopic strain rate under pressure-assisted sintering is defined as follows [5]:

$$\dot{\varepsilon}_z = -\frac{HD\phi^{n_0}{\sigma_z}^{n_0}}{G^{m_0}kT} \tag{2.2}$$

where H is a numerical constant, D is the diffusion coefficient, G is the grain size, k is the Boltzmann constant, T is temperature, and σ_z denotes the externally applied stress. The exponent n_0 and m_0 in this equation vary depending on the dominant creep mechanism: $n_0 = 1$, $m_0 = 2$ for volume diffusion; $n_0 = 1$, $m_0 = 3$ for grain boundary diffusion; $n_0 = 1$ or 2, $m_0 = 1$ for grain boundary sliding; and $n_0 > 3$, $m_0 = 0$ for dislocation-based creep.

Another approach at the macroscopic scale is the continuum mechanics model, which treats the sintering body as a viscoplastic continuum. This perspective, grounded in the theory of plastic deformation of porous bodies [29,30], allows for predicting the evolution of component shape driven by macroscopic parameters during sintering in addition to the sintering kinetics. The origins of the continuum-mechanics-based models trace back to the rheological theory of sintering established by Skorohod [31], which was later adapted by Olevsky to accommodate numerical simulations [32]. This development led to what is currently known as the Skorohod-Olevsky Viscous Sintering (SOVS) model. The model incorporates a set of constitutive laws that correlate the shrinkage of a porous body with its viscous parameters and the generalized state of stress.

In the SOVS model, the porous body is considered to be a medium composed of two material components: a core phase and a void phase. The core phase consists of particles characterized by a nonlinear viscous incompressible behavior, while the void phase is assumed to be homogeneously distributed within the porous body. The overall behavior of the porous body is considered isotropic. The macroscopic shrinkage of a porous body is described by relating an external load corresponding to the stress tensor σ_{ij} to the strain rate tensor $\dot{\varepsilon}_{ij}$ through a nonlinear viscous constitutive law, expressed as follows:

$$\sigma_{ij} = \frac{\sigma_{eq}}{\dot{\varepsilon}_{eq}}\left[\varphi\dot{\varepsilon}_{ij} + \left(\psi - \frac{1}{3}\varphi\right)\dot{\varepsilon}_{kk}\delta_{ij}\right] + \sigma_s\delta_{ij} \tag{2.3}$$

where σ_{eq} and $\dot{\varepsilon}_{eq}$ are the equivalent stress and strain rate, $\dot{\varepsilon}_{kk}$ is the first invariant of the strain rate tensor, which corresponds to the volumetric shrinkage rate. It can be expressed as the sum of tensor diagonal components: $\dot{\varepsilon}_{kk} = \dot{\varepsilon}_{11} + \dot{\varepsilon}_{22} + \dot{\varepsilon}_{33}$. φ and ψ are functions of porosity that characterize the normalized shear and bulk viscosity moduli of the porous compact. δ_{ij} is the Kronecker delta ($\delta_{ij} = 1$ if $i = j$ or $\delta_{ij} = 0$ if $i \neq j$), and σ_s is the effective sintering stress.

Although nonlinear viscous assumption may more accurately represent the actual sintering behavior, acquisition of modeling parameters from experiments is significantly more challenging compared to the linear viscous model. Therefore, a linear viscous assumption is often employed in the sintering process simulations [33,34]. Under this assumption, the relationship of linear viscosity in the SOVS model is given by $\sigma_{eq} = 2\eta_0\dot{\varepsilon}_{eq}$, where η_0 is the shear viscosity of the fully dense material. The inversion of Equation 2.3 provides the relationship between the inelastic component of the total strain rate and the deviatoric and hydrostatic stresses, as shown below:

$$\dot{\varepsilon}_{ij} = \frac{\sigma'_{ij}}{2G_e} + \frac{\sigma_m - \sigma_s}{3K_e}\delta_{ij} \tag{2.4}$$

For linear viscosity condition, $G_e = \eta_0\varphi$ is the effective shear viscosity, $K_e = 2\eta_0\psi$ is the effective bulk viscosity, and $\sigma_m = \sigma_{kk}/3$ is hydrostatic stress. The effective sintering stress σ_s is a function of the porous structure morphology and topology, with different formulations proposed by various authors [32,35,36]. Since both σ_s and the effective viscosity are grain-size dependent, a grain growth law is typically coupled with the constitutive model to account for grain size evolution during sintering [37,38].

The continuum mechanics model and its constitutive equations predict the density, grain size, stress field, and strain field of the compact throughout the entire sintering process, as well as the final shape and dimensions of the component. These models are commonly integrated with FEM to simulate the macroscopic behavior of the porous body during sintering, which is the main focus of this study.

2.2 Electric current assisted sintering (ECAS)

2.2.1 Fundamentals of ECAS

In recent decades, scientific research has focused on developing innovative sintering techniques characterized by reduced carbon footprint and energy consumption [39,40]. Promising approaches include the use of additional process control parameters like pressure [41–43], sintering aids [44,45], and electromagnetic fields [46–48]. Particularly noteworthy are filed-activated processes, such as microwave sintering (MWS) [48], flash sintering (FS) [2,49], and field-assisted sintering technology/spark plasma sintering (FAST/SPS) [50,51]. As suggested by Grasso et al. [1], the term “field” in field-activated techniques is attributed to any applied field, such as mechanical, electric, gravitational or electromagnetic. MWS utilizes electromagnetic field to heat the material volumetrically through molecular interactions, producing internal heat within the powder compact. FS forces an electric current through the green body and produces heat via Joule heating. FAST/SPS combines hot pressing with the application of electricity to generate heat in the graphite tool. Despite the absence of actual sparks or plasma [52,53], the term SPS is retained to distinguish this method from the broader category of field-activated sintering techniques (FAST). Recently, another novel sintering technique named ultrafast high-temperature sintering (UHS) was introduced [3] to further accelerate sintering process. UHS uses carbon strips that are connected to electrodes to heat the powder compact without current passing through the sample. A comparison between these advanced technologies and conventional sintering (CS) in terms of sintering time and furnace temperature is illustrated in **Figure 2.4**. The graph highlights the technological advancements in sintering aimed at reducing both sintering duration and the required thermal input. Besides the low furnace temperature and reduced sintering time, these advanced sintering techniques bring auxiliary benefits including fine grain size [54,55] and improved mechanical properties [56].

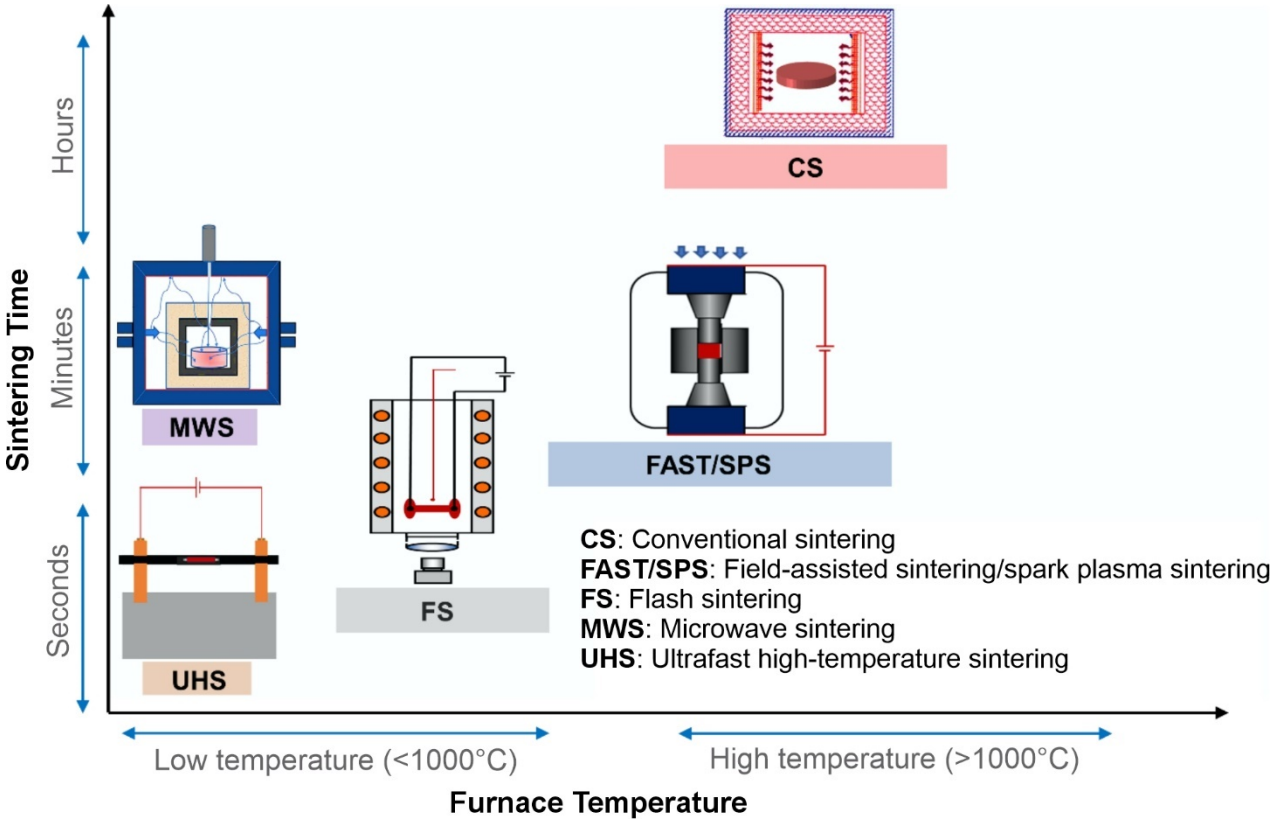

Figure 2.4: Schematic comparison of various sintering techniques in terms of sintering time and furnace temperature: The progression from conventional sintering (CS) to ultrafast high-temperature sintering (UHS) with a significant reduction in processing time (from hours to seconds) and furnace/mold temperature requirements (from ~2000°C to room temperature).

As a subclass of field-activated sintering techniques, electric current assisted sintering (ECAS) refers to a class of consolidation methods where the application of an electric field enables very high heating rates and significantly shorten sintering times [1,57,58]. Currently, main methods of conducting ECAS are direct heating of conductive ceramics via the Joule effect or indirect heating of nonconductive powders in a conductive tool. Among these techniques, FAST/SPS can densify both conductive and non-conductive powders with the help of a conductive tool and external pressure, whereas FS directly heats ceramic samples that exhibit high conductivity at elevated temperatures, which allows current to flow through the sample with generated Joule heating. On the other hand, UHS relies on indirect heating through thermal conduction and radiation, with Joule heating generated only in the carbon strips rather than the sample itself.

In the following sections, the proposed mechanisms for enhanced densification during ECAS are discussed. Following this, two specific cases, FS and UHS, are presented, each highlighting different heating methods. The chapter concludes with a discussion on numerical modeling efforts aimed at addressing the challenges in ECAS technologies.

2.2.2 Densification enhancement mechanisms during ECAS

ECAS enables full densification of ceramic materials within seconds. Extensive research has been dedicated to understanding the mechanisms behind this rapid and enhanced densification. Despite these efforts, the dominant mechanisms and the complex interplay of various factors leading to such remarkable effects are still not fully understood. However, it is generally agreed that the densification process in ECAS is primarily governed by three key factors: the electric field, heating rate, and external pressure. Understanding the role of each of these factors provides valuable insight into the overall densification mechanism.

Effect of the electric field

The electric field influences the densification process either through the flow of electric current or the field itself. The source of electric field in ECAS can be direct current (DC), pulsed DC, or alternating current (AC) [59]. When current flow is possible, as in FS and FAST/SPS with conductive samples, internally generated Joule heating can become significant (**Figure 2.5a**), causing a substantial temperature increase in the sample. For ceramics that exhibit a negative temperature coefficient (NTC) of resistance, the Joule heating-induced temperature rise reduces electrical resistivity and allows more current to flow, which in turn produces more Joule heating. This positive feedback loop leads to thermal runaway as observed in FS [60,61]. Some researchers [60] have attributed the rapid densification during ECAS to this uncontrolled avalanche effect, where the localized and rapid temperature rise may substantially exceed the conventional sintering temperature. However, the grain boundary overheating theory contradicts findings in FS of single crystals [62], suggesting that the event likely occurs within the crystal matrix.

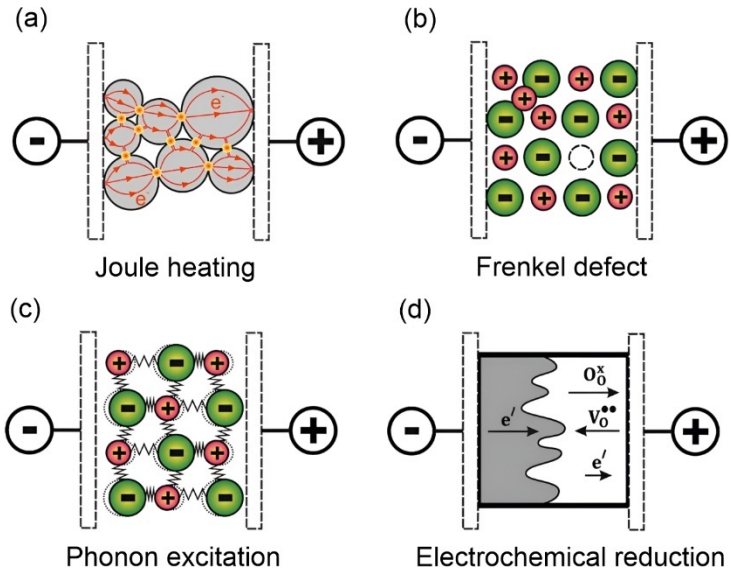

Figure 2.5: Schematic illustration of electric field-related mechanisms in ECAS: (a) Joule heating effect; (b) Frenkel defect generation; (c) phonon mode excitation; and (d) electrochemical reduction and blackening. Adapted from [59].

In addition to the flowing current, the electric field is believed to induce defect formation within the lattice, which could contribute to the enhanced densification. Raj et al. [63] proposed that a large number of Frenkel pairs (**Figure 2.5b**), far from equilibrium, can be generated by the electric field during FS. This process introduces numerous free electrons, holes, vacancies, and interstitial atoms. Under an applied electric field, vacancies are preferentially driven into the grain boundaries, while interstitials migrate into the pores, promoting densification. The electrons and holes migrate toward opposite electrodes, contributing to increased electrical conductivity. Furthermore, the recombination of some electron-hole pairs results in optical luminescence of a fixed wavelength. The hypothesis of electric field-induced Frenkel pairs offers a compelling explanation for all three key characteristics associated with FS: rapid densification, abrupt increase in conductivity, and electroluminescence. However, equilibrium thermodynamic calculations have shown that generating such defect pairs in the crystal lattice would require electric fields significantly higher than those used in sintering experiments [64], raising questions about the validity of this theory.

Nevertheless, the presence of Frenkel defects during FS has been confirmed through experimental measurements of lattice expansion and DFT calculations [65]. Phonon activation (**Figure 2.5c**) has been suggested as an alternative mechanism for the formation of Frenkel pairs [66]. Phonons, which are quantized vibrations of atoms in a crystal lattice, are fundamental to heat transfer and energy dissipation in solids. Jongmanns et al. [66] discovered that rapid heating and applied electric fields increase phonon activity, particularly short-wavelength vibrations near the Brillouin zone edge, which can induce the formation of Frenkel pairs. This has been demonstrated in molecular dynamics (MD) simulations [66,67], where the injection of high-frequency phonons leads to the displacement of atoms from their lattice positions, creating these defects. When the phonon energy exceeds a critical threshold, the lattice is driven into a far-from-equilibrium state, where defect generation occurs in bursts rather than continuously, leading to rapid densification. This mechanism aligns with observations that the onset of FS often occurs near or above the Debye temperature—the temperature at which lattice vibrations dominate and phonon activity becomes more pronounced [68].

The application of electric field can change the electrochemical properties of materials. Electrochemical blackening (**Figure 2.5d**) caused by partial electrochemical reduction has been well studied for ionic conductors like yttria-stabilized zirconia (YSZ) [69,70]. The observed chromatic alteration typically develops starting from the cathode, where electron injection from the metal electrode causes the electrochemical reduction, which also leads

to a reduction in the electrical resistivity of the sample. This phenomenon is due to the migration of the positively charged oxygen vacancies that accumulate at the cathode side, while oxygen ions move towards the anode side. As the sample turns completely blackened, it exhibits a sudden, non-linear surge in conductivity. During FS, electrochemical blackening participates as a co-triggering mechanism in the flash transition through the activation of n-type electronic conductivity [71].

Effect of heating rate

The heating rate impacts the sintering process by affecting grain coarsening and the operation of different mass transport mechanisms. High heating rate and short-time sintering is known to suppress grain growth by minimizing the time the sample spends at high temperatures [72]. This phenomenon is particularly beneficial for densification, as coarsening changes the local surface curvature and thus decreases the driving force for sintering. Finer grain sizes maintain a higher local surface curvature, thereby preserving the driving force for sintering.

Furthermore, the heating rate influences the interplay between surface diffusion and densification. As mentioned in section 2.1.2, surface diffusion requires the lowest activation energy among mass transport mechanisms and dominates at lower temperatures. In the case of low heating rates (**Figure 2.6a**), surface diffusion has sufficient time to redistribute mass along pore surfaces, leading to neck growth between particles at the early stages of sintering. While this process increases pore rounding and reduces surface energy, it also decreases the driving force for densification without contributing significantly to overall densification. Conversely, high heating rates (**Figure 2.6b**) promote rapid densification by activating grain boundary and volume diffusion mechanisms. These mechanisms, which have higher activation energies, become dominant at higher temperatures. By quickly transitioning through lower temperature ranges, high heating rates minimize the time spent in regimes where surface diffusion and neck growth dominate [72]. This delay in pore spheroidization preserves the point contact structure, effectively preserving the driving force for densification and leading to enhanced densification [73].

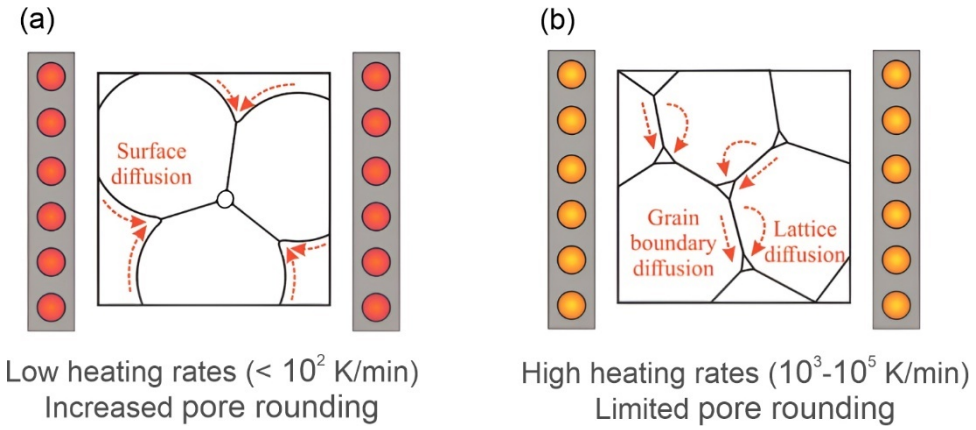

Figure 2.6: Schematic illustration of heating rate-related mechanisms in ECAS: (a) low heating rates: increased pore rounding due to neck formation and delayed densification caused by surface diffusion; and (b) high heating rates: limited pore rounding with rapid densification via immediately activated grain boundary and volume diffusion. Adapted from [59].

The significance of high heating rates in ECAS has been highlighted in several studies [74–76]. Ji et al. [74] compared different fast firing techniques with FS on 3 mol.% yttria-stabilized zirconia (3YSZ) and achieved similar densification by fast firing at a comparable heating rate to FS. They concluded that rapid heating (> 6000 K/min) without an electric field can accelerate the sintering process of 3YSZ by over two orders of magnitude compared with conventional heating (5 K/min) to the same temperature. Other studies on the heating rate effect in FAST/SPS [77] and UHS [76] also suggest that a high heating rate is a primary factor contributing to rapid densification.

Effect of external pressure

The application of external pressure during the sintering of ceramic materials allows for a reduction of the sintering temperature and the obtaining of fine-grained microstructures, as evidenced in FAST/SPS [78,79]. This effect is achieved through enhancing existing densification mechanisms while also inducing new ones under mechanical stress. As shown in **Figure 2.7a**, external pressure amplifies the effectiveness of grain boundary and volume diffusion, as well as viscous flow. This enhancement is particularly pronounced at higher temperatures, where the applied pressure can substantially accelerate mass transport along grain boundaries and through the lattice, while not affecting non-densifying mechanisms like surface diffusion or evaporation/condensation. Additionally, mechanical stress activates new densification mechanisms such as plastic deformation and grain boundary sliding (**Figure 2.7b**), further contributing to the densification process. The interplay between these enhanced and newly activated mechanisms can lead to more rapid densification at lower temperatures compared to CS.

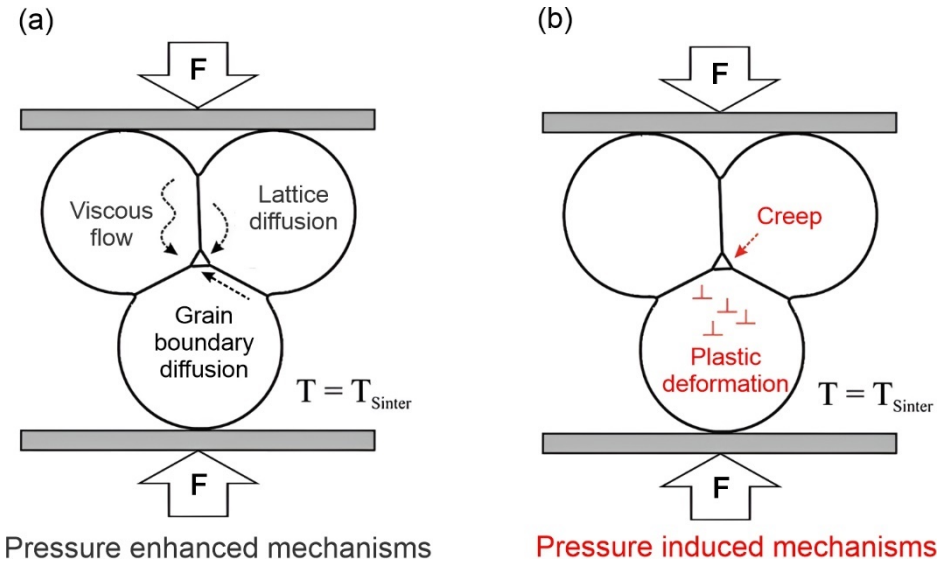

Figure 2.7: Schematic illustration of external pressure-related mechanisms in ECAS: (a) pressure enhanced mechanisms and (b) pressure induced mechanisms. Adapted from [59].

Apart from influencing densification mechanisms, the applied pressure also affects powder compaction at lower temperatures, which involves breaking down initial powder agglomerates and inducing particle rearrangement. This process enhances initial particle packing and reduces pore size, facilitating more homogeneous densification in subsequent sintering stages [50].

The densification mechanisms in ECAS involve the interplay of the electric field, heating rate, and external pressure. However, specific ECAS techniques may employ only one or two of these influencing factors. For instance, external pressure is absent for FS and UHS, while UHS does not directly apply an electric field to the sample. This difference presents a unique opportunity for systematic comparative analysis. Given the similar heating rates in FS and UHS, a direct comparison between these two methods enables a more focused investigation of individual influencing factors, reducing the complexity of their interplay. Since UHS primarily relies on thermal effect, while FS combines both thermal and non-thermal effects (electric field), comparative studies between these two techniques allow for a clearer delineation of the electric field's specific contribution to the sintering process. This approach provides valuable insights into the relative importance of thermal effect versus electric field effect in achieving rapid densification and helps unravel the fundamental mechanisms driving ECAS technologies.

2.2.3 Flash sintering (FS)

Flash sintering (FS) was first discovered in 2010 by the group of Prof. Raj [2]. This technique can densify ceramics at much lower furnace temperatures and in significantly

shorter times (usually < 10 s) compared to CS [46,80]. To initiate FS, a current is forced within a ceramic body by applying an electric field combined with external heating. When a specific onset temperature is exceeded, the sample becomes sufficiently conductive and a high electric current starts to pass through the sample. Heat is then generated through Joule heating in the sample, accompanied by luminescence and rapid densification in few seconds. Since the heating power is almost completely dissipated in the sample, FS is considered to be a highly energy efficient and economical process [81].

Stages of FS

FS typically undergoes three stages and is performed in a tubular vertical furnace, as illustrated in **Figure 2.8a**. In this setup, a dog-bone or bar-shaped sample is connected to a pair of metal wires (e.g., platinum) wrapped through the holes in the ears of the dog-bones or edge of the bars. The sample is suspended by these wires into the furnace [82]. The temperature of the sample is monitored by a thermocouple, while the shrinkage of the sample is recorded through a digital camera with optical filters positioned at the bottom of the furnace.

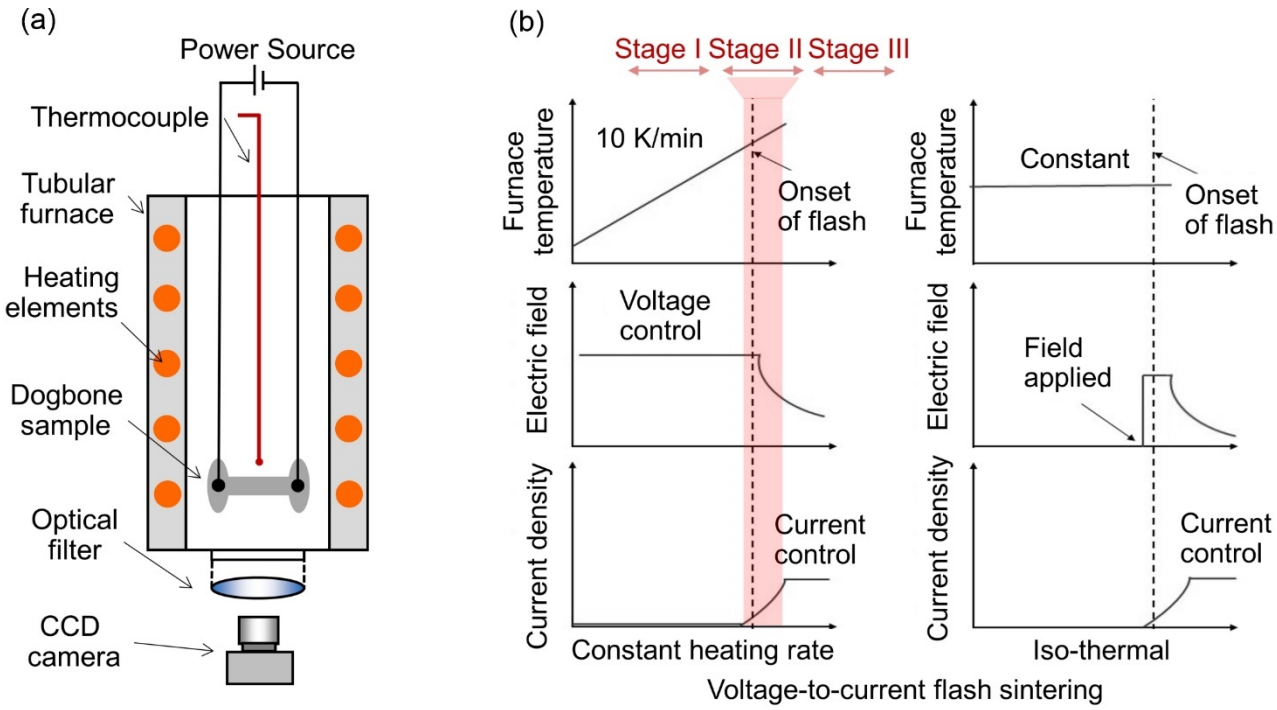

Figure 2.8: (a) Schematic setup of a typical FS and (b) three stages during voltage-to-current flash experiment.

Most FS experiments are carried out in the voltage-to-current mode. This mode can be performed either through “constant heating rate flash”, where the sample is heated at a steady rate while maintaining a constant electric field from the start, or through “iso-thermal flash”, where the furnace is held at a constant temperature and the electric field is applied

as a step voltage. The iso-thermal flash is applied when the onset temperature for the material and the applied electric field are known. In either case, a combination of furnace temperature and electric field triggers the onset of flash, while the magnitude of the current limit dictates the degree of densification [83].

The voltage-to-current controlled FS can be characterized by three distinct stages, as depicted in **Figure 2.8b**. For a constant heating rate flash experiment, each state is described as follows:

- Stage I: At room temperature, a constant voltage is applied to the sample, and the power source operates in voltage control mode. During this stage, the ceramic behaves as an insulator, with only negligible current flowing through the sample. The furnace temperature is then raised at a constant rate (typically 10 K/min). As the temperature approaches a critical point, the conductivity of the sample rises nonlinearly. This stage corresponds to the incubation period that varies from 1 second to several hours [84].
- Stage II: When a critical combination of the electrical field and furnace temperature is reached, the conductivity of the ceramic sample increases abruptly, allowing a high electric current to pass through the sample. This moment signals the onset of flash and triggers an avalanche-like effect, which leads to very fast densification in few seconds. During this stage, the power supply switches from voltage control to current control and maintains a predefined current density. The furnace temperature at the onset of flash is known as the onset temperature. The duration of this stage typically lasts between 1–5 seconds [84].
- Stage III: Once the prescribed current limit is reached, the power supply is fully under current control, and the voltage stabilizes in a quasi-steady state. The ceramic is sintered, grain growth may occur, and electro-luminescence is observed. At this stage, the furnace temperature is no longer necessary for maintaining the flash mode, and the sample can remain in this mode as long as the current is sustained [85].

In an iso-thermal flash experiment, the sample is placed in a furnace preheated to the required temperature. After a short stabilizing period (usually 10–15 minutes) to ensure a homogeneous temperature distribution, an electric field is applied. If the field is strong enough, the onset of flash can occur almost immediately, resulting in a very short incubation period (Stage I). The subsequent stages proceed similarly to those in the constant heating rate flash.

Electric field and onset temperature of FS

FS has been successfully applied to a variety of monolithic ceramics and composites, including insulators, electronic conductors, and semiconductors. A common characteristic among these materials used in FS is their NTC of electrical resistivity [46], meaning their electrical resistivity decreases as temperature increases. This distinct property allows for the thermal runaway phenomenon observed during FS, which only occurs at a specific combination of temperature and applied electric field.

The onset temperature of FS is defined as the furnace temperature at which the material's electrical conductivity begins to rise nonlinearly, and it is inversely influenced by the magnitude of the applied electric field. This abrupt nonlinear rise in conductivity takes place only when the applied electric field exceeds a material-specific critical value. For example, an electric field of at least 60 V/cm is required for 3YSZ to initiate the onset of flash. This relationship between the applied electric field and the onset temperature of FS is universal across all studied materials, as illustrated in **Figure 2.9** [86]. The onset temperatures for FS in these different ceramics vary from 300°C to 1300°C, with corresponding electric fields spanning from 10 V/cm to over 1000 V/cm. Despite the wide range of conditions, it is noteworthy that the onset of the nonlinearity always occurs within a narrow range of power density—approximately 10–60 mW/mm^3, as shown in the figure. This finding suggests the critical role of Joule heating in the FS process.

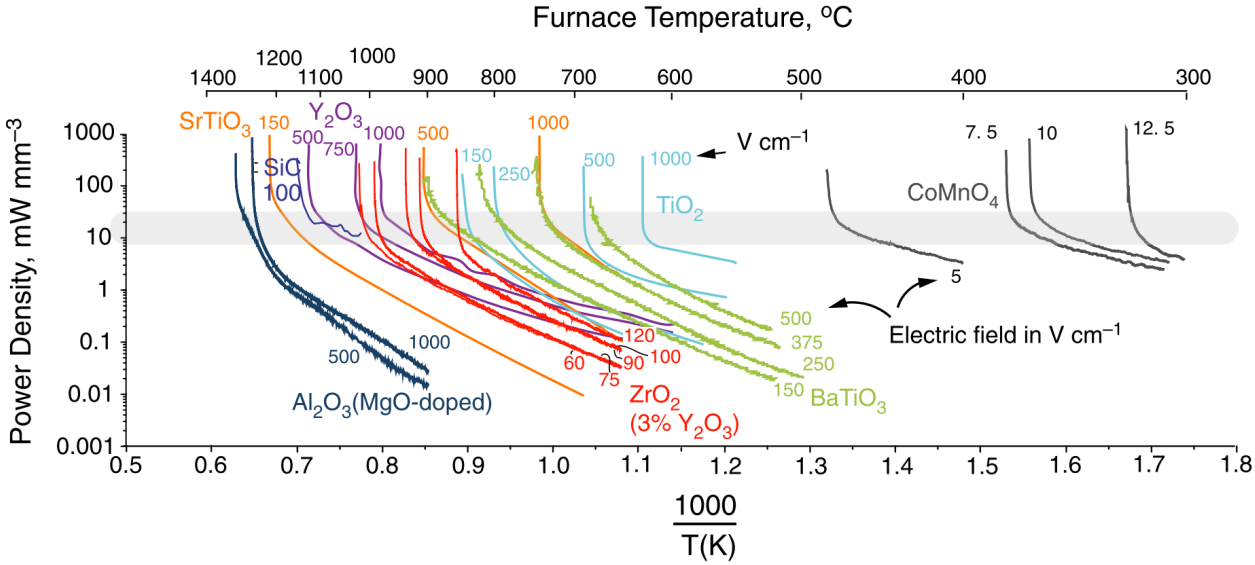

Figure 2.9: Onset of flash in different ceramics during constant heating rate experiments. The onset temperatures fall within a narrow power range, regardless of variations in the applied electric fields. The numbers above each curve denote the applied electric field in V/cm [86].

The inverse relationship between the electric field and onset temperature in FS is bounded by a lower limit related to the Debye temperature Θ_D. Yadav and Raj [68] investigated the onset temperature of YSZ and found that with increasing electric field, the onset temperatures of 3YSZ and 8YSZ stabilized at approximately 450 K. This value falls within the range of Debye limit (450–525 K), as shown in **Figure 2.10**. This lower bound of onset temperature has also been observed in other materials such as TiO_2 and 10 mol.% gadolinium-doped ceria (GDC10) [87].

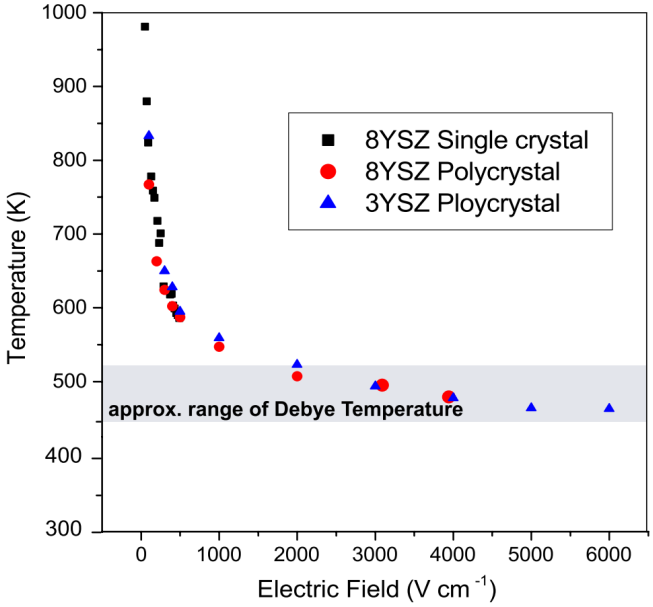

Figure 2.10: Relationship between onset temperature and applied electric field for various dense polycrystalline and single crystal specimens of 3YSZ and 8YSZ [68].

Since the Debye temperature represents the temperature at which the crystal's highest normal mode of vibration occurs [88], its role as the lower bound for flash onset temperature indicates that nonlinear lattice vibrations are essential for initiating the flash event. Below Θ_D, phonon wavelengths exhibit long-range character and are equal to or greater than the lattice parameter, which prevents the occurrence of nonlinear lattice vibrations necessary for FS. This correlation between Θ_D and the onset temperature supports the proposed mechanism of phonon activation during FS, where high-frequency phonons near the Brillouin zone edge can induce the formation of Frenkel pairs [66].

Novel approaches in FS

In addition to the voltage-to-current controlled FS, new flash technologies have been developed to improve the process and the product quality. One approach is to change the operating mode of the FS process. For example, flash experiments can be controlled from the very start by injecting current that increases at a constant rate, thereby avoiding the abrupt spike in power density seen in voltage-to-current flash. Consequently, the

densification occurs steadily with the increasing power density. This method is known as current-rate flash sintering (CRFS) or shrinkage-rate controlled flash (SCF) sintering [89,90]. Mishra et al. [47] employed this current-controlled mode and produced a uniform grain size across the entire gage length of the dog-bone sample made of GDC10, with nearly full densification.

Another way to improve FS is through apparatus modification. This method integrates the FS setup with additional equipment such as a custom-made dilatometer (DIL) [91], mechanical loading frame [92], or FAST/SPS equipment [93,94]. The combination of FS and FAST/SPS, known as flash spark plasma sintering (FSPS), has the advantage of scaling up the sample geometry and providing a more generalized compact form, rather than being restricted to dog-bone shapes, making it more suitable for practical applications.

2.2.4 Ultrafast high-temperature sintering (UHS)

In 2020, a novel sintering technology called ultrafast high-temperature sintering (UHS) was reported by Wang et al. [3]. The initial setup used two parallel carbon strips connected to electrodes to heat the powder compact placed between them. Joule heating in the carbon strips generated heat, which was transferred to the powder compact through radiation and conduction. It was found that the ceramic powder compacts were able to be consolidated by UHS in a few seconds [3,95,96].

A typical UHS setup is illustrated in **Figure 2.11**. The carbon strips are connected to electrodes and the pre-compacted sample is placed between two carbon strips. UHS requires relatively simple equipment, as no external furnace is needed. However, an inert atmosphere is necessary during UHS to prevent oxidation of carbon strips. In contrast to other ECAS techniques like FAST/SPS and FS, which rely on external pressure or conductivity of the sample, UHS consolidates samples solely through thermal radiation and conduction from the carbon strips, without the influence of pressure or electric field. The only influencing factor of UHS is its extremely high heating rate (10^3–10^4 K/min), which can significantly enhance densification while minimizing grain growth.

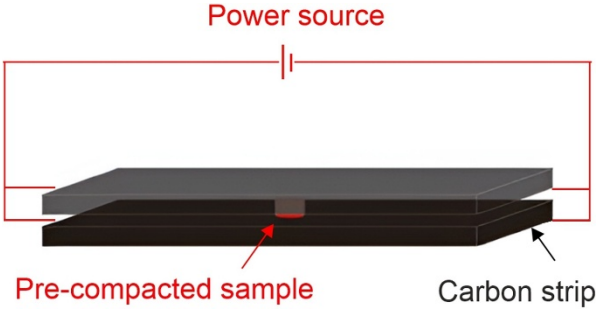

Figure 2.11: Schematic of a typical UHS setup with two carbon strips.

UHS is an all-materials inclusive technique, as it imposes no requirement on the electrical conductivity or geometric shape of the sample [97]. Despite its relatively recent development, UHS has been applied to a broad range of ceramic materials, including ultra-high-temperature ceramics (ZrB_2 [98], TiC [99]), electrolyte materials (GDC [100], YSZ [101], $Na_3Zr_2Si_2PO_{12}$ [102]), glass-ceramics [103], silica glass [104], high-entropy ceramics [105], Al_2O_3 [54], $SrTiO_3$ [76] and Si_3N_4 [106]. Additionally, the flexibility of the carbon felt heating element makes UHS highly adaptable, enabling the sintering of complex 3D printed bodies [3], multilayered ceramics [3], ceramic thin films [107] and ultrathin free-standing membranes [108]. The versatility of this technique broadens its potential applications and makes it one of the most promising ECAS methods for ongoing exploration.

Despite its simplicity and versatility, UHS faces challenges in achieving temperature homogeneity across the sample and scaling up for industrial use. Studies indicate significant temperature gradients during UHS, leading to partial melting and microstructural inhomogeneity even in small samples (8 mm diameter, 1 mm thickness) [76,109]. Current research addresses these challenges through improving thermal insulation methods and optimizing process parameters. For instance, Dong et al. [55] placed an alumina fiber board insulator around the carbon felt during UHS of 3YSZ and reduced the energy consumption by 40%. Wu et al. [110] implemented a pre-sintering step to decrease thermal gradients, resulting in crack free samples. Other strategies such as stepwise current increase [54] and prolonged thermal cycles [111] have further maximized densification while inhibiting grain growth during UHS.

Another issue with UHS lies in the use of carbon strips/felt as heating elements, which can lead to operational limitations and carbonation of sample surfaces. Efforts to address these challenges include exploring alternative heating materials and configurations. Liang et al. [112] developed a new configuration that combines a graphite paper heater and a pulsed DC power source, enabling ultrafast high-temperature heating in air. Other materials such as tungsten have been used as heating elements to suppress the undesired carbon contamination, as demonstrated in the study by Wu et al. [101]. In their work, a tungsten heater was placed in a hybrid UHS and FAST/SPS system (UH-SPS) and translucent YSZ ceramics were sintered within 80 s. Furthermore, a graphite powder-based UHS configuration (P-UHS) has been developed to obtain much larger and complex-shaped products. By embedding the sample in the graphite powder bed, bulk alumina ceramics with dimensions of 10 × 10 × 25 mm^3 were fully densified with homogeneous microstructure [113].

2.2.5 Simulation of ECAS

The complex physical nature of ECAS leads to numerous interdependent process variables and parameters, making comprehensive experimental characterization both expensive and time-consuming. Furthermore, the instantaneous and non-equilibrium characteristics of ECAS bring significant challenges for in-situ experimental measurements. Monitoring the evolution of temperature, current density, and microstructure in real-time remains particularly challenging. Understanding these factors is crucial for studying underlying mechanisms and improving temperature homogeneity for upscaling of the technologies.

Computational modeling has consequently emerged as an invaluable approach in ECAS research. It aims to simulate critical process characteristics including temperature distribution, defect dynamics, densification, and microstructural evolution. These models can be categorized into three primary scales: atomic, microscopic, and macroscopic, each addressing specific aspects of the sintering process.

Atomic-scale simulation

Atomic-scale simulation has been widely employed to study the formation and mobility of defects in materials under the influence of electric field. Frenkel defects, as previously discussed (section 2.2.2), are believed to play a pivotal role in enhancing densification during ECAS. Lebrun et al. [65] confirmed the presence of Frenkel defects during FS using DFT calculations, demonstrating their potential contribution to the process. However, the electric field required to directly generate Frenkel pairs is significantly higher than those typically used in FS. This discrepancy led to the development of the phonon activation mechanism as an alternative explanation.

Using Molecular Dynamics (MD) simulations, Jongmanns et al. [67] demonstrated that applied electric fields increase phonon activity, particularly short-wavelength vibrations near the Brillouin zone edge, which can induce the formation of Frenkel pairs. Xu et al. [114] further investigated the Frenkel pair formation during FS using MD simulations. They calculated the diffusion coefficients of Y, Zr, and O ions in 8YSZ under electric field. Their results showed that an intense electric field not only promotes the formation of cation Frenkel pair defects but also significantly enhances the diffusivities of both cations and anions within the 8YSZ system. These findings highlight the critical role of electric field in activating defect formation and driving ionic transport, offering valuable insights into the underlying mechanisms of ECAS processes.

Microscale simulation

Microscopic-scale simulation of ECAS bridges the atomic and macroscopic scales, it can reveal microstructural evolution of the material during the sintering process, which reflects macroscopic shrinkage and aids in predicting densification. For example, Sweidan et al. [115] used kinetic Potts Monte Carlo (kMC) simulations to analyze the microstructural changes in density-graded stainless steel 304 L during the FAST/SPS process. Their study evaluated key parameters such as sintering time, initial powder density, sintering temperature, and temperature gradient slopes. The results showed that the density profiles obtained from the kMC simulations match the values obtained from the experimental measurements.

Phase field methods have also been extensively applied to model the influence of electric fields on microstructure and charge transport. Vikrant et al. [116] studied the incubation kinetics of 3YSZ during FS, identifying three distinct regimes of microstructural evolution—radiation-dominated, transition, and percolative. The increase of oxygen vacancy concentration at particle contacts and surfaces during the percolative stage facilitates efficient charge flow and Joule heating, which ultimately accelerate densification. Similarly, Bejarano-Palma et al. [117,118] used phase field simulations to investigate anisotropic microstructures in last-stage ceramic sintering. The model effectively isolates effects of electric fields from thermal contributions. Their results indicate that while electric fields can induce microstructure anisotropy, their role in enhancing sintering kinetics is negligible without thermal energy.

In conclusion, microscale simulations provide profound insights into the interplay between electric fields, thermal energy, and microstructural evolution, thereby advancing our understanding of ECAS sintering mechanisms.

Macroscale simulation

Simulation of ECAS at the macroscopic scale often adopts analytical approaches or FEM to model the thermal and mechanical fields during sintering. Temperature prediction remains a primary research focus, as achieving uniform temperature distribution is critical for controlling gradients, ensuring densification, and producing homogeneous microstructures. However, modeling temperature fields is inherently complex due to two major factors: the first is heat generation via the Joule effect under high-intensity electric current. Given the non-uniform current distribution, the heat production also varies significantly across the sample-setup assembly. The second factor involves heat dissipation (cooling mechanisms), including heat radiation from external surfaces and heat

transfer to electrodes. Accurately anticipating the combined influence of these factors on the resulting temperature fields is challenging. Specialized tools like Engemini have been developed for FAST/SPS by Norimat in France [119], offering tailored capabilities for such complex simulations. This software enables seamless geometry import, precise definition of boundary conditions and material properties, and effective visualization of simulation results. Other ECAS techniques, including FS and UHS, rely on mathematical modeling [60,89,120] and multiphysics software packages [121–124], such as ANSYS, ABAQUS, and COMSOL, to solve coupled thermo-electric-mechanical problems.

For densification, various constitutive models have been proposed to account for the influence of pressure [125–128], electric current [129,130] and high heating rate [73,77] in FAST/SPS. Two common constitutive laws are used for FAST/SPS: one is the model proposed by Bernard-Granger [125,126], which is an analytical approach based on the steady-state creep model to describe the creep behavior of dense materials. This model assumes that macroscopic applied pressure is the primary driving force for pressure-assisted sintering, neglecting contributions from pressure-less sintering. An alternative approach is the Skorohod-Olevsky model [31,32], which is grounded in continuum mechanics and describes consolidating powders as a viscous material. The continuum mechanics models of sintering involve a set of constitutive equations that link the shrinkage of a porous body with viscous parameters and the generalized state of stress. These models, capable of predicting the evolution of component shape under the influence of macroscopic parameters during sintering, are particularly valuable for analyzing the sintering of complex systems like FAST/SPS.

Research on FS and UHS densification modeling is still relatively scarce. Most models developed so far for predicting densification are based on kinetic approaches such as master sintering curve (MSC). One of the earliest attempts to model densification during FS utilized a heat equation coupled with an apparent activation energy kinetic equation for densification [131]. More recent studies have combined FEM with kinetic models to improve predictions. For instance, Arya et al. [132] employed the MSC approach integrated with FEM to predict the densification behavior of 3YSZ, 8YSZ, and TiO_2 during FS. Their model demonstrated strong agreement with experimental observations at higher current densities (100–150 mA/mm²) but failed at lower current densities (< 100 mA/mm²). This discrepancy was attributed to the omission of non-thermal effects in the model. However, their model assumed that densification mechanisms remain unaffected by high heating rates and simply extrapolated experimental data from conventional heating rates (5–20 K/min) to ultra-high heating rates (~ 2000 K/min). This method presents significant limitations,

considering that high heating rates likely introduce distinct sintering mechanisms. Additionally, a phenomenological model has been developed and coupled with FEM to investigate the impact of sample geometry and electrode configurations on temperature and density uniformity during the FS of 3YSZ [133]. This constitutive model employs a simplified representation of densification, relying on semi-empirical mathematical relationships for properties such as electrical and thermal conductivity. It is noteworthy that none of the constitutive models developed so far have incorporated the grain growth factor in their densification modeling. Given that the effect of grain size on densification and the ability of ultra-high heating rate to tailor the microstructure are non-negligible, a sophisticated constitutive model coupled with a grain growth law is urged.

For UHS, densification modeling has so far relied solely on the analytical MSC approach. Dong et al. [55] applied MSC to predict the densification of 3YSZ under thermally-insulated UHS conditions. While the MSC approach provides a practical empirical framework for describing sintering processes, it has significant limitations when attempting to draw comprehensive physical mechanism conclusions across diverse thermal conditions. A critical constraint is that the microstructure must be a unique function of density, which is difficult to achieve consistently. Given the strong dependence of microstructure on thermal history in many ceramic systems like YSZ [134,135], more sophisticated models that couple grain growth predictions with densification are essential for accurately describing sintering under ECAS. Additionally, these modified models should account for possible additional sintering mechanisms introduced by the specific conditions of ECAS.

2.3 Summary of fundamentals and state of the art

This chapter provides a comprehensive overview of the fundamental principles and contemporary advancements in the field of sintering. The discussion focuses on the underlying mechanisms of densification during sintering. It begins with the basic and fundamental mass transport mechanisms, which are categorized into two groups: surface transport mechanisms (e.g., surface diffusion) and bulk transport mechanisms (e.g., grain boundary diffusion). Then the ECAS technologies have been introduced. The significant reduction in sintering time during ECAS leads to investigations into the competing mechanisms responsible for enhanced densification. The effects of three critical factors—electric field, heating rate, and external pressure—have been examined. The electric field is found to induce far-from-equilibrium defects that may contribute to enhanced densification. The heating rate and external pressure accelerate densification by impacting the interplay of different mass transport mechanisms. However, the literature on the role of thermal and non-thermal effects during ECAS remains inconsistent. The dominant influencing factor is still not well understood, and a universal explanation for the rapid densification has yet to be established. In reality, multiple mechanisms likely operate simultaneously, and their relative contributions may vary across different ECAS techniques and materials.

Two specific ECAS technologies, FS and UHS, have been introduced in detail. The primary distinction between these methods lies in their heating sources. FS heats samples through Joule heating by conducting current through the material, whereas UHS heats samples indirectly through the thermal radiation and conduction from the carbon felt. Therefore, the electric field directly contributes to the sintering process in FS, but this influence is absent in UHS. This contrast provides a valuable opportunity to study the role of the thermal and non-thermal effect during ECAS separately.

To further enhance the understanding of sintering mechanisms and optimization of sintering, numerical simulation has been presented across three different scales: atomic, microscale, and macroscale. Phenomena such as defect dynamics, microstructural evolution, temperature distribution and densification have been investigated by numerical methods. Despite the extensive literature on ECAS consolidation techniques (nearly nine thousand studies), less than two hundred papers focus on mathematical modeling, and only few tens of papers address the simulation of densification phenomena [136]. Even fewer studies are dedicated to FS and UHS. A sophisticated constitutive model integrated with FEM, capable of accounting for the densification enhancement effect, is still lacking for ECAS such as FS and UHS. Developing a thermal-electrical-structural model that

comprehensively explains densification and grain growth during ECAS is essential for advancing the understanding of the underlying mechanisms.

3 Motivation and objectives

3.1 Motivation and research questions

ECAS drastically shortens sintering times, reducing processes that typically take hours in conventional methods to mere seconds. The underlying mechanisms driving this remarkable densification rate pose significant research challenges. The complexity arises from the interaction of multiple physical fields—electric, thermal, and mechanical. Each field uniquely influences mass transport and microstructural evolution, leading to the concurrent activation of various sintering mechanisms. Despite extensive research, the dominant densification enhancing mechanisms remain a subject of ongoing debate. Moreover, the instantaneous nature of ECAS processes further complicates experimental investigations, making real-time monitoring of the critical parameters, such as temperature, current density, and microstructure, highly challenging.

Consequently, this dissertation seeks to address the following research question:

“What are the dominant factors enhancing densification in ECAS processes, particularly in FS and UHS? How can these effects be incorporated into a constitutive model to predict this enhanced densification?”

Based on the state of the art in ECAS technologies, the key influencing factors that contribute to the enhanced densification during FS and UHS can be summarized as follows:

1. Extra-high sample temperature (up to 3000°C):
   The rapid Joule heating during ECAS can result in uncontrolled temperature increases, reaching up to 3000°C, far exceeding conventional sintering temperatures.
2. Ultra-high heating rate (10^3–10^4 K/min):
   Both FS and UHS are ultra-fast firing techniques with heating rates in the range of 10^3–10^4 K/min. These ultra-high heating rates can alter mass transport mechanisms and influence microstructural evolution, thereby affecting the densification rate during sintering.
3. Direct influence of electric field:
   Apart from generating heat through current conduction, the presence of an electric field directly impacts the sintering process through defect mechanisms and electrochemical reactions. These non-thermal effects could play a critical role in enhancing densification during ECAS.

The corresponding research hypothesis for this thesis is then proposed as:

“With the help of FEM, the temperature distribution and heating rate of the sample during ECAS can be predicted. By comparing FS and UHS under similar heating rates and sintering temperatures, the contribution of thermal and non-thermal effects can be analyzed. The dominant effects can then be incorporated into a constitutive model to verify the validity of the proposed theory.”

3.2 Objectives

This research focuses on the experimental and numerical investigation of two ECAS technologies: FS and UHS. Two different oxide ceramics are selected for the sintering experiments: 8YSZ and $SrTiO_3$. The primary scientific objective of this dissertation is:

“Understanding the dominant sintering mechanisms of ECAS in 8YSZ and $SrTiO_3$ with the help of numerical simulation”

To achieve this aim, the following sub-objectives have been defined:

1. Understanding the FS and UHS process for producing fully dense ceramic samples:
   To produce fully dense samples, a systematic investigation of densification behavior needs to be conducted under various process parameters, such as furnace temperature, current density, and dwell time. A process window that allows the production of samples in good condition with optimal efficiency should be proposed.
2. Prediction of temperature distribution in FS and UHS:
   To understand the temperature evolution and distribution within the sample, a thermal-electrical FEM model needs to be developed. This objective requires material-specific adaptations for 8YSZ and $SrTiO_3$. Accurate temperature predictions are essential for conducting a comparative study of the two sintering methods.
3. Characterization of sintering and microstructure to analyze densification and grain growth kinetics:
   The densities and grain sizes of the sintered samples should be quantitatively characterized to analyze the densification and grain growth kinetics. The obtained kinetic parameters (e.g., activation energy for densification and grain growth) can also be used for the subsequent modeling works.
4. Development of constitutive models for densification and grain growth:
   Formulating a phenomenological constitutive model combined with a grain growth law is the first step to predict densification and grain growth. By employing process-specific apparent activation energies derived from the sintering kinetic analysis, densification and grain growth can be predicted for different sintering methods.

5. Incorporation of the densification-enhancing factors in the constitutive model:
   Once the dominant densification-enhancing factors are identified, their effects must be incorporated into the constitutive model to simulate the densification. The model's validity should be examined. Successful validation of the model can also confirm the reliability of the proposed theory for densification mechanisms.

4 Materials

In the present study, two kinds of oxide ceramics, 8 mol.% yttria-stabilized zirconia (8YSZ) and strontium titanate ($SrTiO_3$), were investigated. The particle size distribution and Scanning Electron Microscopy (SEM) image of both powders are presented.

4.1 8 mol.% yttria-stabilized zirconia (8YSZ)

The starting material of 8YSZ is a commercially available granulated powder with a theoretical density of 5.88 g/cm^3 (Tosoh Corporation, Japan). The powder characterization of 8YSZ was conducted in the work of Mishra et al. [137]. The morphology of the powder was observed by a scanning electron microscope (SEM, Zeiss Ultra 55 FEG-SEM, Carl Zeiss Microscopy GmbH, Oberkochen, Germany). **Figure 4.1** shows the SEM micrographs of the 8YSZ powder at two different magnifications revealing the as-received agglomerated state (**Figure 4.1a**) and the primary particles (**Figure 4.1b**). The as-received powder appears to be in a spray-dried, agglomerated state; however, when the starting powder was mixed with ethanol and dispersed by ultrasonic treatment for 3 min, the primary particles can be observed, which are of sub-micron size.

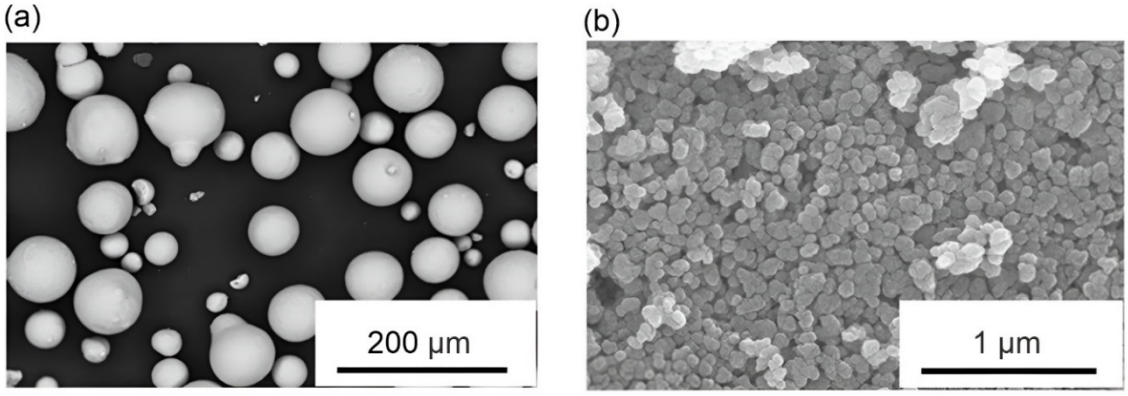

Figure 4.1: Scanning electron micrographs of the 8YSZ powders: (a) as-received condition and (b) after dispersing by ultrasonification for 3 min [137].

The particle size distribution of 8YSZ was measured with a laser diffraction particle size analyzer (LA-950-V2, Horiba Ltd., Tokyo, Japan). The resulting particle size distribution after 3 minutes of ultrasonic treatment is characterized by d_{10}=0.08 µm, d_{50}=0.18 µm, and d_{90}=37.26 µm, as shown in **Figure 4.2**. The distribution spans a wide range from nanometers to approximately 100 micrometers. However, SEM micrographs and specific surface area measurements indicate that the primary particle size lies predominantly in the nanometer range (approximately 0.1–0.2 µm), which aligns with the d_{10} and d_{50} values. The substantially larger d_{90} value (37.26 µm), on the other hand, reflects the volumetric influence of persistent larger agglomerates, as evidenced by the tri-modal distribution observed in **Figure 4.2**.

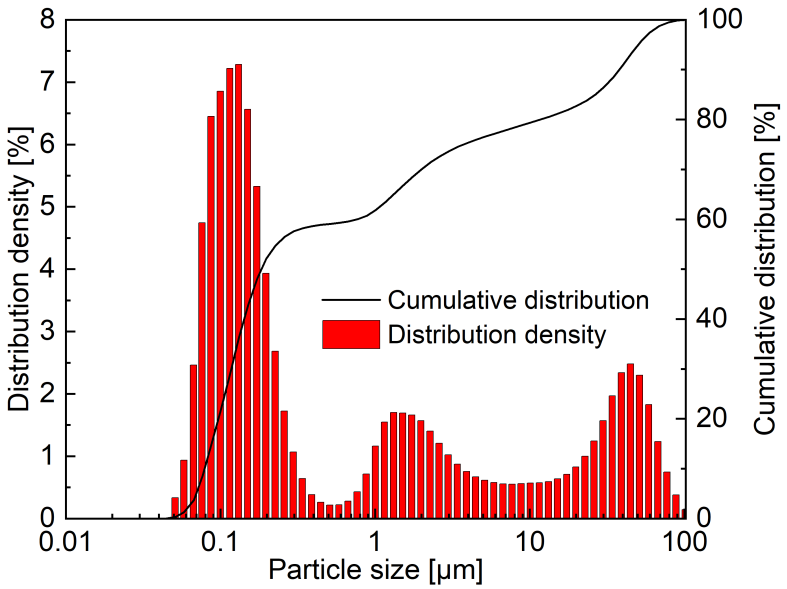

Figure 4.2: Particle size distribution of the 8YSZ powder after ultrasonic treatment.

Yttria-stabilized zirconia (YSZ) is a ceramic material where zirconia (ZrO_2) is doped with yttrium oxide (Y_2O_3) to stabilize its high-temperature phase at room temperature. Among the various YSZ compositions, 8YSZ is widely utilized due to its ability to fully stabilize the cubic phase. As illustrated in **Figure 4.3** [138], 8YSZ exhibits a fluorite-type cubic structure, where Y^{3+} ions substitute for Zr^{4+} ions in the lattice, creating oxygen vacancies to maintain overall charge neutrality. These oxygen vacancies act as conduction pathways for oxide ions (O^{2-}), making 8YSZ a material with high oxygen-ion conductivity. Consequently, it is commonly used as a solid electrolyte in solid oxide fuel cells (SOFCs) and oxygen sensors. However, 8YSZ is considered an isolator at room temperature due to its extremely low conductivity. As temperature increases, it shows a negative temperature coefficient (NTC) of electrical resistance, which means its conductivity increases with temperature. This character makes 8YSZ suitable for FS studies, where an onset temperature is necessary to ensure adequate conductivity for current to flow through the material.

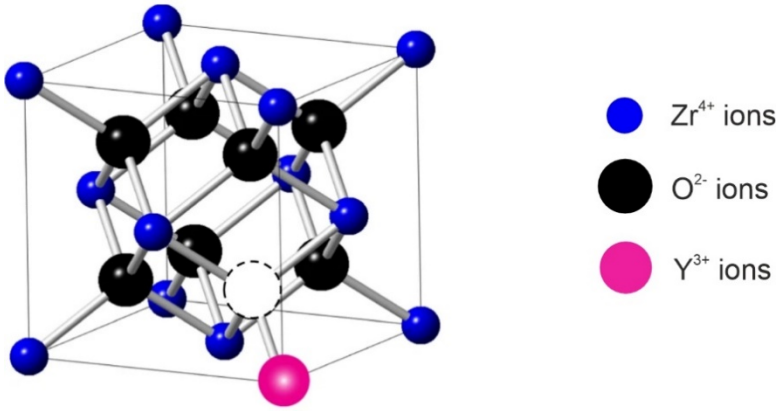

Figure 4.3: The fluorite crystal structure of 8YSZ [138].

4.2 Strontium titanate ($SrTiO_3$)

The starting material of $SrTiO_3$ used in this study is a synthetic powder. The synthesis process of the starting powders has been reported elsewhere [139,140]. The powder morphology was observed by SEM, and the micrograph of $SrTiO_3$ powder is presented in **Figure 4.4a** [141]. The particle size distribution was measured with the laser diffraction method in the work of Mishra et al. [76]. The results are given in **Figure 4.4b**. It can be seen that the $SrTiO_3$ starting powder had a unimodal distribution, with measured particle sizes of d_{10}=0.69 µm, d_{50}=1.65 µm, and d_{90}=3.93 µm.

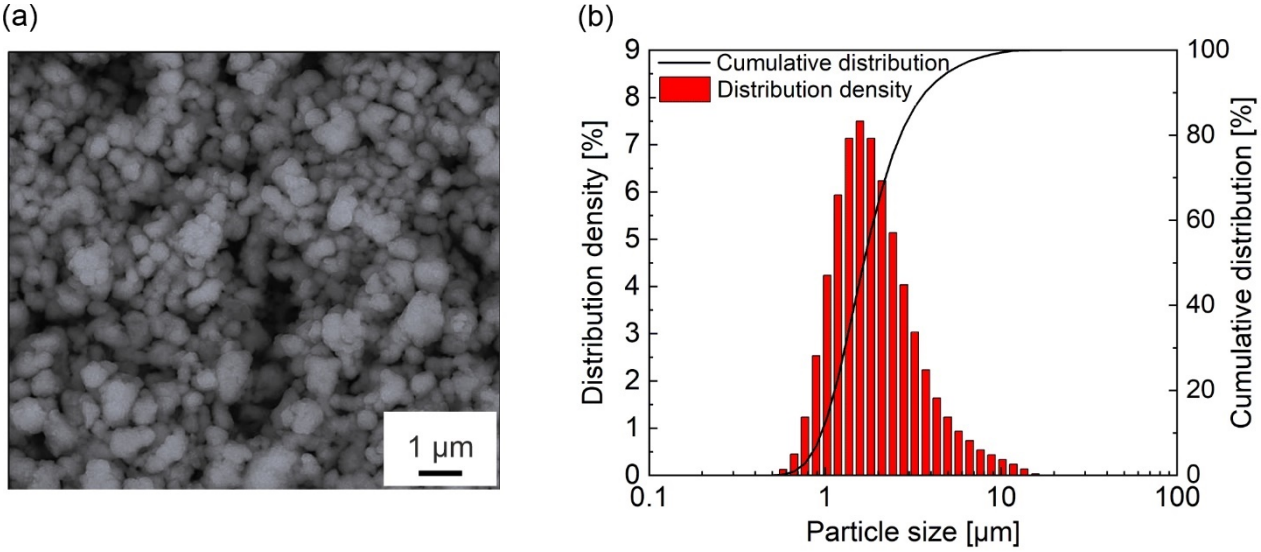

Figure 4.4: Powder characterization of $SrTiO_3$: (a) the scanning electron micrograph and (b) the size distribution.

$SrTiO_3$ is a member of the perovskite family, characterized by the general formula ABO_3. In $SrTiO_3$, Sr occupies the A site and Ti occupies the B site. Its structure is shown in **Figure 4.5** [142]. At room temperature, it crystallizes in a cubic perovskite structure with a lattice parameter of ~3.905 Å. The structure can undergo phase transitions under certain doping conditions or external stress, but the simple cubic structure is the most common form.

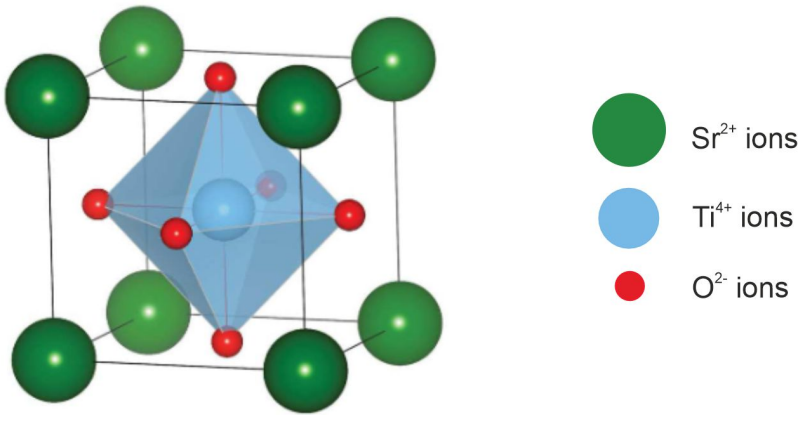

Figure 4.5: The crystal structure of $SrTiO_3$ perovskite compound [142].

$SrTiO_3$ exhibits diverse electrical behaviors, ranging from insulating to semiconducting or even metallic, depending on doping and defect concentrations. While intrinsic $SrTiO_3$ is generally considered a band-insulator, doping with acceptor (e.g., Mg, Fe) or donor (e.g., Nb, La) impurities can significantly alter its electrical properties. With its superior chemical and thermal stability, low toxicity, high dielectric constant, and low dielectric loss [143], $SrTiO_3$ finds widespread applications in electronics, photocatalysis, quantum dot–sensitized solar cells, and electroceramics.

5 Experimental and numerical methods

This chapter describes the investigation methods applied to 8YSZ and $SrTiO_3$. The first section introduces various sintering methods and the experimental procedures. It is worth noting that both FS and UHS were conducted on 8YSZ, which enables a comparative analysis to evaluate the contributions of thermal and non-thermal effect. The subsequent study on $SrTiO_3$, on the other hand, concentrated exclusively on UHS for a more dedicated investigation on the influence of high heating rate. For each ECAS technique, parallel CS experiments were carried out for comparison. The second section presents the material characterization methods, and the chapter concludes with an introduction to the numerical modeling work.

5.1 Sintering experiments

5.1.1 Flash sintering (FS)

The dog-bone shaped samples were used to conduct the FS experiments. To prepare the samples, 8YSZ powder was uniaxially pressed within a dog-bone shaped die at 100 MPa. These dog-bone shaped samples had a gauge length of 15 mm, a width of 3.3 mm and a thickness of ~2 mm. Since the pressed green bodies were too fragile to be connected to the electrodes, they were pre-sintered at 900°C for 60 minutes. The pre-sintered samples had an initial green density of approximately 42–45% measured by the Archimedes method. The scheme of the experimental setup for FS is shown in **Figure 5.1**.

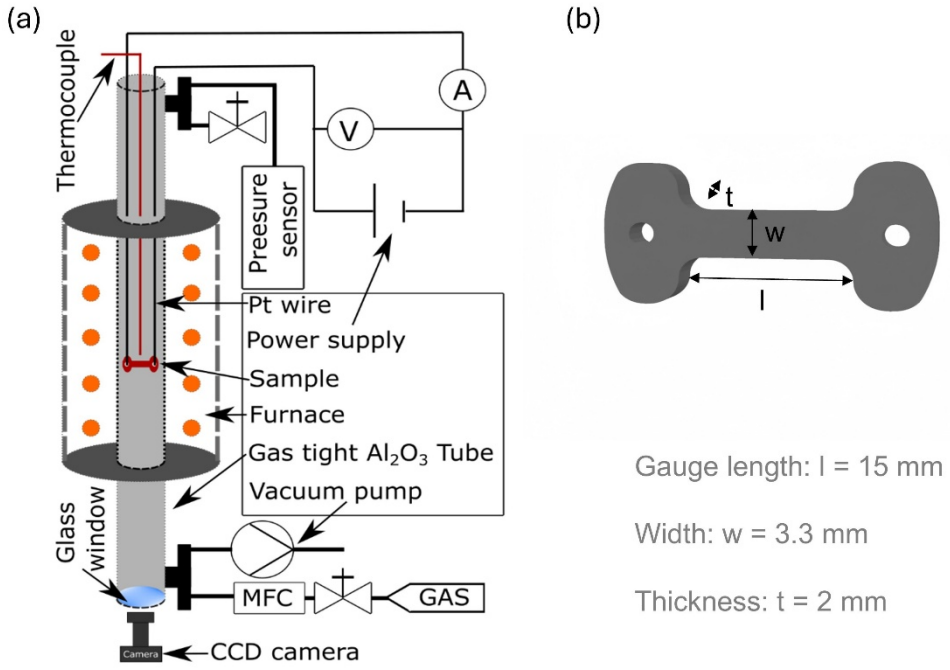

Figure 5.1: (a) Schematic diagram of the experimental setup of FS (Source: Tarini Prasad Mishra, Forschungszentrum Jülich, 2020, personal communication) and (b) specimen geometry of dog-bone shaped sample.

Isothermal FS experiments were carried out at a constant furnace temperature of 850°C in air. Each sample was placed in the furnace for 15 min before a constant electric field of 100 V/cm was applied. After the flash event, the device was switched from voltage control to current control, with the current densities ranging from 25 mA/mm² to 125 mA/mm² (in steps of 25 mA/mm²). After holding the sample at each current density for four different dwell times (15 s, 30 s, 60 s and 120 s), the power supply was turned off. After the process, the ear sections of the dog-bone shaped samples were removed, and the gauge sections were then characterized regarding the density and the microstructure.

For comparison, CS experiments were carried out in a push rod dilatometer (DIL 402C, NETZSCH, Germany) in air. The green samples were prepared by uniaxially pressing 8YSZ powder in a cylindrical die at 100 MPa. The pressed samples had a diameter of 8 mm and a height of ~ 4.5 mm. The pellet samples have a similar green density as the samples prepared for FS. To conduct the CS experiments, the samples were heated to three sintering temperatures (1200°C, 1250°C, and 1300°C) at a heating rate of 5 K/min. The dwell time was 2 h for all the experiments. The extracted temperature-shrinkage curves from DIL were converted to densification curves using the method described in the work of Maca et al. [144].

To study the microstructural evolution during CS, a series of isothermal interrupted sintering experiments were designed. The sintering cycles included a heating rate of 5 K/min, sintering temperatures ranging from 1300°C to 1450°C in 50°C intervals, and dwell times of 0, 12, 30, and 60 minutes at each sintering temperature. After the sintering experiments, the densities of the sintered samples were measured using the Archimedes method. The samples were thereafter metallographically prepared for the grain size analysis. **Table 5.1** summarizes the experimental design for both CS and FS experiments.

Table 5.1: Summary of experimental design for flash sintering (FS) and conventional sintering (CS) experiments of 8YSZ

Experiment	Sintering condition	Dwell time
Isothermal interrupted FS	25 mA/mm²	15, 30, 60, 120 s
	50 mA/mm²	15, 30, 60, 120 s
	75 mA/mm²	15, 30, 60, 120 s
	100 mA/mm²	15, 30, 60, 120 s
	125 mA/mm²	15, 30, 60, 120 s
Dilatometer CS (to obtain densification curve)	1200°C	120 min
	1250°C	120 min
	1300°C	120 min
Isothermal interrupted CS (to characterize grain size)	1300°C	0, 12, 30, 60 min
	1350°C	0, 12, 30, 60 min
	1400°C	0, 12, 30, 60 min
	1450°C	0, 12, 30, 60 min

5.1.2 Ultrafast high-temperature sintering (UHS)

UHS experiments were performed on both 8YSZ and $SrTiO_3$. For 8YSZ, the starting powder was uniaxially pressed into pellet-shaped powder compacts with a pressure of 100 MPa. The samples had a diameter of 8 mm and a thickness of 1–1.2 mm. Afterwards, the powder compacts were pre-sintered in a furnace at the temperature of 1000°C for 60 min to avoid the formation of entrapped gases during UHS. A starting relative density of 45% ± 2% was determined on the pre-sintered powder compacts.

The UHS setup was custom made and consists of two copper electrodes and a carbon felt (40 mm × 9.5 mm × 4 mm). A 9 mm length slit was cut in the middle of the carbon felt, and the pellet-shaped powder compact was put in the center of the felt. A good contact between the electrode and the felt was ensured by tightening the screws on the electrodes to allow the current to flow through the carbon felt. The UHS setup and the schematic illustration is shown in **Figure 5.2**.

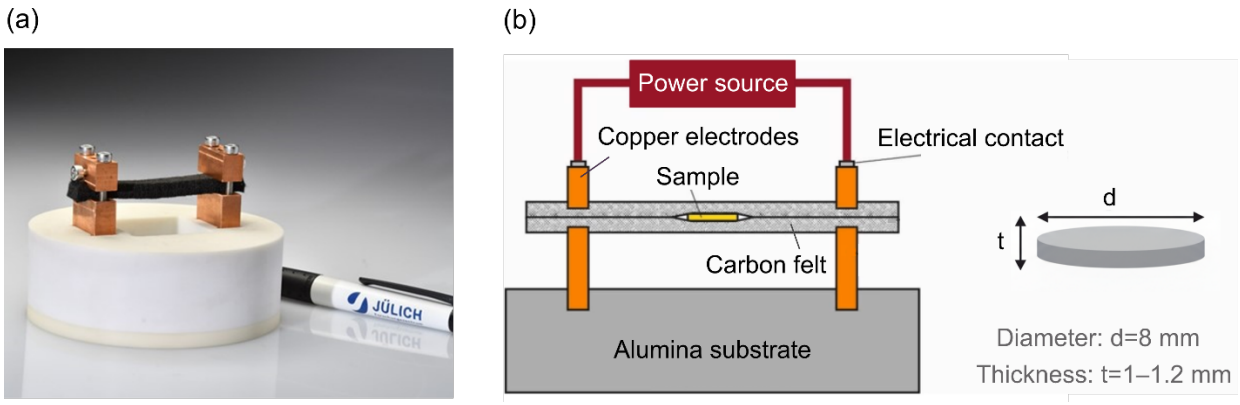

Figure 5.2: (a) The custom made UHS apparatus used in this study; (b) schematic diagram of the UHS experimental setup and specimen geometry [76].

The setup was operated in an argon-filled chamber to prevent oxidation of the carbon felt. The electric current was supplied by an AC/DC power source (TruPlasma Bipolar Series 4000, Trumpf Hüttinger). After the chamber was evacuated (< 0.2 mbar), it was filled with argon at a constant gas flow of 10 l/min. Subsequently, a DC electric current of 10–13 A with an interval of 1 A was applied to the carbon felt through metallic copper electrodes. The joule heating produced fast heating of the carbon felt, and the sample was heated by thermal conduction and radiation from the felt. Upon reaching the desired current levels, the current was held for four different dwell times: 30, 60, 90, and 120 s. These 16 interrupted isothermal experiments were used for parameter identification for the sintering model of 8YSZ. Additionally, a separate experiment was performed with a current of 15 A and a dwell time of 30 s to investigate sintering behavior at higher current levels. After the experiments, the power source was switched off, and the chamber was evacuated again to remove argon. Once the system had cooled, the sintered samples were taken out of the carbon felt, and their densities were measured using the Archimedes method.

During the experiments, the sample temperature could not be measured adequately due to the ultra-high heating rates. However, a pyrometer was used to measure the highest temperatures reached on the top surface of the carbon felt. Additionally, a thermal couple, nickel-chromium wires, and platinum wires were used to determine the highest temperatures at the inner surface of the carbon felt under different current levels. These measurements help us to verify the simulation results of the temperature distribution within the carbon felt, thus allowing us to estimate the sample temperatures. The detailed methodology for temperature verification is presented in a later section (7.2.1).

For comparison, CS experiments were also carried out in a push rod dilatometer TMA 402 F1 (Netzsch, Germany). The cylinder-shaped samples with a diameter of 8 mm and similar starting densities as the UHS samples were sintered in argon atmosphere to keep the consistency. For all dilatometer experiments, a heating rate of 5 K/min was applied. Different sintering cycles were used for the conventional experiments. The processing parameters of dilatometer sintering as well as the UHS are summarized in **Table 5.2**. For UHS, the average temperatures of the sample are estimated to be 1100–1500°C for the given currents (10–15 A) and dwell times according to the simulation.

Table 5.2: Summary of experimental design for ultrafast high-temperature sintering (UHS) and conventional sintering (CS) of 8YSZ

Experiment	Sintering condition	Dwell time
Isothermal interrupted UHS	10 A	30, 60, 90, 120 s
	11 A	30, 60, 90, 120 s
	12 A	30, 60, 90, 120 s
	13 A	30, 60, 90, 120 s
	15 A	30 s
Dilatometer CS	1450°C	0 min
	1250°C	120 min

The study of $SrTiO_3$ followed a procedure similar to that of 8YSZ, but with slight adjustments. The starting powder for UHS was initially uniaxially pressed at 120 MPa and subsequently compacted using a cold isostatic press at 300 MPa. The resulting green pellets had a shape comparable to the 8YSZ samples, with a relative density of approximately 58% ± 2% as measured geometrically. The UHS experiments of $SrTiO_3$ were performed under vacuum conditions (< 0.2 mbar). A DC electric current with maximum values ranging from 5 to 25 A was applied and held for 10 s in each experiment once the target maximum current was reached.

For CS of $SrTiO_3$, the same procedure as UHS was applied for sample preparation. The cylindrical samples had a diameter of 8 mm and a height ranging from 4 to 5 mm. These samples were sintered in a push rod dilatometer TMA 402 F1 (Netzsch, Germany) under an argon atmosphere with a constant gas flow of 50 ml/min. The sintering was carried out at 1500°C for 1 min with a heating rate of 25 K/min. **Table 5.3** summarizes the experimental design for both UHS and CS of $SrTiO_3$.

Table 5.3: Summary of experimental design for ultrafast high-temperature sintering (UHS) and conventional sintering (CS) of $SrTiO_3$

Experiment	Sintering condition	Dwell time
UHS	5–25 A	10 s
Dilatometer CS	1500°C	1 min

5.2 Characterization methods

5.2.1 Microstructural characterization

After the sintering experiments, the microstructure of the sintered 8YSZ samples was characterized. The characterization procedure followed a standard routine: first, the cross-sections of the samples were polished and thermally etched at a moderate temperature for 20–30 min in a conventional furnace to delineate the grain boundaries. For DIL-sintered samples, etching was performed at temperatures 150°C lower than their corresponding sintering temperatures. In the case of FS and UHS, where temperatures were not directly measured, the etching temperatures were set at least 150°C lower than the corresponding simulated average temperatures across the samples. The simulation procedure will be described in section 5.3.

Subsequently, the polished surfaces were sputter coated with gold to ensure sufficient conductivity for the scanning electron microscopy (SEM) analysis. Microstructures at various locations on the cross-section were then observed using a Helios Nanolab G3 CX Dual Beam Focused Ion Beam (FIB)-SEM (Thermo Fisher Scientific, USA). For DIL-sintered and UHS-sintered samples, two locations near the center of the cross-section were selected for analysis. The selection of observation locations for flash-sintered dog-bone-shaped samples required additional attention. To study the electrical polarity effect during FS, the gauge sections were first ground to the half of their thickness before polishing, and SEM images were taken at three different positions along the gauge section, spanning from the anode side to the cathode side (detailed description can be found in section 6.1.2).

For the characterization of $SrTiO_3$ samples, the surfaces were sputter-coated with platinum and analyzed using a Zeiss XB540 SEM (Carl Zeiss AG, Oberkochen, Germany). The preparation procedure otherwise followed the same general approach as for 8YSZ.

To determine the average grain size, the linear intercept method was adopted using “Lince-Linear Intercept 2.4.2” software (Nichtmetallisch anorganische Werkstoffe, FB 11, TU Darmstadt, Germany). Grain sizes were measured and calculated according to the standard DIN EN ISO 13383-1 with a conversion factor of 1.56 [145].

5.2.2 Thermophysical characterization

For coupled thermal-electrical-structural modeling, key material properties, such as thermo-physical properties (thermal expansion coefficient, specific heat, thermal conductivity), mechanical properties (Young’s modulus and Poisson’s ratio), and electrical

property (electrical conductivity), are typically required. However, the material properties of 8YSZ are relatively underreported in the literature, particularly regarding their dependence on temperature and density. In this study, various standard thermo-physical experiments were conducted to determine these material properties of 8YSZ.

The coefficient of thermal expansion (CTE) was measured using a horizontal dilatometer (DIL 402C, NETZSCH, Germany). Specific heat capacity was determined by the dynamic differential calorimeter (DSC 404 Pegasus NETZSCH, Germany), and thermal diffusivity by laser flash equipment (LFA 427, NETZSCH, Germany). Thermal conductivity was calculated by the following equation:

$$\lambda(T) = \alpha(T) \cdot c_p(T) \cdot \rho(T) \tag{5.1}$$

where λ is thermal conductivity, α is thermal diffusivity, c_p denotes specific heat and ρ is density. Mechanical properties such as Young's modulus and Poisson's ratio were measured using the impulse excitation technique (RFDA, IMCE NV, Belgium), for which an Instron furnace was utilized and assembled with the testing system to perform high temperature measurement. Except for the thermal conductivity, which was measured in argon to avoid oxidation of graphite, all other properties were measured in air. To ensure an accurate representation of the material response during heating, all parameters were determined as functions of temperature. Additionally, the dependence of the thermal conductivity on relative density was also considered in the measurements.

For FS, electrical conductivity is an essential parameter, as changes in electrical resistance signal the onset of flash and determine the amount of the produced Joule heating. In this study, the time-evolving current and voltage values were extracted from the log data of corresponding flash experiments. Using this data, along with the sample geometry, the electrical conductivities can be obtained as time-dependent values. The contact resistance between the electrode and the green bodies was neglected here, as a generous coating of Pt paste was applied in the holes of dog-bone samples to minimize the effect.

For $SrTiO_3$, as well as other materials used in the UHS setup (e.g., copper electrodes and carbon felt), the temperature-dependent thermo-physical properties were directly adopted from the available literature [146–151]. The temperature simulation for $SrTiO_3$ under UHS was verified indirectly through experimental design to ensure model accuracy. The detailed description of the experimental verification of UHS simulation can be found in section 7.2.1. The electrical conductivity of the carbon felt was experimentally measured using standard UHS test runs without any sample, at the maximum currents ranging from 5 to 24 A. All the properties adopted for simulations are summarized in the Appendix (section 10.1).

5.3 Numerical modeling

FEM is a convenient tool to replicate the experimental observation and to study the interaction between the electrical field, temperature profile, and sintering behavior during ECAS. In this study, coupled thermal-electrical-structural models were established. A material constitutive model coupled with a grain growth law was implemented in the FEM simulation to predict the densification and grain growth of 8YSZ during both FS and UHS. Furthermore, to study the effect of high heating rate on densification, the constitutive model was modified to account for pore shape impact and was applied to the study of $SrTiO_3$ during UHS.

5.3.1 Finite element modeling

The FEM models for FS and UHS were developed in the software ABAQUS/Standard (v14, Simulia, Dassault Systèmes). The temperature evolution was simulated based on the general balance equation [152,153], which describes heat transfer within a control volume V enclosed by a surface area S, as expressed below:

$$\int_V \rho_v \, c_p \frac{\partial T}{\partial t} \mathrm{d}V = \int_V \nabla(\lambda \nabla T) \, \mathrm{d}V + \int_V \dot{q}_e \, \mathrm{d}V + \int_S (\dot{q}_{cond} + \dot{q}_{conv} + \dot{q}_{rad}) \mathrm{d}S \qquad (5.2)$$

where ρ_v is the density of the control volume, c_p is the specific heat, T is the temperature, and λ represents the thermal conductivity. $\dot{q}_e$ is the rate of electrical energy due to Joule heating, while $\dot{q}_{cond}$, $\dot{q}_{conv}$, $\dot{q}_{rad}$ denote surface heat flux due to conduction, convection, and radiation, respectively. The relevant equations are embedded within the software and account for the heat generation from Joule heating as well as the different heat transfer processes.

The boundary conditions were defined based on the experimental procedures, as illustrated in **Figure 5.3**. For FS, an initial temperature of 850°C that corresponds to the furnace temperature was set as the predefined temperature field for the dog-bone sample. To ensure current flow through the sample, a current load with the value of current density was applied to the interior of one hole, while a 0 electrical potential was applied to the other hole. The data of current density were obtained by converting the time-evolving current values extracted from the experimental log data, ensuring accurate replication of the experimental conditions. Additionally, radiation and convection heat-transfer interactions were defined on the sample surface. An emissivity coefficient of 0.7 from literature [154–156] was adopted in the numerical studies. The convection coefficient, also known as heat transfer coefficient, was determined by an additional calibration process. This process involved manually adjusting the coefficient to achieve a close match between the simulated

and experimental flash-onset temperatures of 8YSZ under different electric fields. The experimental values of onset temperatures were adopted from the work of Yadav and Raj [68], and the model as well as its boundary conditions used in the calibration were adapted to reflect their experimental setup. Since the 8YSZ powder used in their work was from the same manufacturer as in the current study, the same material properties were applied for both the calibration and subsequent simulations, with the exception of electrical conductivity. For the calibration, electrical conductivity was defined as a function of temperature (up to 800°C) based on the work of Zhang et al. [157]. Eventually, a convection coefficient of 34 W/(m²·K) was calibrated to derive the best consistency with experimental results, thus being used as the input parameter for the subsequent simulations in this study.

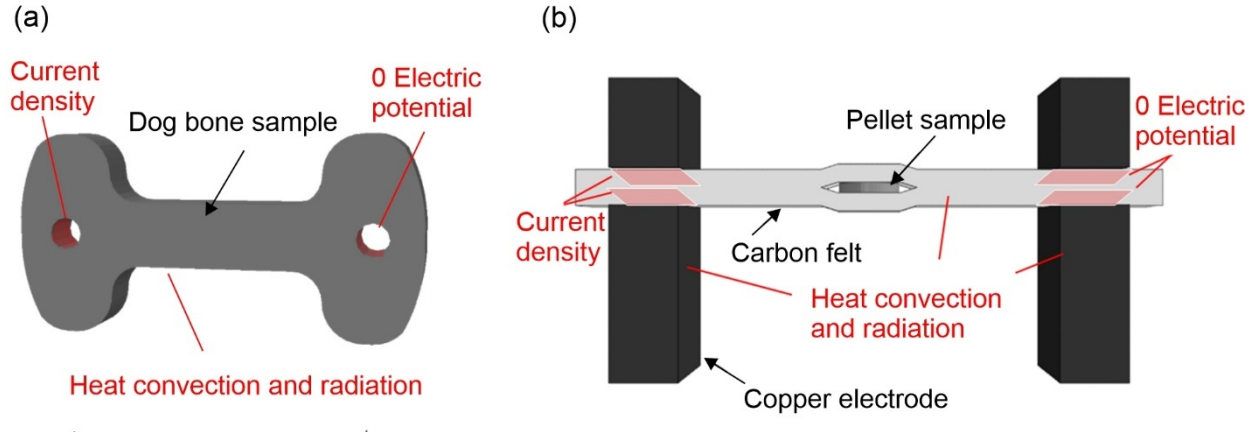

Figure 5.3: Simulation model with defined boundary conditions for (a) FS setup and (b) UHS setup.

As shown in **Figure 5.3b**, the UHS setup of copper electrodes, carbon felt, and the pellet sample was modeled. To simulate the UHS process, a surface current density was applied on one side of the electrode-felt contact surface, while the other side was assigned a boundary condition with an electrical potential of 0 V. Additionally, surface radiation from the carbon felt and copper electrodes was considered, with emissivity values of 0.9 and 0.49, respectively [54,158]. In the case of an inert gas environment (argon), heat conduction was also included. A heat transfer coefficient of 70 W/(m²·K) adopted in the model was obtained by a calibration process that compares the simulated surface temperatures of the felt with that experimentally measured from the pyrometer. During UHS, the carbon felt was stretched out before it was tightly fixed by two copper electrodes with the screws. In this way, a very good contact was ensured both for the electrode-felt and the felt-sample contact surfaces. Therefore, the thermal contact resistance was insignificant, and thus omitted from the model.

For the modeling of CS, where no electric field is present, only the temperature profiles corresponding to the experimental sintering cycles were defined on the sample as boundary conditions.

5.3.2 Constitutive model

A material specific model for 8YSZ was built based on the Skorohod-Olevsky Viscous Sintering (SOVS) model combined with a grain growth law. The original model was rooted in the rheological theory of sintering established by Skorohod [31]. Olevsky later modified the model for numerical simulations based on continuum mechanics [32]. Furthermore, Shinagawa [35,159] introduced an Arrhenius-type function of the viscosity and expressed the sintering stress as a function of density and grain size. These modifications have made the phenomenological constitutive model suitable for describing the densification mechanism during sintering and easily implementable for numerical simulation of ceramic powder sintering [34,160]. According to Shinagawa's adaption, the constitutive equation for inelastic strain rate, derived from Equation 2.4, is formulated as follows:

$$\dot{\varepsilon}_{ij} = \frac{1}{2\eta_0}\frac{1}{\rho^{2n-1}}\left[\sigma'_{ij} + \delta_{ij}\frac{2}{9f^2}(\sigma_m - \sigma_s)\right] \tag{5.3}$$

where ρ is the density, $f = 1/(2.5\sqrt{1-\rho})$, η_0 is the shear viscosity of the fully dense material, n is an exponential constant, σ'_{ij}, σ_m, σ_s represent the deviatoric stress tensor, the hydrostatic stress and the sintering stress, respectively. δ_{ij} is the Kronecker delta. Equation 5.3 and Equation 2.4 are related through the expression for shear and bulk viscosities: $G_e = \eta_0\rho^{2n-1}$ and $K_e = 3f^2\eta_0\rho^{2n-1}$.

The sintering stress σ_s is expressed as a function of grain size and relative density:

$$\sigma_s = \frac{4\gamma_s}{\xi G}\rho^{N_s}\left[\frac{\rho(1-\rho_0)}{\rho_0\,(1-\rho)}\right]^{\frac{1}{3}} \tag{5.4}$$

where γ_s is the specific surface energy, ξ is the correction factor for sintering stress, G is the grain size, N_s is the fitting constant, and ρ_0 is the initial RD. The formulation of viscosity η_0 is adopted from [161] as an Arrhenius-type function:

$$\eta_0 = C_{s1}T\exp\left(\frac{C_{s2}}{T}\right) \tag{5.5}$$

where T is the temperature, C_{s1} and C_{s2} are material constants for viscosity. C_{s2} can be expressed as a function of apparent activation energy for densification Q_d and is given by $C_{s2} = Q_d/R$, where R is the molar gas constant, Q_d indicates the activation energy for the material transport resulting in densification during sintering.

The rate of density change, $\dot{\rho}$, is defined based on the mass conservation equation and is expressed by the trace of the strain rate tensor $\dot{\varepsilon}_{kk}$ as follows:

$$\dot{\rho} = -\rho \cdot \dot{\varepsilon}_{kk} \tag{5.6}$$

In addition to densification, grain growth also plays a significant role in the sintering process. The grain growth law used in this study is shown as follows [37,38]:

$$G^p - G_0^p = Kt = K_0 t \exp\left(-\frac{Q_g}{RT}\right) \tag{5.7}$$

where t is the time, K_0 is the pre-exponential constant, Q_g is the activation energy for grain growth, and p is the grain growth exponent.

With these constitutive equations and the grain growth law, the model was implemented in the user subroutine UMAT of ABAQUS to predict the densification and grain growth during sintering. The viscosity and grain growth parameters were determined by experimental data from isothermal interrupted sintering experiments employing linear regression method.

5.3.3 Constitutive model with pore shape impact

Shinagawa's adaption of the SOVS model was adopted for simulating the densification behavior of 8YSZ. This approach does not explicitly account for any additional mechanisms induced by the ECAS process; instead, it achieves accuracy by fitting kinetic parameters, such as the apparent activation energy for densification Q_d, to experimental observations during ECAS. The altered mechanisms are reflected indirectly in this activation energy. For $SrTiO_3$, however, we modified the original SOVS model to explicitly account for the impact of porosity structure under different sintering conditions. Once the dominant densification enhancement factor was identified from the comparative study of FS and UHS of 8YSZ, the additional effect of this dominant factor—in this case, the ultra-high heating rate—was incorporated to account for pore shape evolution during densification. The goal was to develop a model capable of accurately predicting the sintering behaviors of $SrTiO_3$ for both CS and UHS by addressing the role of heating rates in shaping pore structures.

The development of this model proceeded according to the following routine: First, the original SOVS model was adopted to simulate the conventional dilatometer sintering of $SrTiO_3$. Upon successfully predicting the densification during CS, the model employing the same parameters was applied to simulate UHS to evaluate its applicability. Subsequently, the model was modified to incorporate the dihedral angle θ into the expressions for viscosity modulus and sintering stress. This enables a quantifiable characterization of pore

shape evolution under different heating rates. Finally, the newly developed model was validated using experimental data for both CS and UHS of $SrTiO_3$.

Theory of pore shape impact under UHS and CS

As discussed in section 2.2.2, the ultra-high heating rate (10^3–10^4 K/min) during UHS may be the main factor contributing to rapid densification. The underlying mechanism has been attributed to the bypassing of densification-noncontributing surface diffusion in the low-temperature range and the promotion of grain boundary diffusion. To incorporate this densification-enhancing effect in the constitutive model, we particularly studied the influence of delayed surface diffusion on the pore structure and sintering parameters. Surface diffusion redistributes mass along the pore surface to promote neck growth and spheroidization of pores. Adequate surface diffusion during CS facilitates pore rounding at the early stages of sintering, whereas delayed surface diffusion under ultra-fast heating preserves the reactive microstructures characterized by star-shaped pores with sharp edges [73]. To quantitatively characterize the pore shape evolution during sintering, we introduce the stress intensification factor ϕ and the dihedral angle θ as additional modeling parameters in this work.

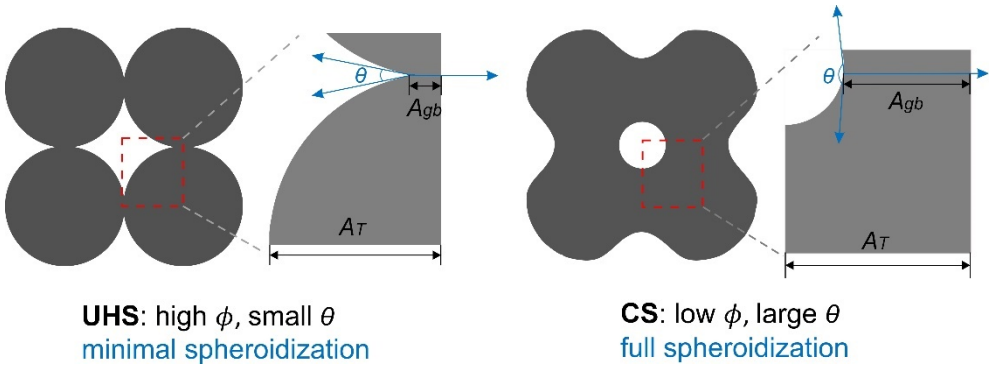

Figure 5.4: 2D scheme of pore structure with minimal and full spheroidization.

The stress intensification factor is defined as the ratio of the total external cross-sectional area of an element unit cell to its grain boundary area, namely $\phi = A_T/A_{gb}$. The dihedral angle θ, which involves the balance of interface energy, forms where a grain boundary intersects the pore. **Figure 5.4** illustrates two contrasting pore shapes formed by four grains. The left figure depicts a microstructure with minimal pore spheroidization, indicative of highly reactive particle contacts. This morphology, characterized by a high ϕ and a low θ, is typical for sintering at ultra-high heating rates such as UHS. On the contrary, the figure on the right, associated more with CS, shows full spheroidization of pores, where surface diffusion effectively rounds the pore geometry, yielding a low ϕ and a high θ. In the present study, simulation of both CS and UHS densification processes is enabled by tuning the

parameter θ. In the case of CS, θ is assigned a value of 180° to describe the full pore spheroidization. For UHS, θ is posited to be minimal during the initial and secondary stages of sintering. As ρ approaches a critical threshold (ρ_c ~ 95%), θ is expected to start increasing until reaching its equilibrium value of 180° at $\rho = \rho_c$. This dynamic variation of θ in UHS is described by the following defined function:

$$\theta = f(\rho) = \left(\frac{1}{\rho_c - \rho}\right)^a + b \tag{5.8}$$

where the constant $a < 1$, and b indicates the minimal starting angle during the evolution of θ. Parameters a and b can be determined through fitting to experimental densification data.

Constitutive equation for CS

Conventional free sintering can be characterized by the linear viscosity function in the SOVS model, as formulated in Equation 2.3 and 2.4. Considering the pressure-less condition for free sintering, a simplified expression can be derived as follows:

$$\dot{\varepsilon}_z = -\frac{\sigma_s}{6\eta_0\psi} \tag{5.9}$$

The effective sintering stress σ_s and the normalized bulk viscosity modulus ψ can be expressed as a function of the relative density ρ [31,32] as given in Equation 5.10 and 5.11. The temperature-dependent shear viscosity η_0 is formulated as an Arrhenius-type equation [35,162] in Equation 5.12, assuming the grain boundary diffusion as the dominant densification mechanism [127,163].

$$\sigma_s = \frac{6\gamma_s}{G}\rho^2 \tag{5.10}$$

$$\psi = \frac{2\rho^3}{3(1-\rho)} \tag{5.11}$$

$$\eta_0 = AT\exp\left(\frac{Q_b}{RT}\right)G^3 \tag{5.12}$$

The term γ_s denotes the specific surface energy, G is grain size, A is the material constant, and Q_b represents the activation energy for grain boundary diffusion. It is important to note that Q_b differs from the previously described apparent activation energy Q_d used for 8YSZ, which reflects the accumulated effect of all the interplayed diffusion mechanisms.

The constitutive model formulated above was adopted to predict the densification behavior during CS of $SrTiO_3$. The viscosity parameters were determined by CS experimental data employing linear regression method.

Modification of viscosity modulus with dihedral angle

The stress intensification factor ϕ is commonly employed in the constitutive model for hot pressing [164]. Based on Equation 2.2, the general expression for the macroscopic strain rate considering grain boundary diffusion as the dominant densification mechanism is formulated below:

$$\dot{\varepsilon}_z = -\frac{HD\phi(\sigma_z + \sigma_s)}{G^3 kT} \tag{5.13}$$

where H is a numerical constant, D is the diffusion coefficient, σ_z and σ_s denote the externally applied stress and the effective sintering stress, respectively. In the work of Manière et al. [73,165], the following relation was derived:

$$A(T, G) = \frac{HD}{G^3 kT} \tag{5.14}$$

The term A, originating from the Norton creep law, has an Arrhenius form and is dependent on temperature and grain size. In the framework of the continuum theory of sintering [32], the linear viscous behavior is represented by $\eta_0 = 1/(2A)$. By using this relationship and equating the solid-state model (Equation 5.13) with the continuum model (Equation 5.9) under a pressure-less scenario ($\sigma_z = 0$), a correlation between the stress intensification factor ϕ and the bulk viscosity modulus ψ is established for free sintering:

$$\phi = \frac{1}{3\psi} \tag{5.15}$$

According to Vieira and Brook's analysis [166] of Beere's work [25], ϕ can be formulated as an exponential function of relative density: $\phi = \exp(\alpha(1-\rho))$, where α is inversely proportional to the dihedral angle θ. Drawing upon these studies, we can eventually derive the relationship between bulk viscosity modulus ψ and dihedral angle θ as follows:

$$\psi = \left[3\exp\left(\frac{740(1-\rho)}{\theta}\right)\right]^{-1} \tag{5.16}$$

Equation 5.16 is adopted in the current study to modify the constitutive model, reflecting the influence of pore structure on the bulk viscosity modulus. A reduced θ, indicating a lower degree of pore spheroidization, yields a diminished ψ, consequently accelerating the densification process. However, when the density exceeds a critical value ρ_c and reaches full densification ($\rho \to 100\%$), the bulk viscosity modulus ψ calculated from Equation 5.16 approaches an unrealistically small finite value. To model the sintering behavior more precisely, the Skorohod expression for ψ, extended with green density ρ_0 [73,167], is adopted for the stage where $\rho > \rho_c$, as shown in Equation 5.17.

$$\psi = \frac{2}{3}\frac{(\rho - \rho_0)^r}{1-\rho} \tag{5.17}$$

From this equation it is evident that as ρ reaches 100%, ψ becomes infinite. The exponent r is fitted to a value that ensures ψ coincides with Equation 5.16 at $\rho = \rho_c$.

Modification of sintering stress with dihedral angle

To characterize the sintering behavior under the high heating rate, the sintering stress formulation proposed by Shinagawa [35,159] is employed, as indicated in Equation 5.18. Here, N_s is a constant, γ_s is the surface energy, and $\bar{r}$ is the effective pore radius which depends on the relative density. To integrate the dihedral angle θ into the sintering stress, the grain-boundary energy contribution to the sintering stress should not be neglected. To this end, we extended Shinagawa's sintering stress to include the grain boundary energy term γ_b, as shown in Equation 5.19. With its correlation to the dihedral angle: $\cos(\theta/2) = \gamma_b/2\gamma_s$, the modified sintering stress can finally be formulated as in Equation 5.20.

$$\sigma_s = \rho^{N_s}\frac{2\gamma_s}{\bar{r}} \tag{5.18}$$

$$\sigma_s = \rho^{N_s}\left(\frac{2\gamma_s}{\bar{r}} + \frac{2\gamma_b}{\mathrm{G}}\right) \tag{5.19}$$

$$\sigma_s = \frac{4\gamma_s}{G}\rho^{N_s}\left\{\frac{1}{\xi}\left[\frac{\rho(1-\rho_0)}{\rho_0\,(1-\rho)}\right]^{\frac{1}{3}} + cos\frac{\theta}{2}\right\} \tag{5.20}$$

where ξ is the correction factor for sintering stress.

Exaggerated grain growth was observed for $SrTiO_3$ after UHS [76]. This was attributed to the extremely high rate of grain boundary migration and pore-grain boundary separation. To account for the effect of grain growth on densification, the same grain growth law used for 8YSZ (Equation 5.7) is adopted. Based on prior research [168], and considering that grain growth becomes pronounced only after a substantial level of densification is achieved ($\rho > 96\%$ [76]), the grain growth exponent $p = 2$ is applied in the study of $SrTiO_3$.

6 Experimental results

6.1 Experiments of 8YSZ

This section presents the results of experimental investigations conducted on 8YSZ. The experimentally measured thermophysical properties are introduced first. Then, the sintering results of 8YSZ, including densification and grain growth during CS, FS, and UHS, are presented. The densification and grain growth kinetics are analyzed using linear regression plots, with the activation energies for densification and grain growth determined. Finally, different sintering methods are compared, and the potential densification enhancement mechanisms during FS and UHS are proposed.

6.1.1 Thermophysical characterization

The thermophysical properties of 8YSZ samples, including specific heat, thermal diffusivity, and CTE, have been measured using individual thermophysical experiments detailed in section 5.2.2. These properties were measured as functions of temperature and plotted in **Figure 6.1**. Additionally, thermal diffusivity was measured at four different relative densities (RD) to study the influence of density, and thermal conductivity was calculated subsequently using Equation 5.1. This result is shown in **Figure 6.1c.**

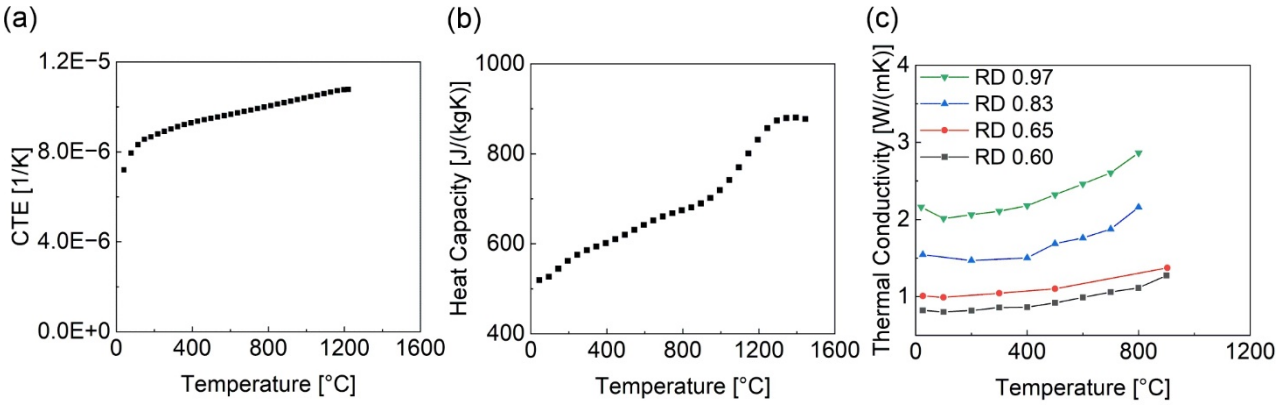

Figure 6.1: Thermophysical properties of 8YSZ as a function of temperature with (a) the coefficient of thermal expansion (CTE), (b) specific heat capacity, and (c) thermal conductivity at different relative densities (RD).

The plotted results show that all the thermo-physical properties increase with temperature, while an increase in density enhances thermal conductivity. The CTE curve shows an initial nonlinearity up to ~200 °C, primarily due to thermal lag and measurement artifacts in the dilatometer. Because 8YSZ is partially transparent to infrared radiation at high temperatures, thermal diffusivity measurements are limited to 900 °C. For temperatures above this limit, the values are extrapolated and used for modeling purposes.

For mechanical properties, Young's modulus has been measured as a function of temperature and is shown in **Figure 6.2**. The value initially decreases with increasing temperature and then rises. This transition occurs at approximately 600°C, which can be explained by the phase transition of 8YSZ from the metastable tetragonal phase to the cubic phase at this temperature [169]. The Poisson's ratio was determined to be 0.273 at room temperature, with only a very limited increase observed at elevated temperatures.

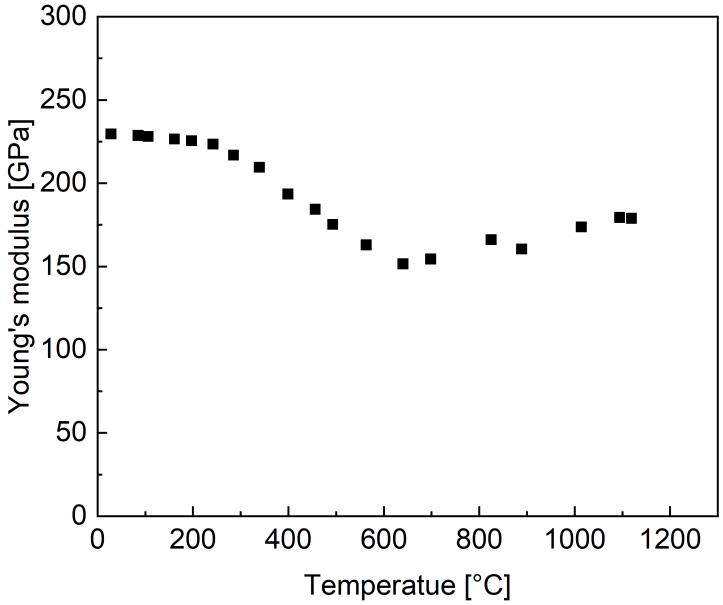

Figure 6.2: Young's modulus of 8YSZ as a function of temperature.

The determined values have been implemented as tabular data into ABAQUS, and all the measured properties are summarized in the Appendix (section 10.1). Given the challenges in measuring electrical conductivity of 8YSZ at high temperatures, the electrical conductivity data were derived from the time-evolving current and voltage values extracted from the log data of corresponding flash experiments. These calculated values were defined as time-dependent parameters in ABAQUS for simulations.

6.1.2 Sintering and microstructural characterization

Conventional Sintering (CS)

Figure 6.3 shows the shrinkage curves and their corresponding RD curves of dilatometer sintering experiments in air. It can be seen that the samples sintered at 1300°C for 2 h achieved almost full densification. The sintering trajectory of 8YSZ can be obtained from the isothermal interrupted CS experiments by plotting grain size against RD for different sintering temperatures and dwell times (**Figure 6.3b**). The number at each colored point corresponds to the dwell time (min), and the sintering temperatures are indicated by

different colors. It can be deducted from the graph that only neglectable grain growth appears for a RD below 92%, above which the grains start to grow significantly. When the density reaches the maximum and stabilizes, the grains continue to grow with the increase of the dwell time.

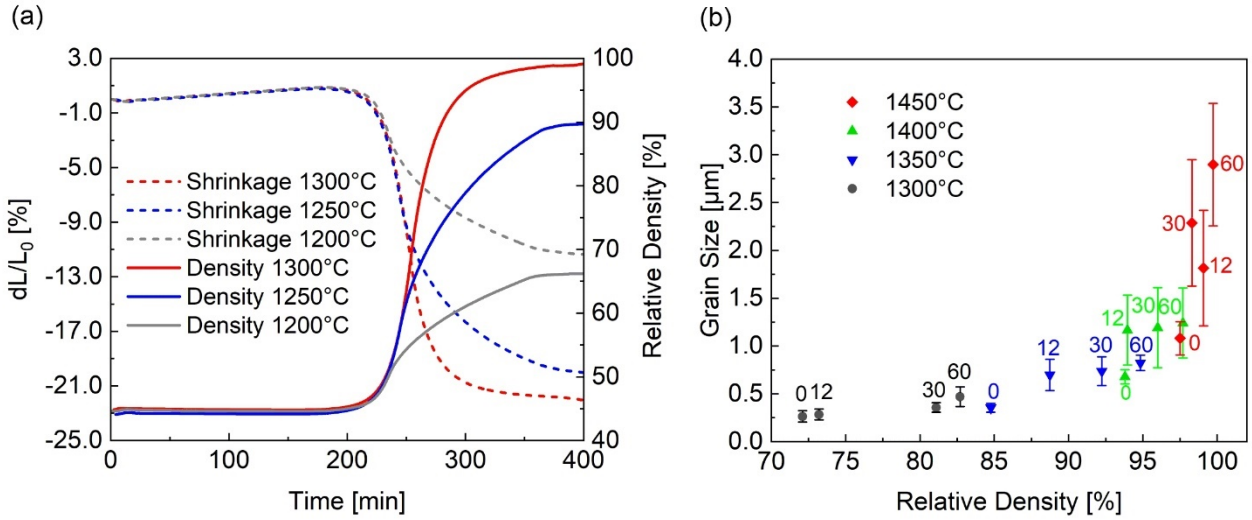

Figure 6.3: Experimental results for CS of 8YSZ: (a) sintering shrinkage and RD as a function of time; (b) sintering trajectory at different sintering temperatures and with different dwell times. The dwell time (min) is indicated by the number at each colored point.

The measured grain sizes for conventional isothermal sintering experiments are plotted as a function of dwell time, as shown in **Figure 6.4**. It shows that for the given dwell times, significant grain growth only occurred at a temperature above 1300°C. The evolution of the grain sizes of the samples sintered at 1350°C with four different dwell times is further illustrated by the SEM micrographs in **Figure 6.5.**

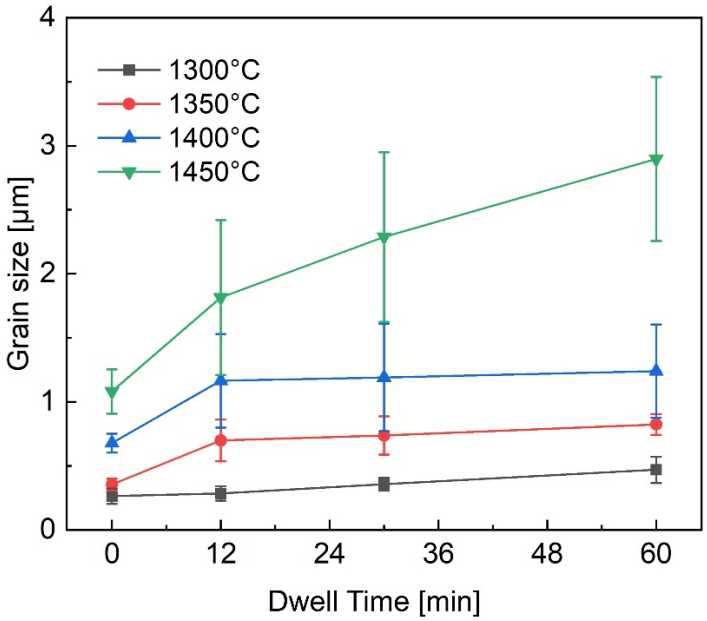

Figure 6.4: Grain sizes of 8YSZ samples sintered by CS at temperatures ranging from 1300°C to 1450°C and dwell times of 0, 12, 30, and 60 min.

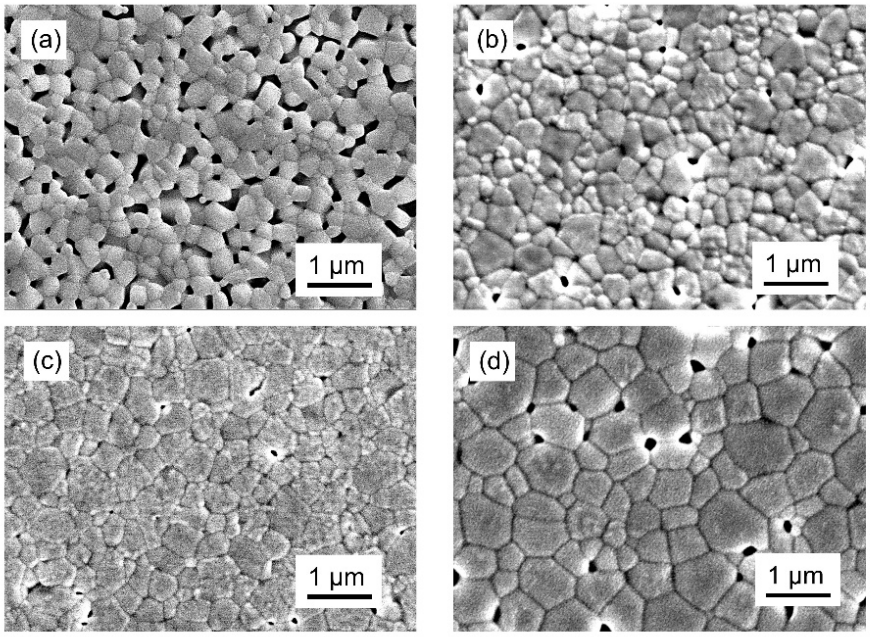

Figure 6.5: Microstructural evolution of 8YSZ samples conventionally sintered at 1350°C for (a) 0 min, (b) 12 min, (c) 30 min, and (d) 60 min.

Flash Sintering (FS)

For FS, the measured densities of flash-sintered samples are plotted against current densities in **Figure 6.6a**. The highest RD of ~95% was reached at the current density of 100 mA/mm² with the dwell time of 120 s, as well as at 125 mA/mm² for all dwell times. Some abnormal values are observed in the graph. For instance, for the dwell times of 30 s and 60 s, the RD at 75 mA/mm² is larger than that at 100 mA/mm². This deviation is primarily attributed to the divergence of the sample temperatures at the same current density. During FS experiments, the dissipated power density was found to fluctuate across experiments, even when the same current density was applied. This inconsistency led to variations in the sample temperatures, with simulated differences of up to 100 K at high current densities. While the exact cause of this deviation remains unclear, it is likely due to factors such as electrical contact resistance and systematic errors in the device and setup.

As a result, temperature rather than current density is considered more relevant for analyzing densification behavior. For future analysis, the temperatures of the gauge sections of the dog-bone samples during the isothermal period were extracted from simulations. The values are averaged and subsequently adopted as the sintering temperature for each FS experiment. The plot of RD as a function of temperature can be then constructed in **Figure 6.6b**. Notably, the deviation in RD at 100 mA/mm² for 30 s and 60 s observed in **Figure 6.6a** is mitigated in **Figure 6.6b**. The diagram reveals that at around 1400°C, the maximum RD of around 95% can be achieved within just 15 s by FS.

This demonstrates the capability of FS to significantly accelerate the sintering process and achieve high densification in 8YSZ samples.

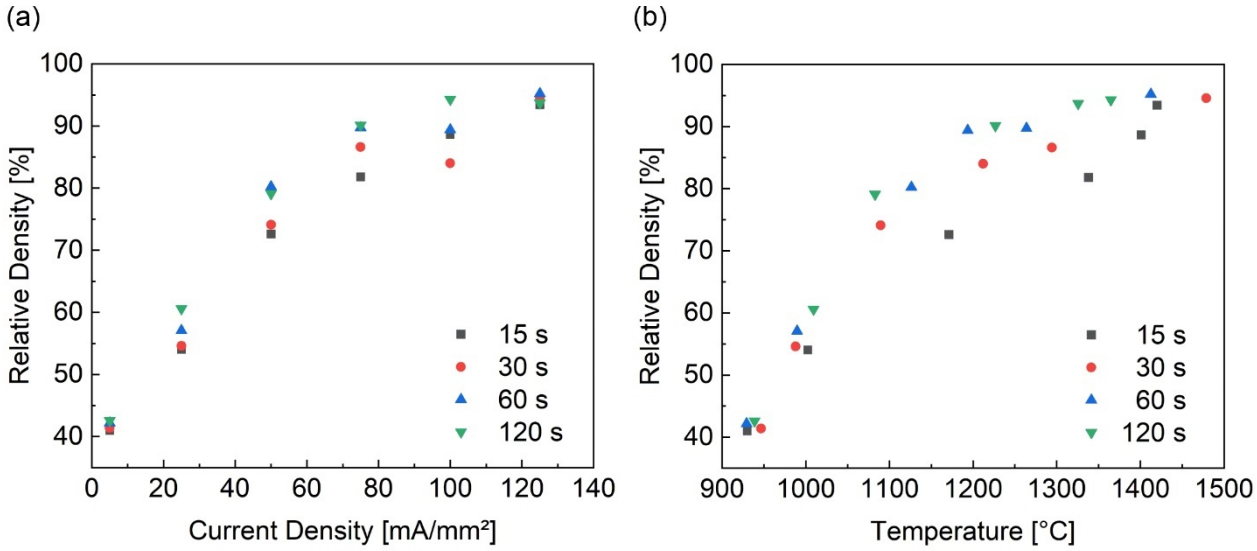

Figure 6.6: RD of flash-sintered 8YSZ samples: (a) RD as a function of current density; and (b) RD as a function of temperature. The temperatures are simulated average temperatures of the gauge sections of the dog-bone samples during the isothermal period.

To characterize the grain size distribution in the flash-sintered dog-bone samples, the microstructure at three different positions (position A, B, and C) were analyzed as shown in **Figure 6.7a**. The measured mean grain sizes of the sample flash sintered at 50, 100 and 125 mA/mm² for 30 s are plotted for each position in **Figure 6.7c**. The figure indicates a gradual decrease of grain size from the position near the anode side to that near the cathode side. Although the grain sizes are almost the same at different positions for the sample sintered at 50 mA/mm², the gradient enlarges with increasing current densities.

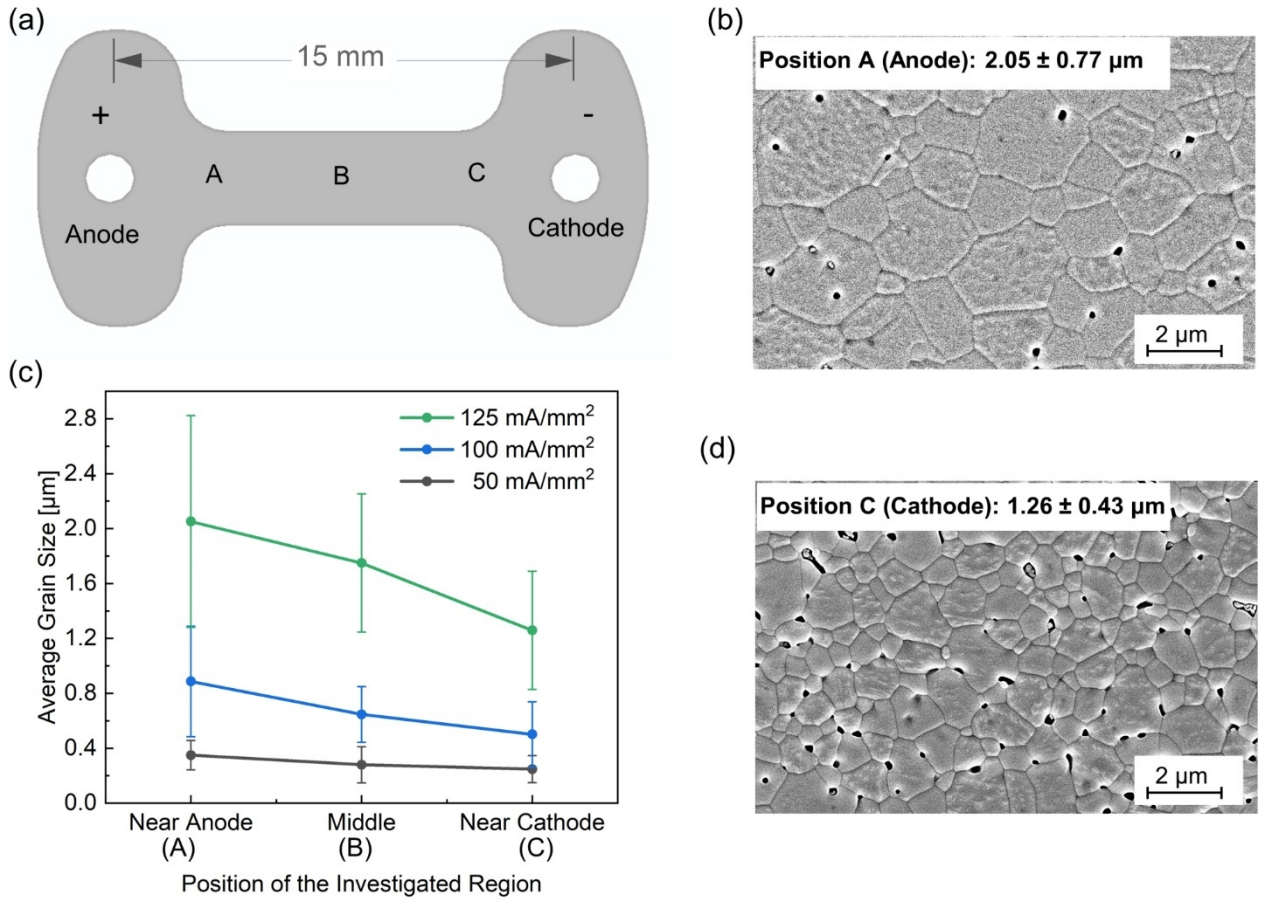

Figure 6.7: Grain size analysis for flash-sintered 8YSZ samples: (a) schematic representation of the measured positions of the gauge section (15 mm) of dog-bone shaped samples; (b) microstructure at position A (near anode) of the sample flash sintered at 125 mA/mm² for 30 s; (c) grain sizes at position A, B, and C (corresponding to the positions on the dog-bone sample) at different current densities for the dwell time of 30 s; (d) microstructure at position C (near cathode) of the sample flash-sintered at 125 mA/mm² for 30 s.

The micrographs at the positions close to the anode side (position A) and the cathode side (position C) of the sample flash sintered at 125 mA/mm² for 30 s are shown in **Figure 6.7b** and **Figure 6.7d**. The sample has a RD of 95% and the grain size varies from 1.26 to 2.05 µm from the cathode side to the anode side. They are comparable to the grain sizes of conventionally sintered samples at similar densities. For example, the sample conventionally sintered at 1400°C for 30 min has a RD of 96% and a grain size of 1.63 µm.

Ultrafast high-temperature sintering (UHS)

In this study, interrupted isothermal UHS experiments with dwell times of up to 2 min were conducted to obtain the modeling parameters. The relative densities of the pellet samples were measured after the sintering experiments, and the results are given in **Figure 6.8**. For convenience, the simulated sample average temperatures corresponding to each current are indicated on the top axis of the figure. The results show that, for a dwell time above 1

min, nearly complete densification (RD > 97%) can be achieved at the maximum current of 13 A, which corresponds to a simulated average sample temperature of 1439°C. At the maximum current of 15 A, 8YSZ sample can be densified in just 30 s.

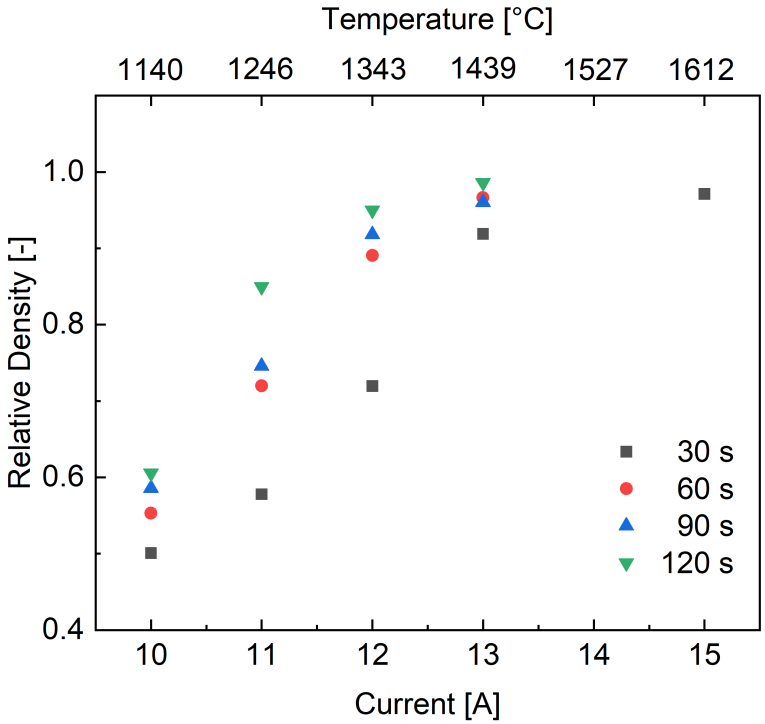

Figure 6.8: Experimental results of RD of UHS-sintered samples at different maximum currents and dwell times. Pre-sintered green bodies had a RD of 45% ± 2%. The top axis indicates the simulated average temperatures of the samples.

For comparison, dilatometer sintering experiments with a heating rate of 5 K/min were carried out on 8YSZ samples in argon. The results show that a RD of ~ 95% for the 8YSZ sample can be achieved by sintering at 1450°C with no holding time. This is similar to the sample temperature at the maximum current of 13 A during UHS, although a much longer total processing time was required for CS (~ 10 h) compared to UHS (< 20 min). It is worth noting that most of the processing time of UHS is for evacuation and filling the chamber with argon (~ 16 min). The total cycle time could be reduced to a few minutes by using a stronger vacuum pump and a higher argon flow rate.

From the comparison of UHS and CS, it can be concluded that no extra-high sample temperature played a role in the densification of 8YSZ during UHS. Since the samples were heated solely by thermal conduction and radiation, the influence of electric field can also be excluded. Thus, the ultra-high heating rate appears to be the dominant factor that enhances densification. The effect of ultra-high heating rate on densification will be discussed in detail in later chapters.

The measured grain sizes for 8YSZ samples sintered by UHS at currents between 11 A and 13 A with dwell times of 30, 90, and 120 s are plotted in **Figure 6.9**. Moreover, the microstructures at the center of the polished and etched cross-sections of the samples for 120 s are shown in **Figure 6.10**. It can be seen from the figures that the average grain size of the 8YSZ sample increases with increasing current for the same dwell time, and the grain continues to grow with increasing dwell time. At 13 A for 120 s, the sample was almost fully densified with a grain size of 1.9 µm, which is comparable to the grain size of the conventionally sintered 8YSZ samples. The grain growth behavior during UHS reveals that the rapid densification is unlikely due to a fine-grained microstructure caused by the ultra-high heating rate.

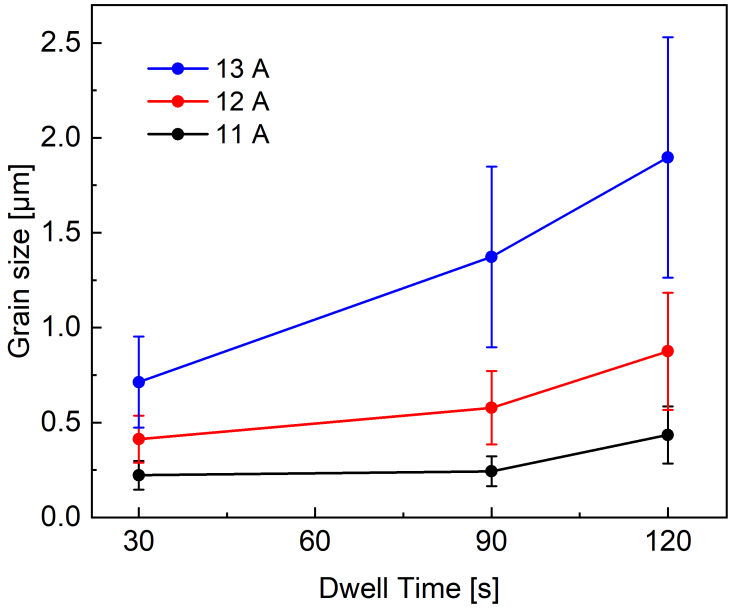

Figure 6.9: Grain sizes of 8YSZ samples sintered by UHS at maximum currents between 11–13 A and dwell times between 30–120 s.

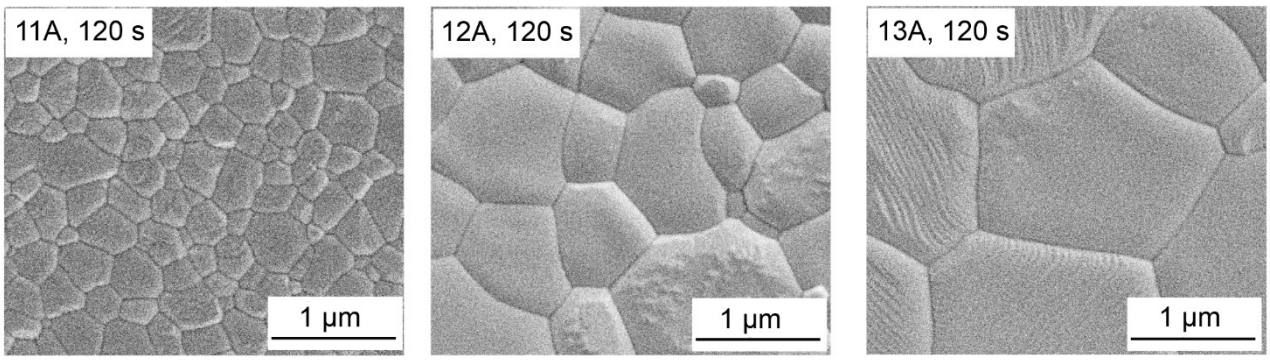

Figure 6.10: SEM micrographs of the UHS-sintered 8YSZ samples at the maximum currents of 11 A, 12 A, and 13 A for 120 s in argon atmosphere.

6.1.3 Densification kinetics

Since there is only minor grain growth for 8YSZ samples with a RD below 92%, constant grain sizes were assumed at early stages of sintering. Only the experimental data of the RD smaller than 92% were utilized for the characterization of the densification behavior and the determination of exponential parameters for densification. For the calculation of densification, considering the case of pressure-less sintering with isotropic shrinkage, the strain rate can be formulated as Equation 6.1. With the substitution of σ_s, η and f, Equation 6.2 can be then obtained. The parameters m, N_S, and n are density exponents. To determine m (Equation 6.3), Equation 6.2 was rewritten as the double logarithmic form given in Equation 6.4, where K_1 and K_2 are constants. By keeping the temperature T invariable and assuming a constant grain size G in our case, the left-hand side of Equation 6.4 against $ln\,\rho$ can be plotted.

$$\dot{\varepsilon}_{kk} = -\frac{\dot{\rho}}{\rho} = -\frac{1}{2\eta} \cdot \frac{1}{\rho^{2n-1}} \cdot \frac{2\sigma_s}{9f^2} \tag{6.1}$$

$$\frac{\dot{\rho}}{\rho} = \frac{K_1}{C_{s1} T\, exp\left(\frac{Q_d}{RT}\right) G} \cdot \rho^m \cdot (1-\rho)^{\frac{2}{3}} \tag{6.2}$$

$$m = N_S - 2n + \frac{4}{3} \tag{6.3}$$

$$ln\left[\frac{\dot{\rho}}{\rho} \cdot \frac{1}{(1-\rho)^{\frac{2}{3}}}\right] = m\, ln\,\rho + K_2 \tag{6.4}$$

$$ln\left[T \cdot \frac{\dot{\rho}}{\rho} \cdot \frac{1}{\rho^m (1-\rho)^{\frac{2}{3}}}\right] = -\frac{Q_d}{RT} + K_3 \tag{6.5}$$

The double logarithmic plots for the DIL sintering at the temperatures of 1200°C, 1250°C, and 1300°C are shown in **Figure 6.11a**. The results showed a linear feature and were fitted by a linear function with a slope representing the parameter m. The average value of m was calculated to be -4.69 ± 1.00. After the calculation of exponential parameters, the apparent activation energy for densification Q_d was determined. Equation 6.2 was rewritten in the logarithmic form as shown in Equation 6.5. The left-hand side of the equation is plotted as a function of $-1/T$ in an Arrhenius plot (**Figure 6.11d**), the dwell time of 10, 20, and 30 min were chosen for the curves to ensure that the RD is below 92%. From the slopes of the curves, the average activation energy for densification can be obtained as 691 ± 20 kJ/mol.

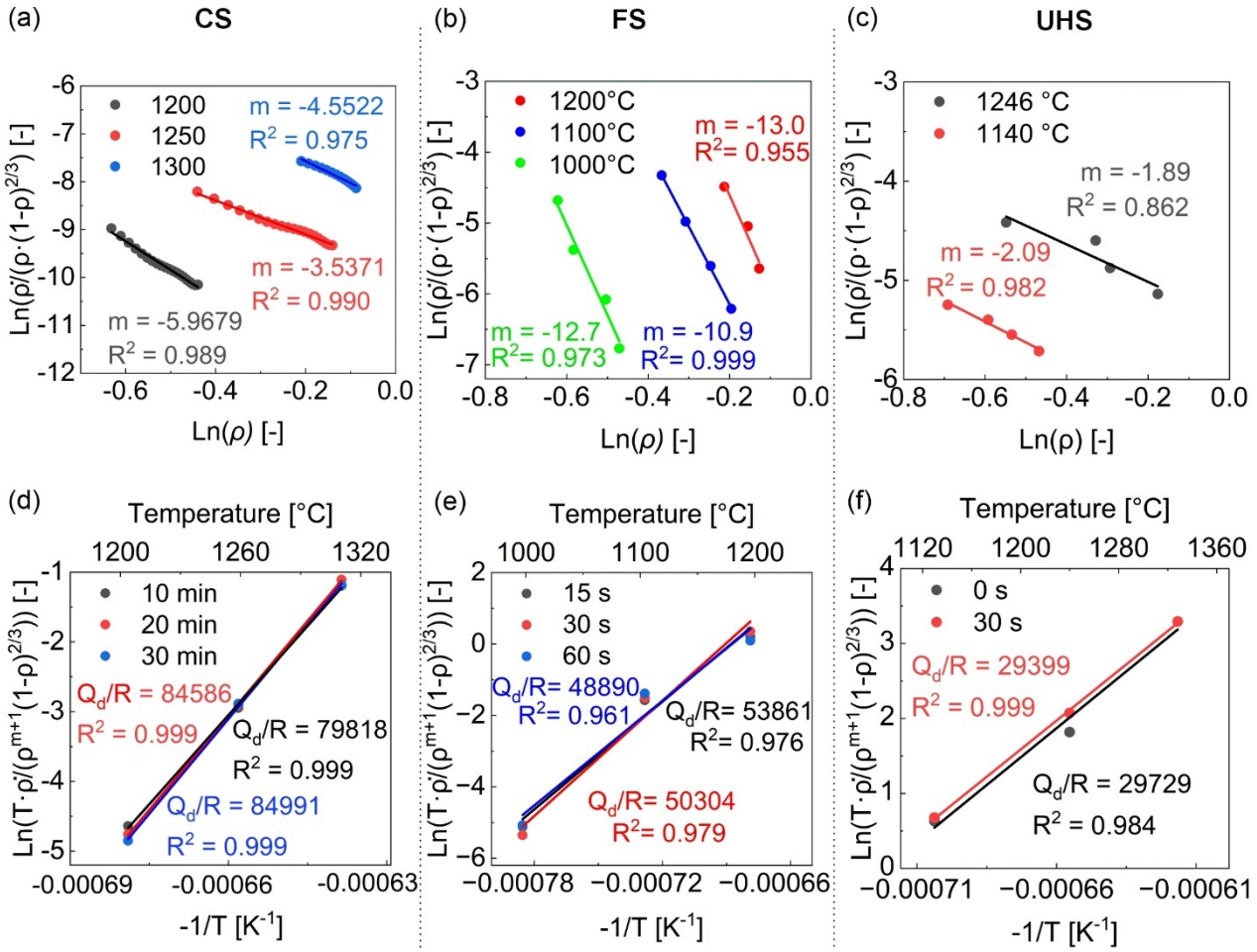

Figure 6.11: Parameter identification for densification: Determination of parameter m and the apparent activation energy of densification Q_d for (a, d) conventional sintering (CS); (b, e) flash sintering (FS); and (c, f) ultrafast high-temperature sintering (UHS).

The same strategy was employed to identify the exponential parameter m and the activation energy for densification Q_d for FS. Unlike the DIL sintering experiments, in-situ shrinkage under isothermal conditions could not be measured during FS experiments. Therefore, interrupted isothermal experiments were designed to obtain densification curves as a function of dwell time, from which the densification rate can be derived. However, the isothermal condition is hard to fulfill across different experiments even using the same current density. As explained earlier, a scatter of the temperature occurs for identical current densities, as can be seen in **Figure 6.6**. Although the temperature deviation was not substantial, a fitting strategy for the densification curves was employed to ensure a more accurate parameter identification process. Density values at 1000°C, 1100°C and 1200°C were extracted from the fitted curves for the identification process. The detailed procedure for this fitting strategy is described in the Appendix (section 10.2).

Using the extracted densification data at these three temperatures, the parameter m and the apparent activation energy for densification Q_d were determined in the same manner

as for CS. The linear regression plots are shown in **Figure 6.11b** and **Figure 6.11e**. The average value of m was calculated to be -12.19 ± 0.90, and the activation energy Q_d was determined to be 424 ± 17 kJ/mol.

For UHS, a similar identification process was applied. To ensure that no prominent grain growth occurred in the selected experiments for parameter identification, only the data from 10 A (1140°C) and 11 A (1246°C) were adopted to determine the parameter m (**Figure 6.11c**), and the data from 0 s and 30 s were used to determine Q_d (**Figure 6.11f**). It should be noted that the time here refers to the real dwell time, which differs from the set dwell time (total sintering time) used in **Figure 6.8**. The real dwell time is calculated by subtracting the heat-up time (~30 s) from the set dwell time. Unlike FS, no fitting was required for UHS since the current input remained relatively stable and consistent across different experiments.

The value of m for UHS was calculated to be -1.99 ± 0.10, and the activation energy for the densification Q_d was 246 ± 1 kJ/mol. It can be seen from **Figure 6.11** that most of the coefficients of determination (R^2) fall within the range of 0.97–1.00, which indicates a good fit between the data and the linear regression line.

6.1.4 Grain growth kinetics

The grain growth law (Equation 5.7) can be rewritten to its double logarithmic form in Equation 6.6. Using the measured grain sizes at different temperatures and dwell times, linear regression plots can be constructed to determine the activation energy for grain growth. The value of grain growth exponent p was taken as 2 according to the literature [170] for 8YSZ.

$$\ln(G^p - G_0^p) = -\frac{Q_g}{RT} + lnK_0 + \ln t \tag{6.6}$$

Figure 6.12 shows linear regression plots for CS and UHS. The grain sizes were measured at the center of each sintered sample. For UHS, the simulated temperatures at the sample center were used for linear regression analysis. The activation energy Q_g can be determined by the slope of the fitted linear curves. The average value for the activation energies at different temperatures was calculated to be 575 ± 30 kJ/mol for CS and 405 ± 67 kJ/mol for UHS.

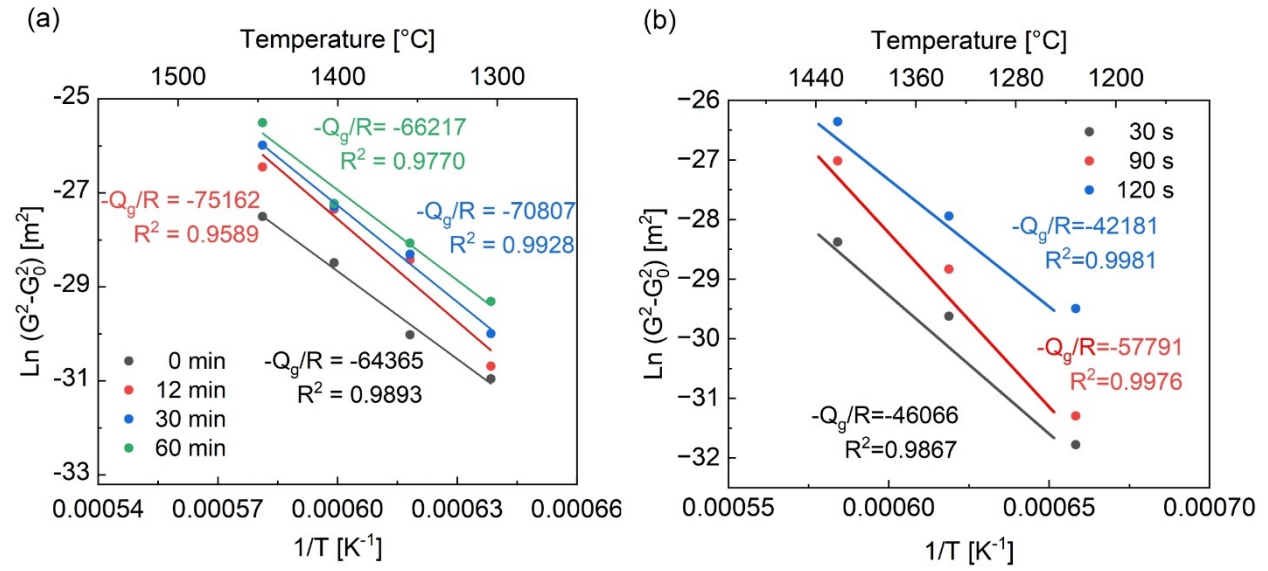

Figure 6.12: Determination of activation energy Q_g for grain growth for (a) conventional sintering (CS) and (b) ultrafast high-temperature sintering (UHS).

For FS, different activation energies for grain growth were assumed at different positions of the dog-bone sample due to the electrical polarity. Therefore, the aforementioned parameter identification method was used to determine Q_g at three different positions of the dog-bone samples, namely near the anode, in the middle, and near the cathode, which are labeled as positions A, B, and C in **Figure 6.7a**. A similar approach to the current work has been utilized to model the asymmetrical microstructure during FAST/SPS of GDC [171]. The temperatures were extracted from the simulation models at each corresponding position on the dog-bone sample for the analysis. The linear regression plots are shown in **Figure 6.13** for positions A (anode), B (middle), and C (cathode). The average activation energies of 173 ± 5, 189 ± 12, and 197 ± 14 kJ/mol were obtained for the anode, middle, and cathode regions, respectively.

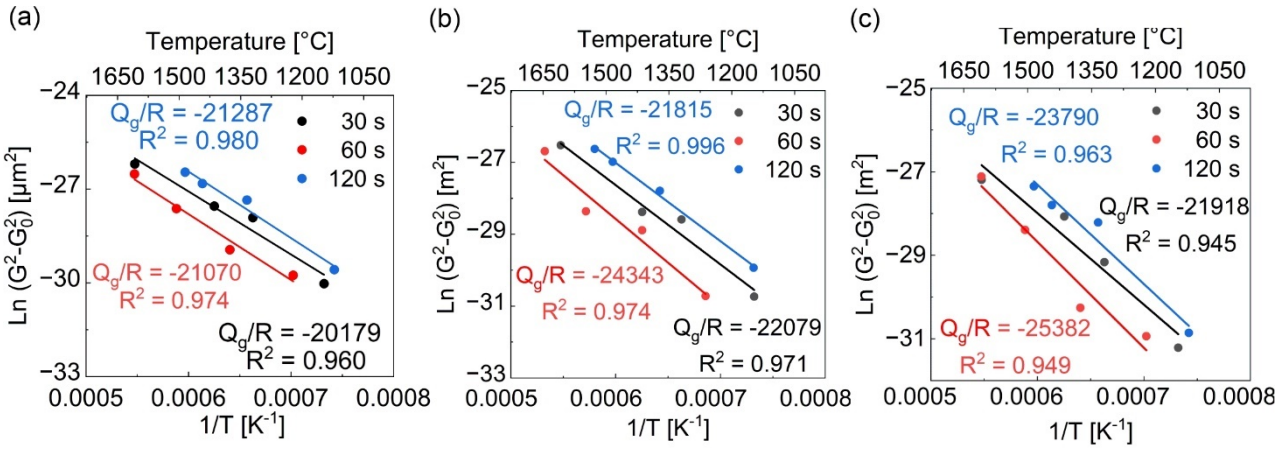

Figure 6.13: Determination of activation energy Q_g for grain growth for flash sintering (FS) near the (a) anode, (b) middle, and (c) cathode side of the sample during FS.

6.1.5 Comparative study and interim summary

UHS and FS exhibit comparable heating rates and are both capable of densifying ceramic materials within tens of seconds. The primary difference between the two techniques lies in their heating mechanisms. In UHS, the sample is heated through thermal radiation and conduction (indirectly by the electric field), whereas in FS, the current flows through the green body, heating the sample via Joule heating induced directly by the electric field. This distinction provides a foundation for comparing the roles of the heating rate and electric field on the sintering behavior of 8YSZ, specifically on densification and grain growth.

Sintering trajectories

The sintering trajectories of the 8YSZ samples sintered by FS, UHS, and CS are plotted in **Figure 6.14**. Grain sizes were measured at the center of the samples for all the sintering methods to exclude the effect of electrical polarity. The RD values represent averages across the entire sample or the gauge section. It can be seen from **Figure 6.14b** that the trajectories of CS and UHS align closely, while a slight difference in the slope of the trajectory is observed between FS and UHS (**Figure 6.14a**). At the RD above 85%, FS shows a steeper trajectory slope than UHS, indicating an early start of grain growth, and thus a more evident grain coarsening and limited densification. While this difference could be attributed to limitations in measurement precision, it can, nevertheless, be explained by the final densities of the sintered samples: UHS achieved a maximum RD of 98.6%, whereas FS reached only 95%.

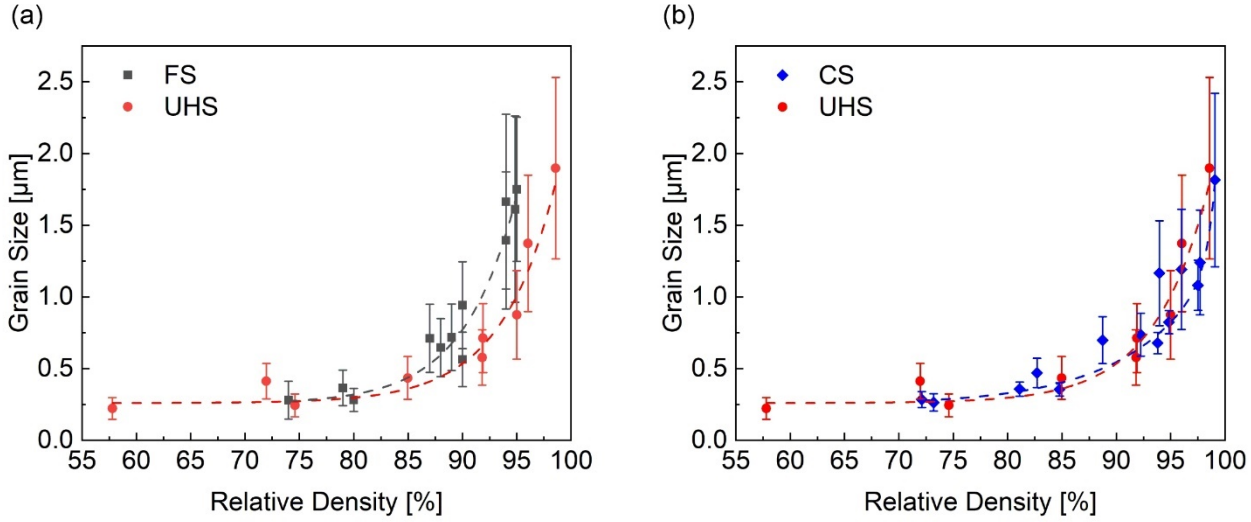

Figure 6.14: Comparison of sintering trajectories of 8YSZ: (a) flash-sintered in air and UHS-sintered in argon; (b) conventionally sintered in air and UHS-sintered in argon.

Several factors may influence the sintering trajectory of 8YSZ, including heating rate, sintering atmosphere, and electric field. According to the temperature simulation, the

average heating rate of UHS of 8YSZ does not exceed the heating rates observed in FS. Therefore, the less grain coarsening observed in UHS cannot be explained by the suppression of grain growth due to a higher heating rate. Regarding the sintering atmosphere, previous studies [172–176] have shown its influence on the sintering behavior of various ceramic materials. For example, Yan et al. [173] found that a reducing atmosphere produces larger grain sizes in $BaTiO_3$, and that the grain boundary mobility of Fe_3O_4 is inversely proportional to the square root of the partial pressure of O_2. In contrast, Ubenthiran et al. [176] reported that 3YSZ samples sintered in argon exhibited smaller grain sizes but reduced densities compared to those sintered in air. We constructed a sintering trajectory from the work of Ubenthiran et al., and it shows that atmosphere has minimal influence on the sintering trajectory of 3YSZ. The contradiction in these studies is attributed to variations in material systems and defect mechanisms. However, in either case, a reduced atmosphere does not exhibit the ability to lower the sintering trajectory slope that delays grain growth while maintaining the same density levels. Therefore, the oxygen-deficient argon environment in UHS cannot explain the smaller grain sizes achieved compared to FS either.

Based on the discussion above, the most plausible explanation for the observed differences in sintering trajectories can be attributed to the effect of the electric field, which was applied to the sample in FS and absent in UHS. Electric fields have been reported to be able to redistribute point defects and change the grain boundary mobility at the electrode sides during FS [61,177]. Since microstructural analyses in this study focused on the sample center, the effect of the electric field likely extended across the entire sample during FS, contributing to the distinct grain growth behavior.

Ultra-high heating rates

To isolate the influence of heating rate, densification data for FS and UHS of 8YSZ were compared to those of CS conducted under the same atmosphere and similar sintering temperatures. **Table 6.1** compares FS and CS of 8YSZ in air, while **Table 6.2** compares UHS and CS of 8YSZ in argon. To study the effect of the heating rate across different sintering stages, various temperature ranges were selected for comparison. For CS in argon, the densification curves were derived from shrinkage data obtained through DIL experiments. Corresponding densities were extracted from these densification curves based on the chosen temperatures and holding times. The temperatures listed for FS and UHS are simulated values, chosen to match those of CS. It is important to note that the dwell times listed for UHS in the table represent the real dwell times of the samples, rather than the set dwell times (total sintering times) of the experimental procedure. Considering

the heat-up times of the samples before their highest temperatures were reached, the real dwell times were obtained by subtracting the heat-up times from the set dwell times during the experiments. The heat-up time was assumed to be approximately 30 s during UHS based on the simulation results.

Table 6.1: Comparison of conventional sintering (CS) and flash sintering (FS) at similar temperatures in air

CS (air)				FS (air)			
Temp. [°C]	Dwell Time [s]	Heating Rate [K/min]	RD [%]	Temp. [°C]	Dwell Time [s]	Heating Rate [K/min]	RD [%]
1200	60	5	52.9	1171	15	3012	72.6
1300	60	5	71.7	1294	30	2892	86.6
1350	120	5	88.7	1326	120	1393	93.7

Table 6.2: Comparison of conventional sintering (CS) and ultrafast high-temperature sintering (UHS) at similar temperatures in argon

CS (argon)				UHS (argon)			
Temp. [°C]	Dwell Time [s]	Heating Rate [K/min]	RD [%]	Temp. [°C]	Dwell Time* [s]	Heating Rate [K/min]	RD [%]
1102	0	5	45.3	1102	0	2573	57.8
1224	0	5	51.4	1224	0	2759	72.0
1335	0	5	71.9	1335	0	2976	91.9
1250	7200	5	77.8	1246	90	2573	85.0

* The dwell times for UHS refer to the real dwell time of the samples.

Table 6.1 shows that FS achieves higher densification than CS with relatively lower sintering temperatures and shorter holding times. This observation indicates that the enhanced densification during FS of 8YSZ is not a result of extra-high sintering temperatures. Considering the significantly higher heating rate during FS (> 1000 K/min) compared to CS (5 K/min), it is likely that the ultra-high heating rate in FS plays a major role in the enhanced densification. However, the role of electric field in FS cannot be completely excluded in this comparative analysis.

Similarly, **Table 6.2** reveals that even in the absence of an electric current, pronounced increases in relative densities can still be achieved. UHS densified 8YSZ samples to a much higher degree at the same temperatures and with the same or shorter holding times compared to CS. By comparing the conclusions drawn from **Table 6.1** and **Table 6.2**, it is clear that our results support the theory of the heating rate effect: the enhanced densification observed in both FS and UHS is primarily due to the ultra-high heating rate. This conclusion aligns with the fundamental works of Harmer et al. [178] from the early

1980s. As for the electric field, its influence in FS is more significant for grain growth rather than densification.

Furthermore, by comparing the densification curves for CS of 8YSZ in air and argon, it can be concluded that the 8YSZ samples are more easily densified in air than in argon. This finding highlights the importance of sintering atmosphere in the densification process of 8YSZ.

Activation energies for densification and grain growth

The parameters for apparent activation energy of 8YSZ obtained from linear regression plots are summarized in **Table 6.3**. These parameters were used in the subsequent simulation studies.

Table 6.3: Summary of activation energy parameters used for simulations of 8YSZ

	Sintering experiment	Sintering atmosphere	Activation energy [kJ/mol]
Densification	CS	air	691 ± 20
	FS	air	424 ± 17
	UHS	argon	246 ± 1
Grain growth	CS	air	575 ± 30
	FS (anode)	air	173 ± 5
	FS (middle)	air	189 ± 12
	FS (cathode)	air	197 ± 14
	UHS	argon	405 ± 67

The table shows that the calculated activation energy Q_d for CS in air is 691 ± 20 kJ/mol, which is consistent with the literature values of 688–757 kJ/mol for 8YSZ [179–181]. In comparison, FS has a much lower activation energy of 424 ± 17 kJ/mol. The ability of FS to reduce the activation energy for densification was also reported on other materials like uranium dioxide (UO_2), where Q_d was decreased from 380 kJ/mol to 108 kJ/mol [182].

Moreover, the activation energy for densification of 8YSZ during UHS is 246 ± 1 kJ/mol, which is considerably lower than those of the CS and the FS conducted in air. Since UHS experiments were performed in argon, a direct comparison is challenging considering the effect of sintering atmosphere. However, our experimental results reveal that, at the same temperature, 8YSZ samples were more densified in air than in argon. This indicates that the activation energy for CS in argon is likely higher than 691 kJ/mol. Consequently, it can be concluded that UHS also substantially reduces the apparent activation energy for densification of 8YSZ. This observation is consistent with other studies on UHS [3,183].

Reductions in apparent activation energy for sintering have also been observed in other sintering techniques with high heating rates, such as FAST/SPS [182,184] and microwave sintering [48]. Although different sintering methods use different sintering aids (pressure, electric field, electromagnetic field, etc.), their common feature—ultra-high heating rate—appears to be the key factor in altering the fundamental mass transport mechanism during sintering. High heating rates reduce the activation energy by suppressing surface diffusion, which is known to increase the apparent activation energy for densification [185]. By rapidly transitioning through lower temperature ranges, where surface diffusion and neck growth dominate without contributing to densification [72], high heating rates directly activate grain boundary diffusion and volume diffusion, thereby enhancing densification during sintering.

From **Table 6.3**, it can also be observed that FS reduces the activation energy for grain growth Q_g compared to CS. However, unlike densification, where the activation energy for UHS is smaller than FS, the activation energy for grain growth during UHS is much larger than FS. This disparity is attributed to the influence of the electric field, which increased grain boundary mobility in FS but is absent in UHS and CS. Additionally, the activation energy for grain growth gradually increases from the anode side to the cathode side of the flash-sintered samples, indicating a grain size gradient and microstructural asymmetry on the gauge section of the dog-bone samples induced by electrical polarity.

6.2 Experiments of $SrTiO_3$

For the study of $SrTiO_3$, the investigation focused on the effect of heating rate on densification during sintering. Given this focus, only CS and UHS of $SrTiO_3$ are discussed in this section. The shrinkage curve obtained from DIL sintering is presented first, then the densification and grain growth behavior of $SrTiO_3$ during UHS are introduced. The experimental investigations on $SrTiO_3$ were conducted in the work of Mishra et al. [76]. Finally, the activation energies for grain boundary diffusion (CS) and grain growth (UHS) are analyzed using experimental data to study the sintering kinetics.

6.2.1 Sintering and microstructural characterization

The CS behavior of $SrTiO_3$ was investigated using dilatometry in an argon atmosphere to replicate the oxygen-lean atmosphere during UHS. The linear shrinkage and densification of $SrTiO_3$ as a function of temperature in argon are depicted in **Figure 6.15a**. The contribution from thermal expansion was subtracted in the figure. For UHS, the RD of samples sintered at four different current levels are shown in **Figure 6.15b**. Each current corresponds to a simulated average temperature of the sample, which are indicated on the top axis of the figure. Notably, the temperature increase in the $SrTiO_3$ sample lagged behind the applied current. After the maximum current was reached, the temperature continues to rise during the holding time. The temperatures reported here corresponds to the end of the holding time (10 s) period during UHS, indicating that the real dwell time of the sample at the corresponding sintering temperatures is 0 s.

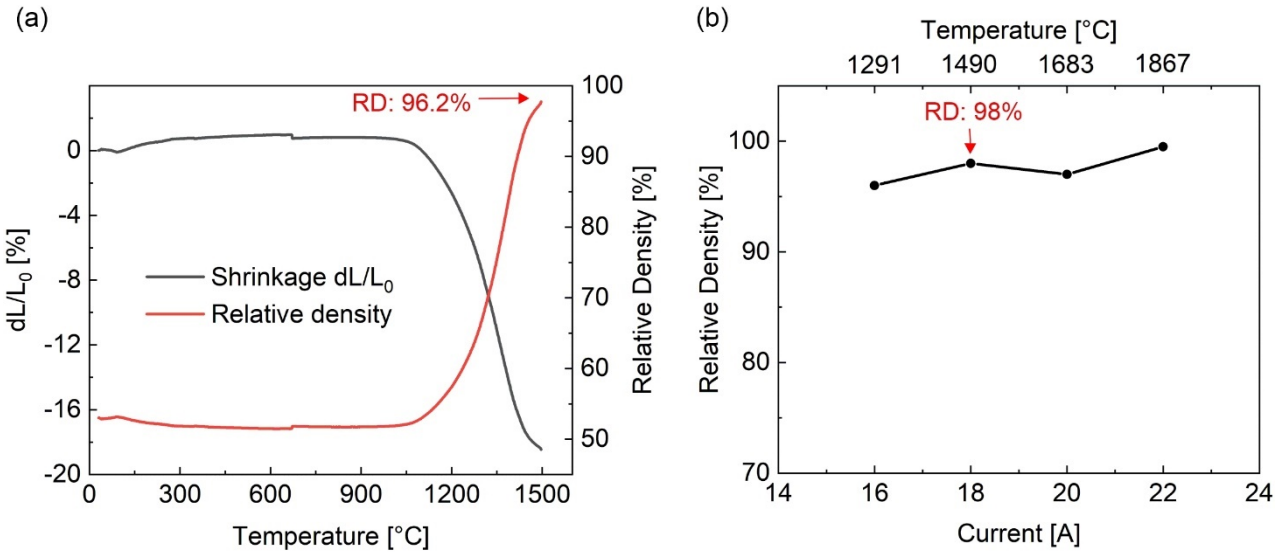

Figure 6.15: (a) Uniaxial shrinkage and densification curves from dilatometer sintering of $SrTiO_3$ at the heating rate of 25 K/min, maximum temperature of 1500° C, and 1 min holding time in argon; (b) Relative density of the UHS-sintered samples as a function of the maximum current, with a 10 s holding time at the maximum current. The top axis indicates the simulated average temperature of the samples at each current.

The dilatometry study showed that the sintered sample achieved a RD of 96.2% at 1500°C, while for UHS, a higher RD of approximately 98% was reached at the maximum current of 18 A, which corresponds to a sintering temperature of 1490°C according to the simulation. This finding demonstrates UHS's ability to significantly enhance densification even at comparable sintering temperatures to CS.

The measured average grain sizes at the maximum current of 16, 18, 20, and 22 A is shown in **Figure 6.16**. The SEM micrographs of the polished and thermally etched cross-sections of UHS-sintered pellets at different maximum currents for $SrTiO_3$ are shown in **Figure 6.17** [76]. These micrographs were taken from the middle section of the samples and illustrate the microstructural evolution during UHS.

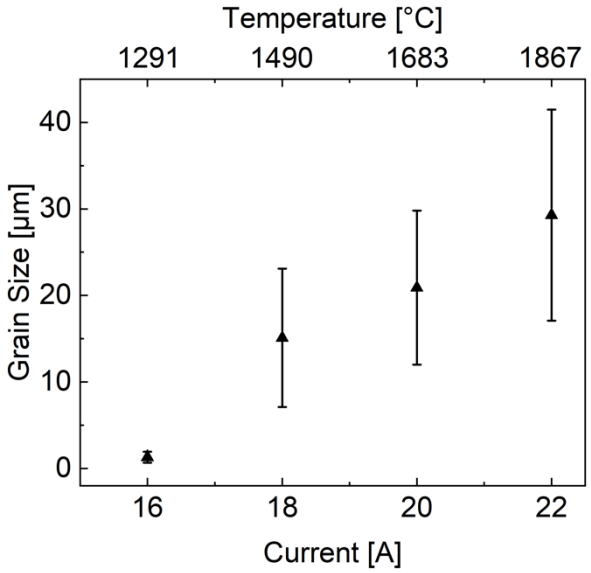

Figure 6.16: Grain sizes of UHS-sintered $SrTiO_3$ samples at different maximum currents. The top axis indicates the simulated average temperature of the samples at each current.

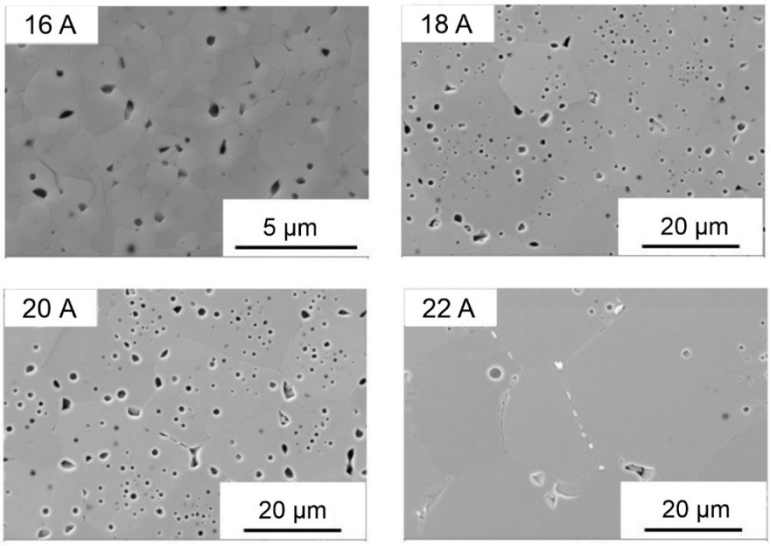

Figure 6.17: SEM micrographs of UHS-sintered $SrTiO_3$ samples at different maximum currents [76].

The figures show that the average grain size of $SrTiO_3$ increases rapidly with increasing current. The most notable difference in the microstructures occurs between the maximum current of 16 A and 18 A. At 16 A, the UHS-sintered sample showed limited grain growth, with porosity remaining inter-granular. In contrast, at 18 A, the UHS-sintered sample underwent rapid grain growth, with most pores becoming entrapped within the grains. While the RD increased by only 2% from 16 A to 18 A, the average grain size grew more than tenfold. Grain growth continued as the current increased to 20 A and 22 A.

The rapid grain growth over such a short time suggests that the grain boundary migration rate became extremely high above 18 A. The observed pore entrapment inside individual grains in $SrTiO_3$ samples is characteristic of exaggerated grain growth [5]. This indicates that the microstructure transitioned to a state of pore-grain boundary separation, following the mechanism of pore drag [186,187]. In the pore drag model, pores often separate from the grain boundaries and become trapped within rapidly growing grains when the grain boundary migration rate exceeds the pore diffusion rate, and the pore drag force is insufficient to impede grain boundary migration [188].

To restrict grain growth, $SrTiO_3$ has been doped with 2 mol% iron (Fe), and significantly improved grain sizes were observed after UHS [76]. This improvement is due to the suppression of pore-grain boundary separation caused by the reduction of grain growth rates from Fe doping [189,190]. As Fe segregates to grain boundaries, the solute drag effect, caused by the slow diffusion of Fe along the moving boundary, hinders grain boundary movement and significantly reduces grain growth kinetics, enabling the tailoring of microstructures during UHS.

6.2.2 Densification kinetics

Similar to the parameter identification process for 8YSZ, the strain rate formulation used for CS of $SrTiO_3$ is rewritten as Equation 6.7. To determine the activation energy for grain boundary diffusion Q_b, and assuming a constant grain size G, the equation is reformulated in logarithmic form, as shown in Equation 6.8, where K_4 is a constant.

$$\dot{\varepsilon}_z = -\frac{\dot{\rho}}{\rho} = -\frac{3\gamma(1-\rho)}{2AT\rho \exp\left(\frac{Q_b}{RT}\right) G^4} \tag{6.7}$$

$$ln\left[T \cdot \frac{\dot{\rho}}{(1-\rho)}\right] = -\frac{Q_b}{RT} + K_4 \tag{6.8}$$

The experimental data from the densification curve were selected based on the criterion of RD < 95%, ensuring minimal grain size changes. The left-hand side of Equation 6.8 against

$-1/T$ is plotted as in **Figure 6.18**. From the slopes of the curves, the average activation energy for grain boundary diffusion can be obtained as 243 kJ/mol, which aligns well with the reported literature on $SrTiO_3$ [191,192]. In this study, it is assumed that under the same temperature range and similar sintering atmosphere, the activation energy for grain boundary diffusion Q_b is an intrinsic, material-specific property. For a given material with the same composition, microstructure, and initial density, this activation energy remains consistent across different experimental methods. Accordingly, the same value of Q_b was adopted for the simulation of UHS of $SrTiO_3$.

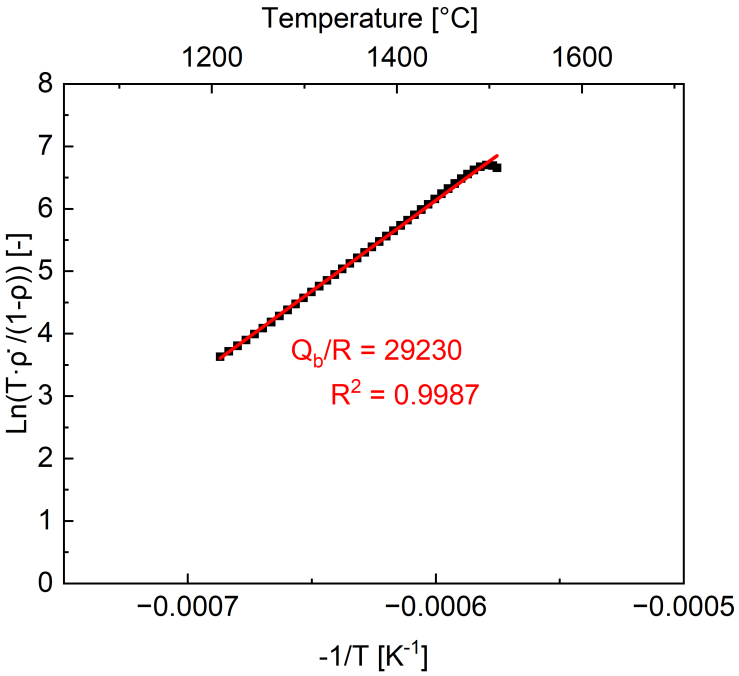

Figure 6.18: Parameter identification for densification: Determination of parameter Q_b for CS of $SrTiO_3$.

6.2.3 Grain growth kinetics

For UHS of $SrTiO_3$, considering that prominent grain growth only started after 16 A, the grain sizes at 18 A, 20 A, and 22 A are used to construct linear regression plot based on Equation 6.6. The result is shown in **Figure 6.19**. A strong linear correlation was obtained from the grain size data, and the activation energy for grain growth Q_g during UHS was determined to be 117 kJ/mol. This small value of activation energy indicates a very high grain boundary migration rate in the high temperature range (1500–1900°C). As discussed in section 6.2.1, the high temperatures reached during UHS resulted in grain boundary migration rates high enough for pore separation to occur. This determined activation energy was used for the modeling of UHS.

For modeling of CS, which involves relatively lower sintering temperatures (up to 1500°C), an activation energy for grain growth of 837 kJ/mol was adopted from the literature on

$SrTiO_3$ [141]. The large difference in activation energies indicates a change in the rate-controlling mechanism. Under UHS, the unique condition and very high temperatures enhance grain boundary mobility and favor pore–boundary separation, yielding a much lower apparent Q_g than in CS.

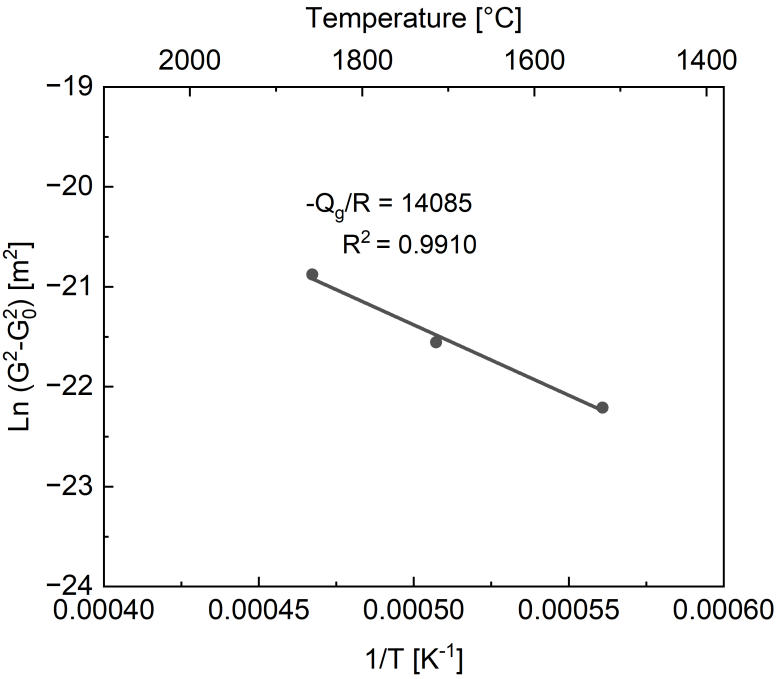

Figure 6.19: Parameter identification for grain growth: Determination of parameter Q_g for UHS of $SrTiO_3$.

6.2.4 Interim summary

The activation energy parameters determined in this section, which were used for simulations of $SrTiO_3$, are summarized in **Table 6.4**. Both CS and UHS experiments were conducted in oxygen-lean atmospheres. It is important to note that, unlike the apparent activation energy for densification Q_d used in the study of 8YSZ, the activation energy for grain boundary diffusion Q_b is applied here. This value is assumed to remain consistent for both CS and UHS to isolate the effect of ultra-heating rate on pore structure in the modeling. Q_b is considered dependent only on the material.

Table 6.4: Summary of activation energy parameters used for simulations of $SrTiO_3$

	Sintering experiment	Sintering atmosphere	Activation energy [kJ/mol]
Densification	CS	argon	243
	UHS	vacuum	243
Grain growth	CS	argon	837
	UHS	vacuum	117

Table 6.5 compares the densification behavior of CS and UHS for $SrTiO_3$. The same conclusion to the study on 8YSZ can be drawn from the table: UHS achieves higher densification at comparable sintering temperatures with shorter dwell times than CS. This improvement is attributed to the significantly higher heating rate of UHS (8940 K/min) compared to CS (25 K/min). Notably, the heating rate of UHS for $SrTiO_3$ is found to be higher than that of 8YSZ, primarily due to the considerably better thermal conductivity of $SrTiO_3$ samples compared to 8YSZ.

Table 6.5: Comparison of CS and UHS of $SrTiO_3$ at similar sintering temperatures

	Temperature [°C]	Dwell time [s]	Heating rate [K/min]	RD [%]
CS	1500	60	25	96.2
UHS	1490	0	8940	98.0

The results from the $SrTiO_3$ study further confirm the role of heating rate in enhancing densification, as proposed in the 8YSZ study. It can be confidently stated that, even without the influence of electric field-induced current flow in the sample, ceramic materials can still be fully sintered at an unprecedented rate when the heating rate is sufficiently high. However, the rapid process does not inhibit the prominent grain growth of $SrTiO_3$, particularly at very high temperatures. To obtain fully dense $SrTiO_3$ samples with a fine microstructure, doping is necessary to impede grain boundary migration during grain growth.

Our work on both 8YSZ and $SrTiO_3$ identified the ultra-high heating rate as the dominant factor driving rapid sintering during FS and UHS, rather than the non-thermal influence of the electric field. This finding aligns with the recent work of Raj et al. [193], which showed that heating alone, without the application of an electric field, can also induce the flash phenomenon. They attributed this observation to phonon-induced Frenkel defect formation through molecular dynamics (MD) calculations. However, the mechanistic links between phonon-induced Frenkels and high electronic conductivity in oxides remain unclear. In our study, the effect of the high heating rate on rapid densification was attributed to delayed surface diffusion, which alters the pore shape evolution trajectory during sintering. This hypothesis was investigated through modeling work on $SrTiO_3$, which will be introduced in section 7.2.2.

7 Numerical results

7.1 Simulations of 8YSZ

In this section, the simulation results of 8YSZ are presented. The study starts with FS, where the onset temperatures of FS under different electric fields are predicted. With a good match between the simulation and experimental data, the validity of the thermal-electrical model is confirmed. Following this, the temperature distribution within the sample during FS is shown, along with predictions of densification and grain growth. For comparison, the simulation results of CS are also provided.

For UHS, the predicted temperatures on the surface and inside the carbon felt are compared with experimental measurements to evaluate the accuracy of the simulation. Subsequently, the temperature distribution within the setup and the sample is presented. In the last section, the simulation results of densification and grain growth during UHS are introduced.

7.1.1 Onset temperature of FS

The onset temperature of FS, signaled by a non-linear rise in electrical conductivity and a surge in power dissipation, has been found to be inversely related to the applied electric field [86,194]. As described in section 5.3.1, the convection coefficient in the finite element model was calibrated by matching the simulated flash-onset temperature to literature data obtained under constant heating rate flash conditions [68]. In the simulation, a wide range of electric field (from 100 V/cm to 4000 V/cm) was applied. The temperature profiles of the gauge sections of the dog-bone samples were extracted and averaged after each simulation. By plotting the temperature-time evolution curves, the flash-onset temperature can be identified as the point where the abrupt increase in temperature occurs. Simulation results show that the onset temperature decreases with increasing electric field.

By fitting the results with experimental data, the parameter of convection coefficient was calibrated to be 34 W/(m²·K). The relationship between the onset temperature and electric field is plotted in **Figure 7.1** for both experiment and simulation. The figure shows a very good agreement between the numerical and experimental results. In addition, simulations with the electric fields higher than 4000 V/cm were also conducted. The results show minimal changes in the onset temperature, indicating that a lower bound of the onset temperature is already reached at 4000 V/cm. This observation further supports the hypothesis of the role of Debye temperature on the onset temperature of FS [87] by using the electric fields that are difficult to achieve experimentally.

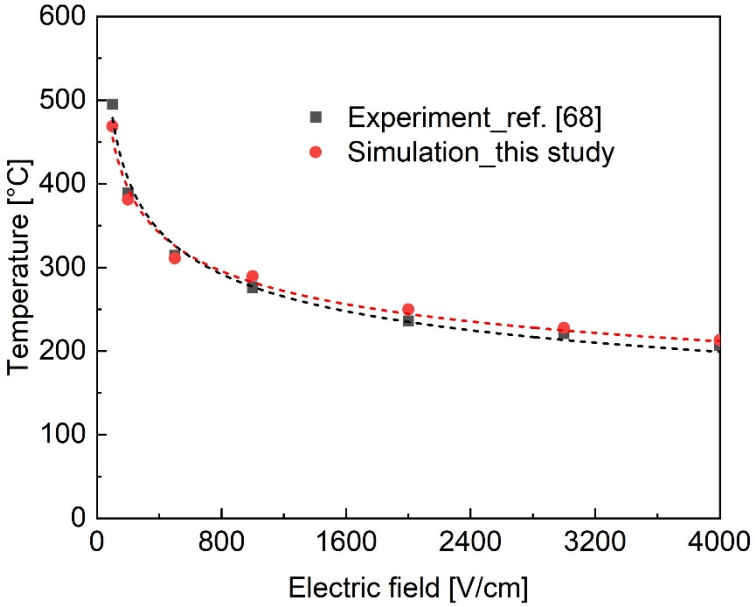

Figure 7.1: Comparison of simulation results and experimental values from ref. [68] of the flash-onset temperatures of 8YSZ with respect to different electric fields.

7.1.2 Temperature distribution of FS

To investigate the densification and grain growth during isothermal FS, the temperature distribution within the sample must be first analyzed using FEM. The temperature evolution of the sample was studied by extracting the average temperature of the gauge sections of the dog-bone samples from the simulation results. **Figure 7.2a** shows the evolution of the average temperature during FS at the current densities of 25 mA/mm², 50 mA/mm², 75 mA/mm², and 100 mA/mm², with a dwell time of 120 s. The curves reveal that it takes only a few seconds to heat the sample from the preset 850°C to the maximum temperatures after the onset of FS. The temperature then stabilizes during the current-controlled period.

Figure 7.2b illustrates the temperature distribution in the dog-bone sample flash-sintered at 100 mA/mm² for 120 s. To visualize the maximum temperature reached in the gauge section, the model was cut along the xy-symmetry plane. The highest temperature is observed at the center of the sample, and it gradually decreases outward due to thermal conduction and radiation to the surrounding environment. A temperature difference of around 150 K within the gauge section is observed for the sample flash-sintered at 100 mA/mm² with 120 s. However, the simulation results indicate that the temperature gradient decreases at lower current densities. For example, at a current density of 25 mA/mm², the temperature difference within the gauge section is reduced to around 30 K.

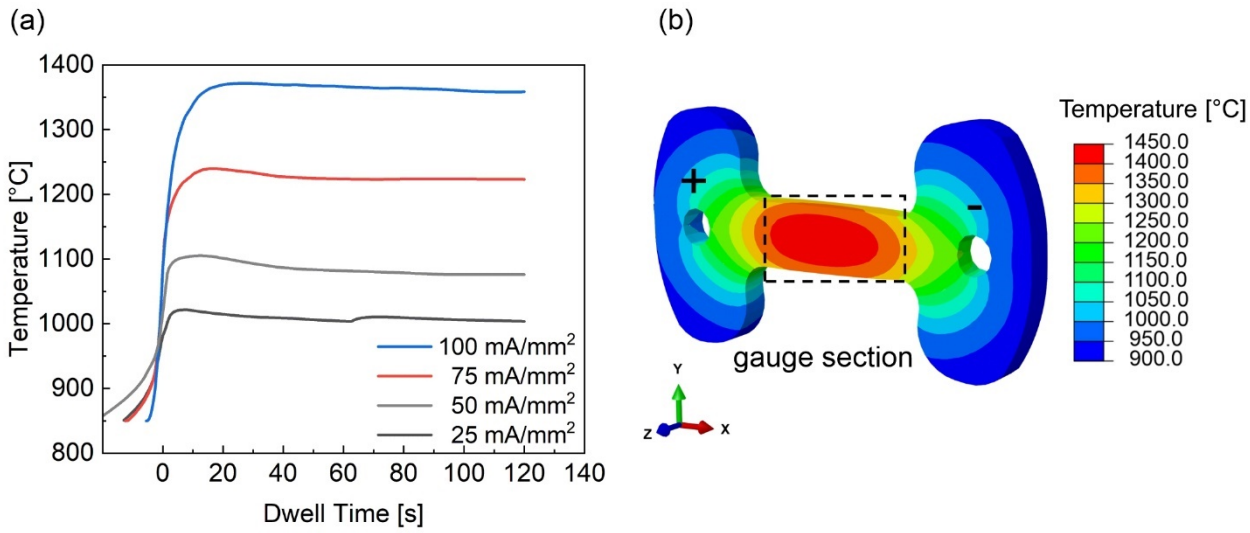

Figure 7.2: Temperature simulation during FS: (a) mean temperature evolution for 25 mA/mm², 50 mA/mm², 75 mA/mm², and 100 mA/mm² with a dwell time of 120 s; (b) temperature distribution in the dog-bone sample sintered at 100 mA/mm² for 120 s, cut along its xy-symmetry plane.

A symmetrical temperature distribution in the flash-sintered dog-bone sample is demonstrated in **Figure 7.2b**. Early studies [71,121,195] on FS of YSZ have suggested that electrochemical reduction at the cathode side might occur and reduces the electrical resistance of the material near the cathode, leading to less heat dissipation at the cathode side and potential overheating at the anode side. However, in this study, the effect of electrochemical reduction was not initially considered in the model due to the experimental challenges of measuring in-situ local conductivity within the dog-bone samples. Additionally, Biesuz et al. [71] found that for FS of 8YSZ in “good contact” mode—where Pt paste instead of Pt wire was applied to the contact surface—the reduction of the cathode was much less evident and the temperature distribution in the sample was symmetrical. In the present work, a generous amount of Pt paste was applied between the sample holes and the electrodes to minimize contact resistance. Therefore, a symmetrical temperature distribution was assumed for this study. Further discussions of the effect of electrochemical reduction on FS simulations are given in section 7.1.3.

7.1.3 Densification and grain growth of FS

Upon the predicted temperatures and obtained constitutive parameters, the densification and grain growth behavior were simulated for both FS and CS by FEM. For the implementation of grain growth model for FS, the experimentally determined activation energies and the fitted pre-exponential parameters were individually assigned to the anode, middle, and cathode regions. The identification process for these parameters was explained in section 6.1.4. Grain growth parameters for the intermediate and outermost

regions were determined using a linear interpolation method and defined in the subroutine. The simulated relative densities in the gauge sections of the dog-bone samples were extracted and averaged. Grain size results were extracted from the anode (A), middle (B), and cathode (C) regions on its xy-symmetry plane. For CS, since the temperature distribution is uniform across the sample, no specific regional considerations were necessary for the evaluation of the results. In the following, the numerical results for FS and CS were compared with the experimental data, as shown in **Figure 7.3**. In general, a good agreement between numerical and experimental data was achieved for both densification and grain growth. Relatively large deviations observed for FS can be attributed to challenges in consistently measuring density and grain size for the same gauge length/position of the dog-bone samples.

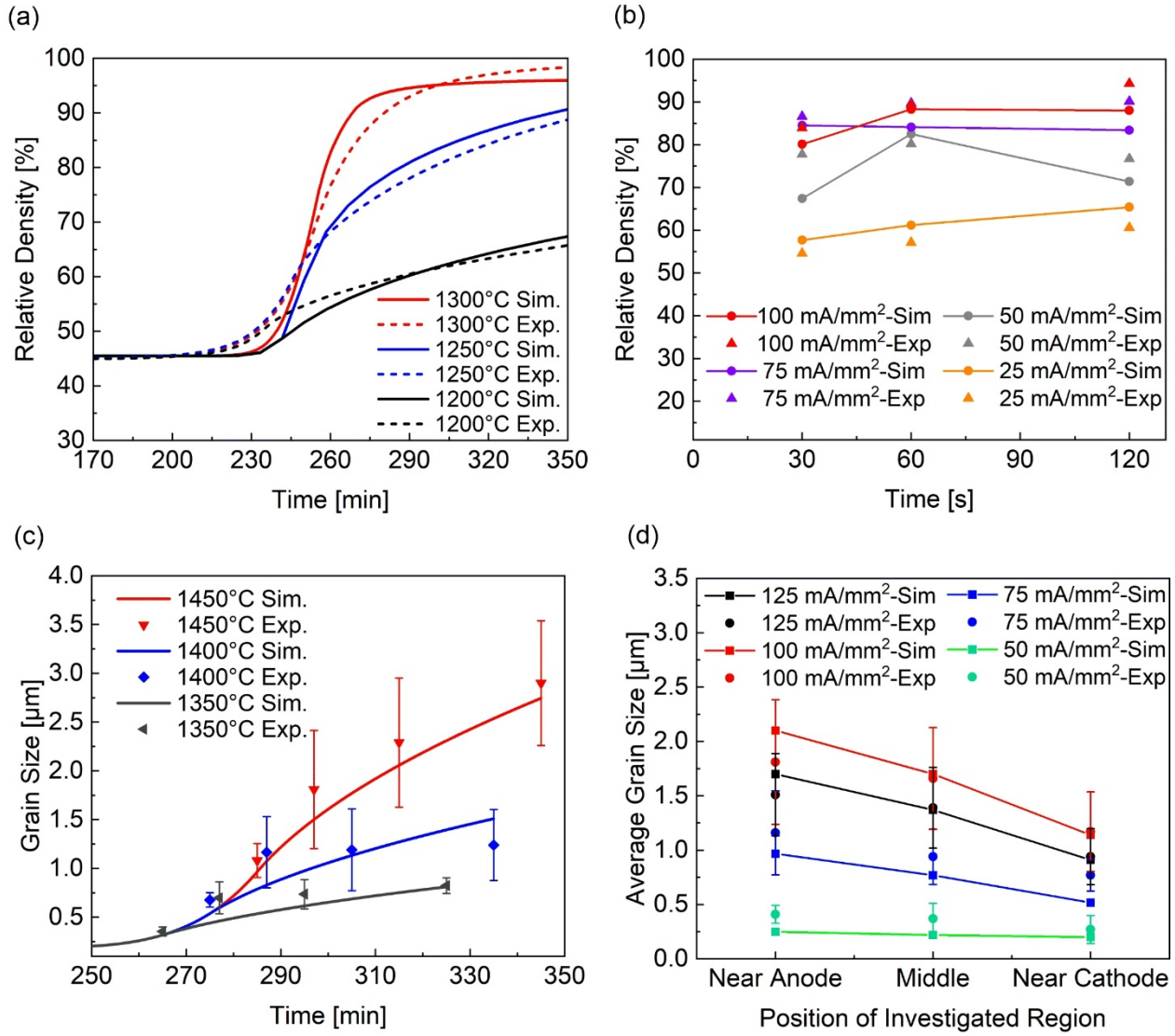

Figure 7.3: Experimental and simulation results for (a) densification of CS at 1200°C, 1250°C and 1300°C for 2 h, (b) densification of FS at 25, 50, 75, and 100 mA/mm² with dwell times of 30, 60, and 120 s, (c) grain growth of CS at 1350°C, 1400°C, and 1450°C for 0, 12, 30, and 60 min and (d) grain growth of FS at 50, 75, 100, and 125 mA/mm² for 120 s.

The simulated density and grain size distributions within the dog-bone sample flash-sintered at 100 mA/mm² for 120 s are illustrated in **Figure 7.4**. **Figure 7.4a** shows a density gradient that decreases from the cathode side (right) to the anode side (left), which appears to correlate with the microstructural asymmetry depicted in **Figure 7.4b**. Larger grain sizes at the anode side can suppress further densification and lead to a smaller density compared to the cathode side.

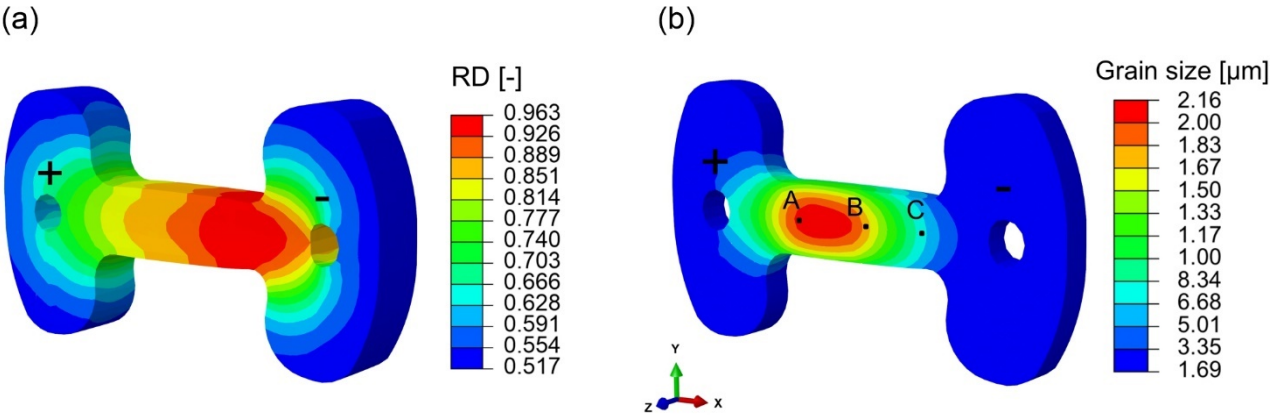

Figure 7.4: Simulation results of flash-sintered samples at 100 mA/mm² for 120 s: (a) density distribution in the entire dog-bone sample; (b) grain size distribution in the half of dog-bone sample cut along its xy-symmetry plane. Position A, B, and C indicate the locations where grain sizes were measured and analyzed, corresponding to the anode, center, and cathode, respectively.

Microstructural characterization revealed that the largest grain sizes in flash-sintered 8YSZ samples occurred on the anode side, which was also reported by Bhandari et al. [196]. However, such observation of anode-favored grain growth contrasts with some previous studies on 3YSZ and 8YSZ materials [121,195], which reported much larger grain sizes at the cathode side. Cathode-favored grain growth in these studies was attributed to the electrochemical reduction of the material at the cathode. Such reduction can lower the migration barrier for diffusion and at the same time increase the grain boundary mobility [121,195]. However, electrochemical reduction has also been suggested to induce higher temperatures at the anode side, which explains the faster grain growth at the anode side of 8YSZ in the work of Bhandari et al. [196]. Another case of abnormal grain growth at the anode was observed in ZnO by Zhang et al. [61]. In their work, the microstructural asymmetry was attributed to the formation of cation vacancies at the anode due to the local accumulation of free electrons. The increase of cation vacancies could lead to a decrease of activation energy for grain growth.

The contrasting findings of microstructural asymmetry during FS imply that for different materials and sintering processes (e.g., current density and holding time), FS may induce different grain growth enhancement mechanisms. In this study, the theory of the

accumulation of defects at the anode is adopted to account for the abnormal grain growth near the anode of the dog-bone sample. Activation energies for grain growth were calculated separately for the anode, center, and cathode regions. The results show a decrease in activation energy from the cathode (197 ± 14 kJ/mol) to the anode (173 ± 5 kJ/mol), which corresponds to a higher grain boundary mobility and a larger grain size at the anode. The simulation results align with the experimental observation of a decrease in grain size from the anode to the cathode side (**Figure 7.4b**), while the local density shows an inverse gradient (**Figure 7.4a**).

However, considering the possible electrochemical reduction near the cathode side starting before the onset of flash, the simulated density distribution may not fully represent the real sample. Partial chemical reduction at the cathode can lead to the decrease of electrical resistance, thus, less Joule heating and less densification near the cathode side. To study the influence of electrochemical reduction on the local density, a case study was conducted by assigning a lower electrical resistivity to the cathode region (marked with black square in **Figure 7.5**) in the model. **Figure 7.5** shows the simulation results obtained by decreasing the electrical resistivity of 50% at the cathode region for the entire flash process. By comparing **Figure 7.4** and **Figure 7.5**, it can be concluded that partial reduction near the cathode side produces a more symmetrical density distribution, whereas the grain size distribution remains largely unaffected.

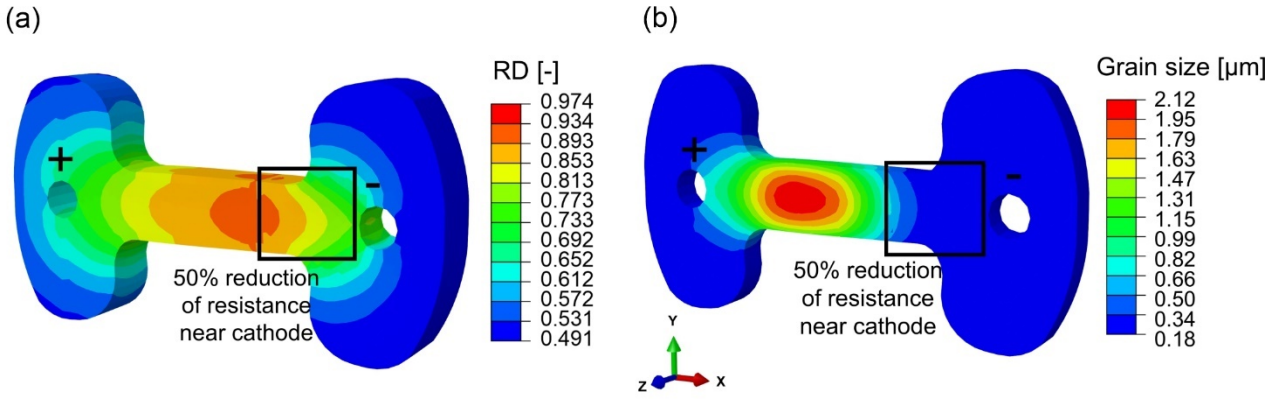

Figure 7.5: Simulation results of a flash-sintered sample at 100 mA/mm² for 120 s with the partial reduction of the electrical resistivity near the cathode side: (a) density distribution in the entire dog bone sample and (b) grain size distribution in the half of dog-bone sample cut along its xy-symmetry plane.

7.1.4 Temperature distribution of UHS

The simulation results for the temperature distribution in the UHS setup at 13 A for 30 s are shown in **Figure 7.6a**. The cross-section of the carbon felt reveals a large temperature gradient from the surface to the core of the felt, while the gradient along the current path between the two electrodes is small. Additionally, the stabilized temperatures at different

currents are demonstrated in **Figure 7.6b**, where blue dots and blue triangles indicate the temperature on the top surface of the carbon felt obtained from the simulations and the experiments, respectively, while red dots are the simulated sample temperatures averaged over the whole pellet. It can be seen that the simulated surface temperatures match closely with the temperatures measured by the pyrometer. However, the sample temperatures are significantly higher than the surface temperatures of the carbon felt. The predicted temperature distribution within the 8YSZ samples reveals a very large temperature gradient, with temperature differences ranging from 100 K to 200 K depending on the applied current.

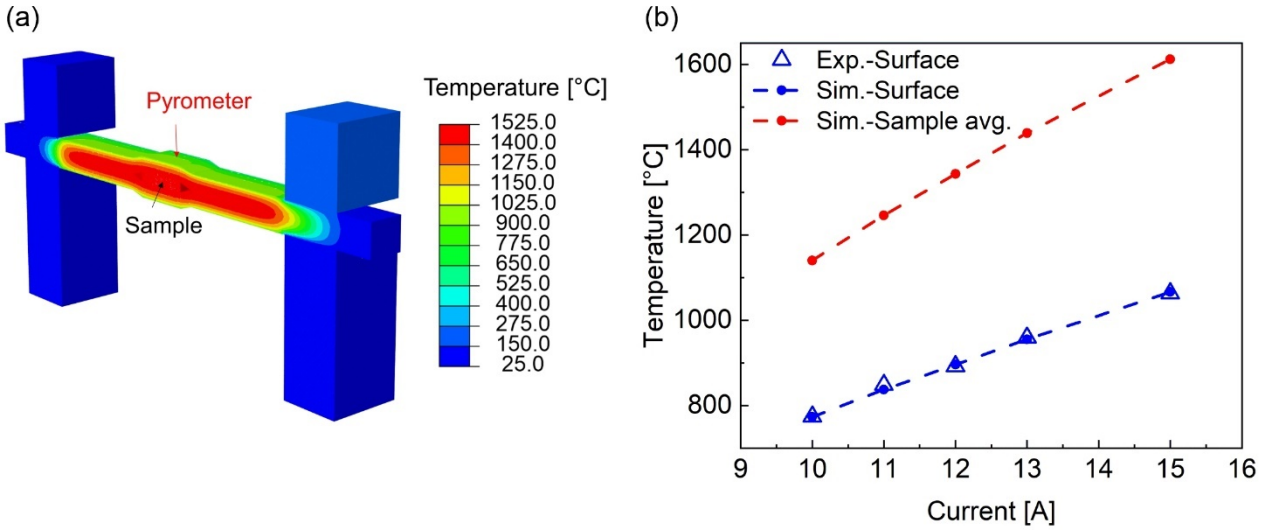

Figure 7.6: (a) Simulated temperature distribution in the UHS setup at the maximum current of 13 A for 30 s, cut along the length of the carbon felt at the half-width position; and (b) experimental and simulation results of the stabilized temperatures on the surface of the carbon felt and those of the sample at different maximum currents.

Although real-time measurement of the sample temperature is constrained by experimental limitations, efforts have been made to validate the temperature simulation inside the carbon felt (close to the sample) using a thermal couple and alloy wires. Additionally, the simulation of the temperature distribution within the sample was validated through observations of partial melting in the sintered sample, for which $SrTiO_3$ was used due to its relatively low melting point. Both validation methods are elaborated in detail in section 7.2.1.

7.1.5 Densification and grain growth of UHS

Densification of UHS

The modeling parameters were determined by the linear regression plots, as described in sections 6.1.3 and 6.1.4. The activation energies for densification Q_d and grain growth Q_g were calculated to be 246 kJ/mol and 405 kJ/mol, respectively. With the determined model

parameters, the densification during UHS was simulated using FEM, and comparisons between numerical and experimental results are summarized in **Table 7.1**.

Table 7.1: Comparison of simulation and experimental results of densification for UHS-sintered 8YSZ samples

Current [A]	Relative density [%]					
	60 s		90 s		120 s	
	Exp.	Sim.	Exp.	Sim.	Exp.	Sim.
10	55.3	50.4	58.6	58.0	60.5	65.5
11	72.0	60.4	74.6	75.7	85.0	86.0
12	89.1	75.8	91.8	89.6	95.0	96.4
13	96.6	85.3	96.0	95.7	98.6	99.6

The table shows a good agreement between the numerical and experimental results for UHS-sintered samples with long dwell times (> 60 s), whereas at the dwell time of 60 s, an underestimation by the simulation was observed. The deviation at short dwell times could be attributed to the inaccuracy of the simulated heat-up time. The heat-up time represents the time needed for the 8YSZ sample to reach its highest temperature and stabilize. Unlike the carbon felt, which peaks in temperature within 3 s, the 8YSZ sample generally takes 30–40 s to reach its highest temperature, as based on the simulation results. However, the temperature simulation was first carried out without considering the shrinkage of the sample, which could lead to an imprecise prediction of temperature evolution before the maximum temperature is reached. In reality, the sample may already reach the highest temperature earlier than the simulated peak time, meaning the real heat-up time is shorter than the predicted value. As a result, the real densities of the samples with short dwell times are higher than those predicted by the simulation. As dwell time increases, the impact of this model deficiency diminishes, as the stabilized highest temperatures were more accurately predicted.

Figure 7.7 shows UHS-sintered samples at 11 A for 120 s and 13 A for 120 s, alongside their simulated density and temperature distributions. The blackened sample surface after UHS is caused by carbothermal reduction [101,183]. With higher current levels, blackening becomes more evident. However, this only occurs on the surface and can be easily removed by grinding. Moreover, after sintering at 11 A, the sample's diameter along the x-axis (aligned with the current direction in the felt) is smaller than that along the z-axis. This irregular shape is due to density and temperature inhomogeneity within the sample, as illustrated in the simulation results shown in **Figure 7.7**. The density and temperature along the diameter aligned with the z-axis are smaller than those aligned with the x-axis.

Consequently, the shrinkage along the diameter aligned with the z-axis is smaller than that aligned with the x-axis.

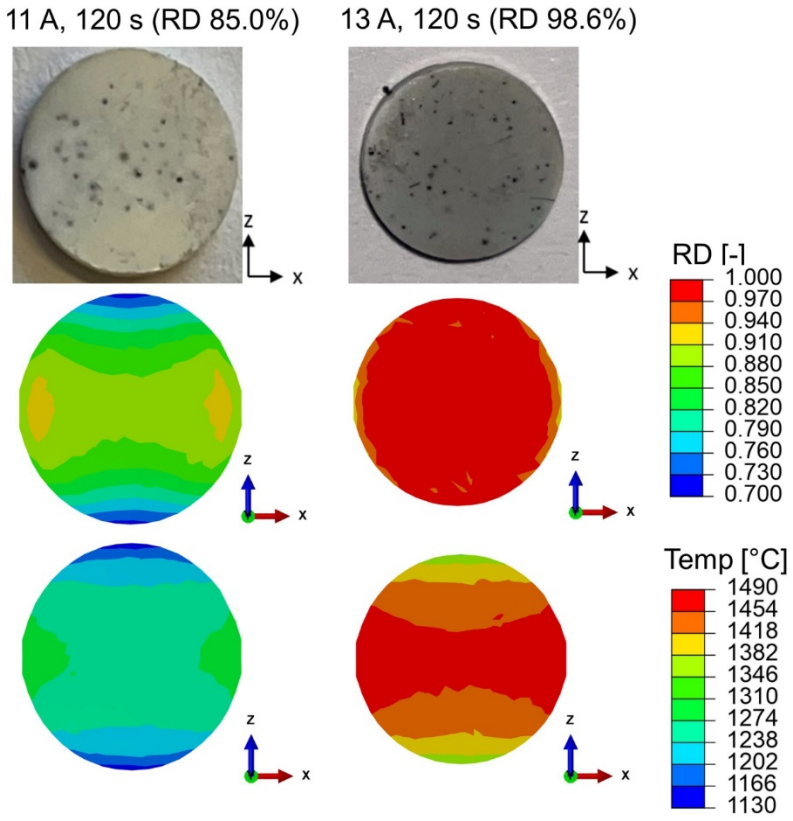

Figure 7.7: Optical image (top), simulation of RD distribution (middle), and simulation of temperature distribution (bottom) for UHS-sintered 8YSZ samples at 11 A for 120 s (left) and 13 A for 120 s (right).

This density gradient in the sample decreases with increasing applied current during UHS. As can be seen in **Figure 7.7**, the density gradient in the sample of 13 A is significantly smaller than that of 11 A. However, the temperature gradient remains distinct even at high maximum currents. The temperature inhomogeneity is induced by rapid heat dissipation to the environment through conduction and radiation, and it can be mitigated with thermal insulation [55]. Simulation results indicate that the most significant heat dissipation occurs at the ends of the pellet sample near the carbon felt's opening. Hence, the temperature gradient can be reduced by increasing the width of the carbon felt. The downside of a wider carbon felt is that the current density decreases proportionally.

In future works, FEM modeling can be utilized to guide experimental setup modifications in two main ways to achieve more uniform sample temperatures and densities: on the one hand, the widths and shapes of both the carbon felt and the sample can be adjusted to identify an optimal criterion, such as a critical ratio of sample width to carbon felt width, that allows densification at an affordable energy expense with the minimum temperature

gradient. On the other hand, the current profile can be modified in the model (e.g., using a stepwise mode) to enable a gradual temperature increment, which can also decrease the temperature gradient within the sample. This numerical strategy holds significant potential for minimizing thermal stress in the sample, and thus preventing cracking when scaling up the sample size.

Grain growth of UHS

Figure 7.8a compares the experimental and numerical results for grain size evolution with respect to dwell time at different maximum currents. A good agreement between experimental and numerical values is achieved for longer dwell times (> 60 s), while at a dwell time of 30 s, the simulation results underestimate the real grain sizes. This discrepancy aligns with the simulation results for densification and can be attributed to the imprecise prediction of the heat-up time during UHS.

Figure 7.8b demonstrates the grain size distribution in a sample sintered by UHS at 12 A for 120 s. This grain size inhomogeneity is caused by the temperature gradient in the pellet-shaped sample. To verify the simulated grain size gradient, three locations on the cross section of half of the experimentally produced pellet sample, marked as x, y, and z in the graph, were observed by SEM. The grain sizes of these three positions were measured and compared to the simulation results, as shown in the inset table of **Figure 7.8b**. The results indicate that the center of the cross section (position y) has the largest grain size, while the grain sizes at the two sides (x and z) are smaller than the center and similar to each other. This symmetrical grain size distribution was accurately predicted by simulation.

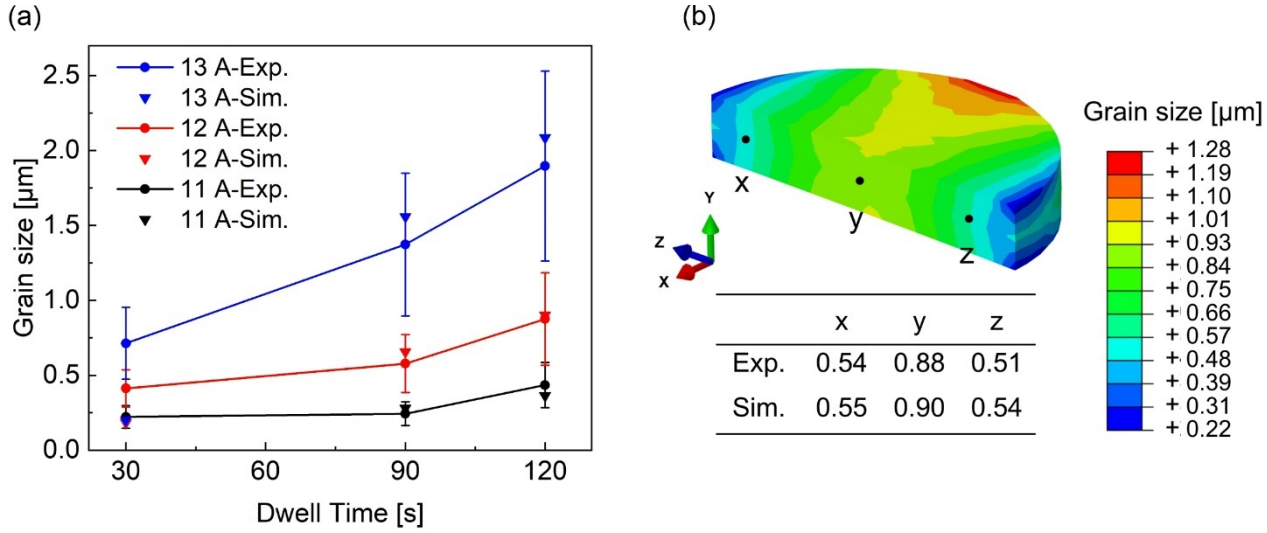

Figure 7.8: (a) Comparison of simulation and experimental results of grain sizes of UHS-sintered 8YSZ samples at 11 A, 12 A, and 13 A. (b) Simulation result of grain size distribution in the UHS-sintered 8YSZ sample at 12 A for 120 s and the comparison between experimental and simulation results of the grain size at the position x, y, and z.

7.1.6 Interim summary

A multiphysics FEM model has been developed in this study to simulate heat generation, heat dissipation, densification, and grain growth of the 8YSZ samples across three sintering methods: CS, FS, and UHS. These simulation works provide valuable insights into the underlying sintering mechanisms. The prediction of onset temperatures of FS confirms the hypothesis regarding the role of Debye temperature in the flash onset temperature. With the employed activation energy values obtained from kinetic analysis, the densification model, coupled with the grain growth law, successfully predicted relative densities and grain sizes. Some deviations between simulated and experimental data were observed, particularly for densification during UHS at shorter dwell times. However, in general, a very good match was achieved across different sintering experiments, indicating the validity of the calculated modeling parameters.

Additionally, the effect of electric field on the microstructure was considered in the model for FS, and the anisotropic grain growth across the gauge section of flash-sintered dog bone samples was successfully simulated. Furthermore, the influence of electrochemical reduction during FS was studied by assigning the cathode region a smaller electrical resistivity, resulting in a more symmetrical density gradient compared to the model without consideration of electrochemical reduction.

Although the developed model for 8YSZ demonstrates the ability to simulate accelerated densification during FS and UHS and captures the impact of the electric field on microstructure, it relies on a phenomenological approach employing the fitted apparent activation energies for densification. While the model reveals differences in densification kinetics across various sintering methods, it does not explicitly incorporate the non-equilibrium effects induced by ultrafast heating. As a result, the simulation does not fully explain the specific underlying mechanisms driving FS and UHS at ultra-high heating rates. This aspect is further investigated in the subsequent modeling and simulation of $SrTiO_3$, which is introduced in the next section.

7.2 Simulations of $SrTiO_3$

For the simulation study of $SrTiO_3$, the experimental validation methods for the simulated temperatures (on the top surface of carbon felt, inside the carbon felt, and within the sample) are introduced first. Next, the results of densification predictions for both CS and UHS using the original SOVS model are presented. Finally, a modified model, explicitly accounting for pore shape differences under normal and ultra-high heating rates, is used to simulate the densification and grain growth of $SrTiO_3$ for both CS and UHS.

7.2.1 Temperature distribution of UHS

The total duration of UHS for $SrTiO_3$ is only 10 s, during which extremely high temperatures can be reached. Accurate prediction of the sample temperature evolution during this short period is crucial for analyzing the process and the underlying mechanisms. Thus, extensive efforts have been made to validate the temperature simulation and ensure reliable conclusions.

A pyrometer was used to measure the temperature on the top surface of the carbon felt. For the inner surface, a K-type thermocouple was inserted into the empty felt at a position similar to the sample's location to measure temperatures at low currents (5 to 8 A). For UHS at higher currents (12 and 16 A), metal or alloy wires were placed inside the carbon felt. During these measurements, Al_2O_3 protection tubes were adopted to insulate the thermocouple or wires from the carbon felt. The UHS processes were stopped after 5 min to allow the recorded temperature to stabilize. At maximum currents of 12 A and 16 A, the temperature range was determined based on the melting points T_m of the nickel-chromium (90% Ni-10% Cr) wire (T_m = 1420°C) and platinum (Pt) wire (T_m = 1768°C). After the experiments, the Ni-Cr wire melted, while the Pt wire remained intact at 12 A. However, at 16 A, both wires melted. Therefore, the temperature inside the carbon felt during UHS at 12 A was estimated to be between 1420°C and 1768°C, while at 16 A, it exceeded 1768°C.

The simulation results of the temperature were extracted from the model at positions corresponding to the measurement points and compared with experimentally measured temperatures, as shown in **Figure 7.9**. In the graph, simulated values are represented by circles, while experimental values by triangles. The temperatures estimated based on the melted wires are indicated by arrows for 12 A and 16 A. The fitted temperature curves show that both the inner and top surface temperatures of the carbon felt increase with higher maximum currents.

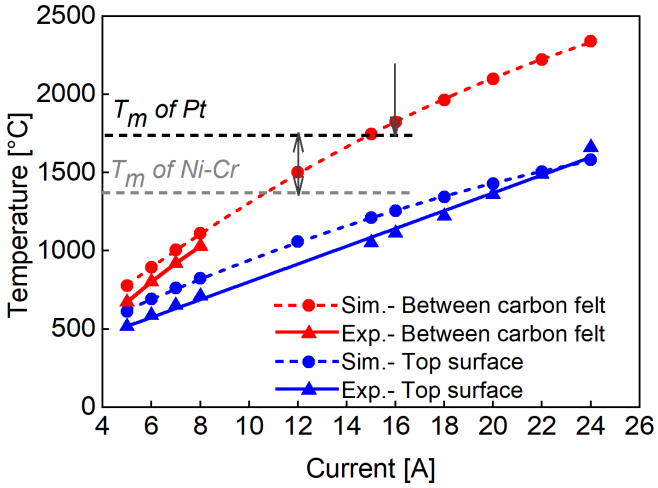

Figure 7.9: Experimental measurements and simulation results of the temperature inside the carbon felt and on the top surface of the felt during UHS at the maximum currents ranging from 5 to 24 A. At 12 A, the temperature inside the felt falls between the melting points (T_m) of Pt and Ni-Cr. At 16 A, the temperature inside the felt is higher than the T_m of Pt.

From **Figure 7.9**, an overestimation of simulated values compared to experimental measurements was observed. This discrepancy could result from inaccuracies in the thermo-physical data of the carbon felt and the precision of the pyrometer's focus. A dispersed focus can lead to an underestimation of the temperature. Despite this, the deviation is in reasonable ranges. In general, the experimentally measured temperatures align well with the predicted temperatures from FEM modeling.

In addition to analyzing the temperature distribution in the UHS setup, the temperature distribution inside the sample was also evaluated. After the experiments, samples densified at different currents exhibited different surface appearances. For samples sintered above 22 A, partial melting was observed at the center of the samples. **Figure 7.10b** presents optical images of two UHS-sintered samples: one sintered at 18 A for 10 s and the other one at 24 A for 10 s. The image clearly shows that the sample sintered at 24 A was partially melted, indicating that its temperature surpassed 2060°C, which is the melting point of $SrTiO_3$. This observation aligns with the simulated temperatures at the center of the carbon felt's inner surface, which reached approximately 2300°C at 24 A. To understand the relationship between the temperature evolution of the carbon felt and the sample, as well as the temperature distribution within the sample, systematic simulations were performed for UHS at currents between 16 A to 24 A. The results of these simulations are also presented in **Figure 7.10**.

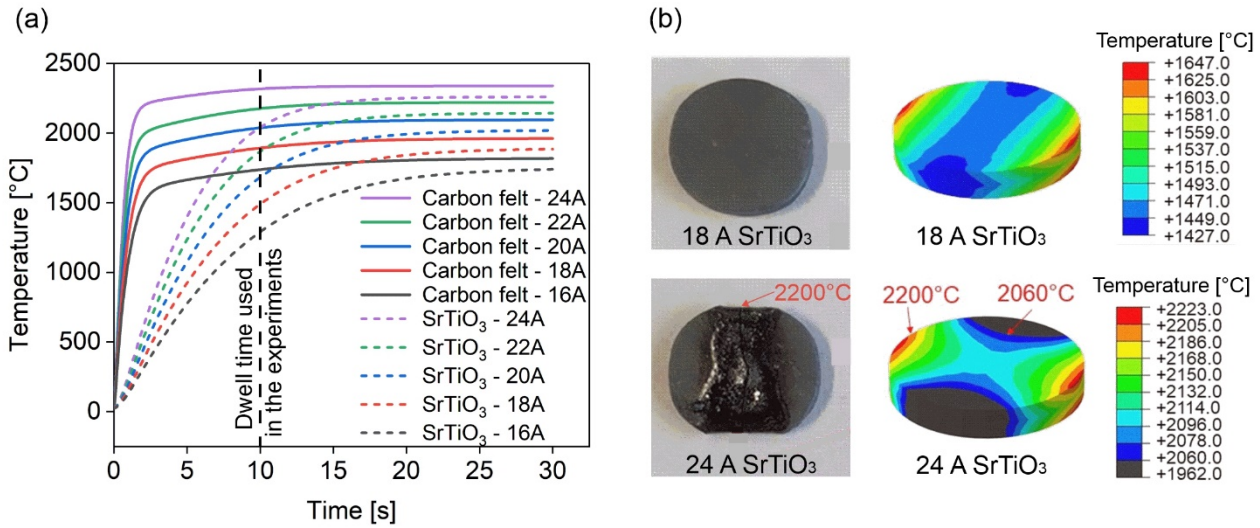

Figure 7.10: (a) Temperature evolution of the carbon felt (center of the inner surface) and $SrTiO_3$ samples (averaged over the entire pellet) during UHS at different maximum currents, as obtained from FEM simulation; and (b) comparison of optical images and simulation results for UHS-sintered $SrTiO_3$ samples at the maximum currents of 18 A and 24 A. The sample densified by UHS at 24 A has partially melted, whereas the samples densified at 18 A remains stable.

The temperature evolution of the carbon felt and $SrTiO_3$ samples during UHS at different maximum currents is depicted in **Figure 7.10a**. The temperature of the carbon felt was extracted at the center of the inner felt, while for $SrTiO_3$ samples, the temperatures were averaged over the entire pellet. It can be concluded from the graph that the temperature of the carbon felt reached its highest level within only 3 seconds, whereas $SrTiO_3$ samples required 15–20 seconds for the temperature to stabilize. The dotted black line in **Figure 7.10a** represents the dwell time set in the UHS cycles during the experiments. Its intersections with the sample temperature curves indicate that the samples reached their maximum temperature and then cooled down, sintered without a dwell time.

Figure 7.10b shows the images of the UHS-sintered samples at 18 A and 24 A. The sample sintered at 18 A reveals a slightly distorted shape compared to the original disk shape. This distortion is attributed to uneven shrinkage caused by the inhomogeneous temperature distribution within the sample, as shown in the simulated results. For the sample sintered at 24 A, partial melting at the center indicates a temperature above the melting point of $SrTiO_3$ (around 2060°C). Additionally, the top and bottom corners of the pellet completely disappeared due to over-melting. The melted regions and the disappeared area of the $SrTiO_3$ sample correspond to the area above the 2060°C and 2200°C isotherms in the simulation result. The accurate replication of the experimental observations demonstrates the model's validity in predicting temperature distribution during UHS.

7.2.2 Densification and grain growth of UHS

With the predicted sample temperatures, densification and grain growth behavior can be simulated for $SrTiO_3$. The original SOVS model was modified to incorporate the effect of the unique pore shape induced by ultra-high heating rate. The detailed modeling strategy is introduced in section 5.3.3. To examine the validity of the developed model, homogeneous constitutive modeling was initially conducted in MATLAB, assuming uniform material response throughout the sample. The constitutive equations, coupled with the grain growth law, were implemented in MATLAB to calibrate the modeling parameters using experimental data. The average sample temperatures during UHS were obtained from FEM simulations for homogeneous modeling. Finally, the developed model was implemented in ABAQUS to predict the density distribution in the samples after UHS.

Densification predicted by original constitutive model

The model parameters were determined through linear regression analysis of the DIL shrinkage data, as described in section 6.2.2. The activation energy for grain boundary diffusion Q_b was determined to be 243 kJ/mol. Employing the fitted viscosity parameters, the MATLAB model accurately predicted the densification curve derived from DIL results, as illustrated in **Figure 7.11**.

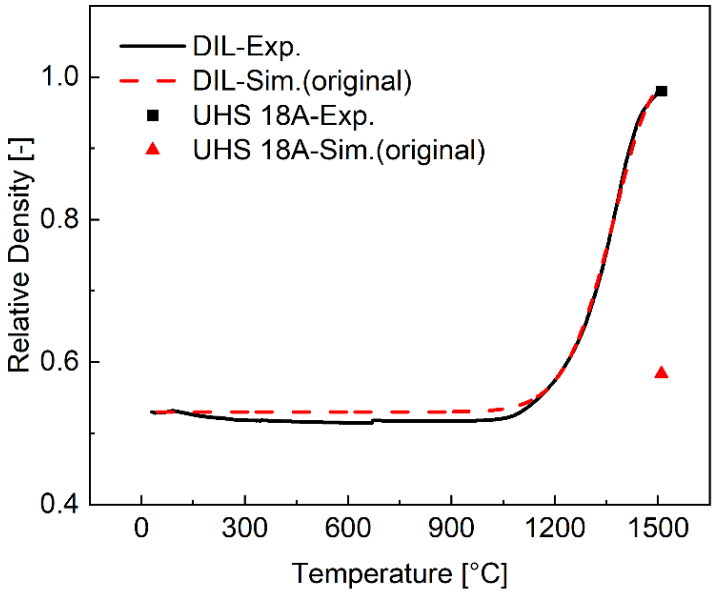

Figure 7.11: Densification of $SrTiO_3$ samples sintered by DIL and UHS at 18 A: experimental results vs. MATLAB simulation results using original SOVS model.

However, when this model with the same parameters was applied to simulate the UHS of $SrTiO_3$, the predicted RD (58%, marked with red triangle) at 18 A largely underestimated the experimental data (98%, marked with black square). The simulated maximum

temperature for UHS at 18 A is around 1490°C, which corresponds to the DIL sintering temperature. To match the experimentally obtained RD (98%), we increased the modeling temperature for UHS. It was found that a sintering temperature of 2500°C was necessary to reach this high RD when the same heating rate as UHS was applied. This high temperature surpasses the melting point of $SrTiO_3$. The unrealistic simulation results highlight the model's inability to predict the accelerated densification observed during UHS, suggesting that additional factors, potentially influential in the UHS process, need to be incorporated into the original SOVS model.

Simulation of grain growth

FEM simulation results show a longer cooling time compared to heating during UHS, as depicted by the black line in **Figure 7.12a** for 22 A. The slow cooling rate can be attributed to the low thermal conductivity of the carbon felt, which impedes heat dissipation from the sample. With the experimentally fitted activation energy for grain growth ($Q_g = 117\ \mathrm{kJ/mol}$), the grain growth behavior during UHS was predicted using MATLAB. The simulation results indicate that grains continued to grow after reaching the maximum temperature (**Figure 7.12a**), with the cooling period contributing to about one third of the total grain growth for sintering at 22 A. **Figure 7.12b** compares the experimental and simulation results of grain size after four different experiments, with the maximum currents of 16, 18, 20, and 22 A, respectively. The predicted values show a very good agreement with the experiments.

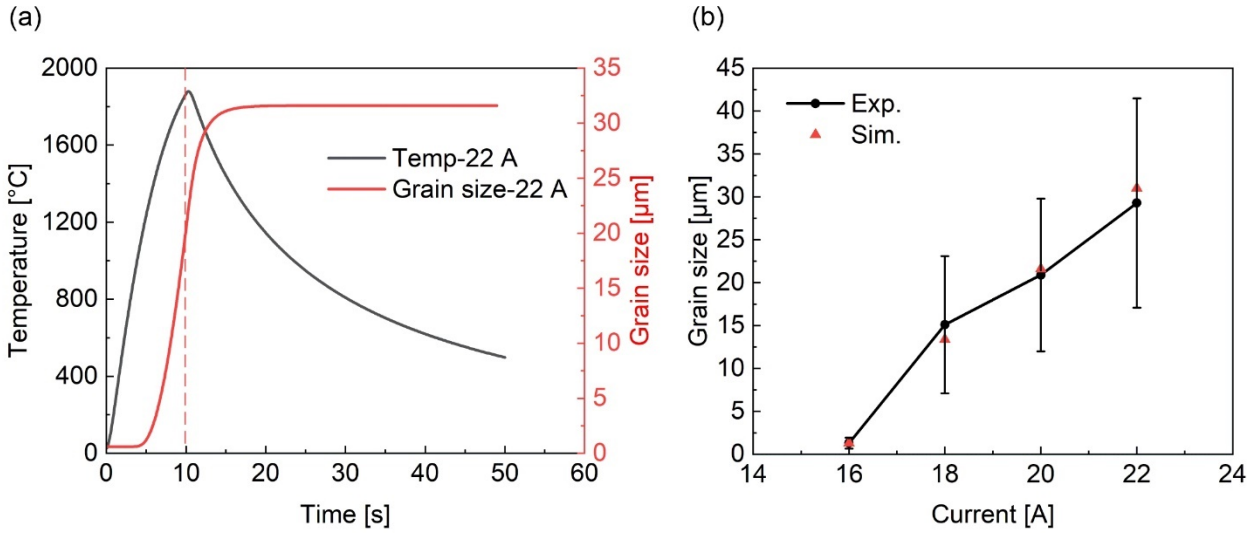

Figure 7.12: Simulation results of temperature and grain growth: (a) sample temperature evolution from FEM and grain growth calculated at 22 A; (b) comparison of experimental data and MATLAB simulation for grain sizes after the tests at maximum currents of 16, 18, 20, and 22 A.

Densification predicted by modified constitutive model

By employing the modified constitutive model coupled with the integrated grain growth equation, the densification process during UHS of $SrTiO_3$ was simulated in MATLAB. The results are illustrated in **Figure 7.13a**. For comparison, the experimental data and the simulation results of the original model have also been plotted. The figure clearly demonstrates the significant improvement in densification prediction for UHS of $SrTiO_3$ achieved by the modified model. In parallel, the densification behavior during CS was also simulated using the modified model. A strong agreement between the experimental data and model predictions is observed, as shown in **Figure 7.13b**. This confirms that the modified SOVS model proficiently characterizes the densification mechanisms operative in both CS and UHS.

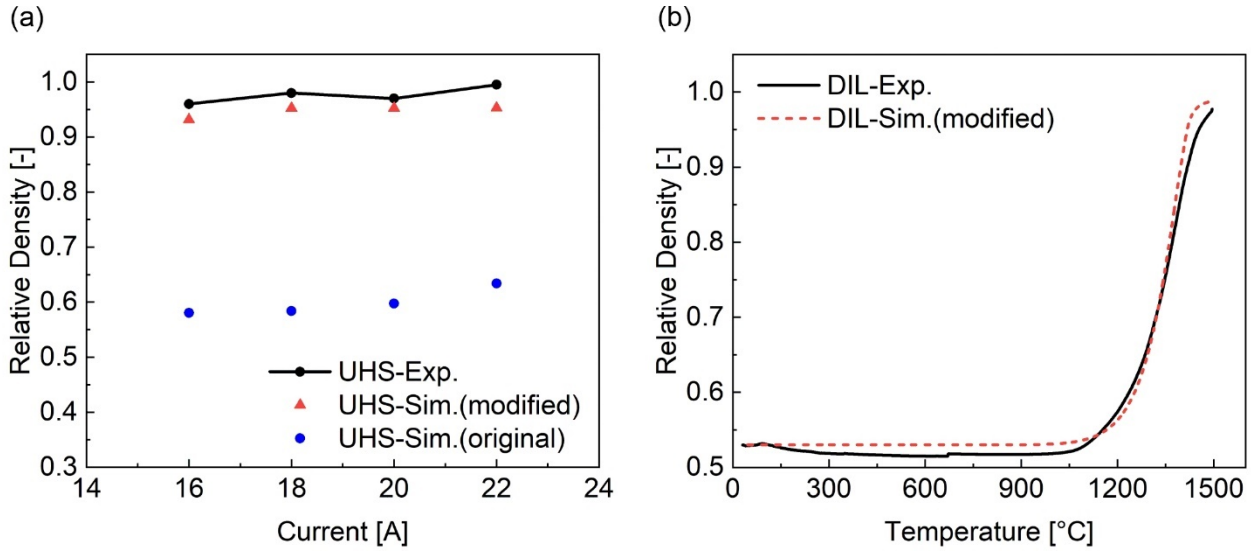

Figure 7.13: MATLAB simulation results of densification by modified SOVS model for (a) UHS and (b) CS.

Homogeneous models used the average temperature on the sample for calculations. However, given the relatively large temperature gradient on the sample during UHS, the real average density may deviate from the calculation. **Figure 7.14** presents the FEM simulation results of temperature and RD distribution. **Figure 7.14a** shows a temperature difference of ~200 K within the sample sintered at 18 A before cooling. The RD distribution after the entire UHS process is demonstrated in **Figure 7.14b**, revealing a relatively homogeneous distribution (RD ~93–95%), with small edge regions being fully densified (RD ~100%) and some areas less densified (RD <90%).

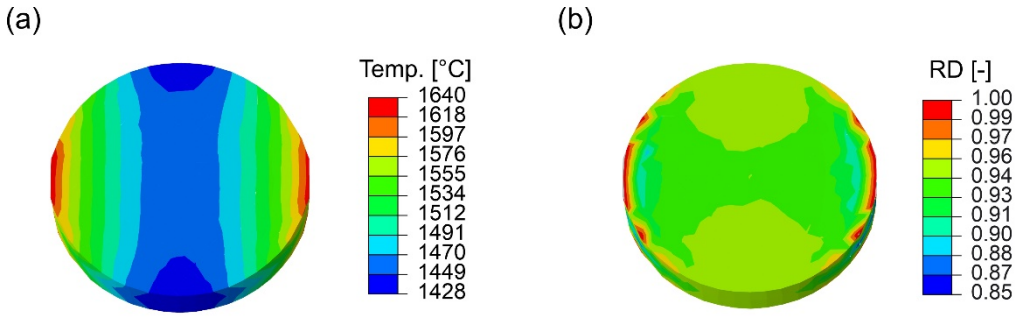

Figure 7.14: FEM simulation results using the modified SOVS model: (a) temperature distribution of UHS-sintered sample at 18 A before cooling; and (b) density distribution of the sample after UHS sintered at 18 A.

As can be observed in **Figure 7.14**, the RD gradient is smaller than temperature gradient. This difference can be attributed to the cooling period. During cooling, heat dissipates faster on the sides than at the center, causing the hotspot to shift from the side to the center of the sample while the temperature remains above 1200°C. This allows the central region of the sample to densify further, compensating for the less densification during the heating phase. The average RD of the sample after each simulation was calculated and showed only a ~1% difference compared to the homogeneous modeling results, thereby validating the accuracy of the homogeneous model.

7.2.3 Interim summary

The comprehensive experimental validation for the temperature simulation results for UHS ensures the reliability of the model. Notably, the simulated temperature distribution within the $SrTiO_3$ sample UHS-sintered at 24 A corresponds closely with the partial melting behavior observed in the experiments. This agreement demonstrates the model's capability to accurately predict the temperature of the ceramic samples during UHS.

With the extracted simulated temperatures on the sample, the densification and grain growth behavior were studied. The original SOVS model, which employs the modeling parameters obtained from conventional DIL sintering, has been shown to be inadequate in predicting the densification process of UHS. As a result, the model was modified by introducing the dihedral angle θ to account for the pore shape effect. The modified SOVS model successfully predicted densification of $SrTiO_3$ in both CS and UHS. This is achieved by adjusting θ from 180° to a defined density-dependent function, which maintains a small value during the initial and intermediate stages of sintering and gradually reaches 180° as the density approaches a critical threshold. The results support the theory that a high heating rate significantly delays surface diffusion, thereby postponing pore spheroidization and leading to a highly reactive skeleton structure, which is crucial for the densification enhancement for UHS.

Additionally, the cooling period during the UHS process was investigated, as it exceeds the heating time and may lead to continued sintering of the sample. The simulation results show that grain growth during the cooling period of UHS constitutes approximately one-third of the total grain growth, with no further densification of the sample observed during cooling.

While the modified SOVS model demonstrates capability in predicting densification for both CS and UHS, direct experimental verification of pore shape evolution during UHS remains challenging. From the SEM micrographs of flash-sintered and UHS-sintered samples in this study, no distinct star-shaped pores were observed on a large scale. This could be due to the extended cooling period after sintering and the prolonged thermal etching process at lower temperatures, which allow continued surface diffusion and pore rounding. The low thermal conductivity of the carbon felt and the sample extraction process from the setup result in a cooling period that is much longer than the heating time. Consequently, it is difficult to "freeze" the UHS microstructure for SEM observation. Future research should focus on fast-firing technologies with quenching capabilities to enable direct experimental comparisons of the pore shapes between CS and UHS.

8 Summary and outlook

8.1 Summary

This dissertation aims to investigate the densification enhancement mechanisms and microstructural evolution during electric current assisted sintering (ECAS) of oxide ceramics. The study focuses on two ECAS techniques: flash sintering (FS) and ultrafast high-temperature sintering (UHS). Through a combination of experimental investigations and numerical simulation, the study provided insights into the role of key process parameters, such as electric field, heating rate, and temperature distributions, in controlling densification and grain growth. In this work, two oxide ceramic materials, 8 mol.% yttria-stabilized zirconia (8YSZ) and strontium titanate ($SrTiO_3$), were systematically analyzed, with both materials reaching relative densities as high as 95–98% within mere 30 s under ECAS.

Three key influencing factors contributing to the enhanced densification during ECAS have been evaluated in this study: extra-high sintering temperature, ultra-high heating rate, and electric field. Both FS and UHS can achieve heating rates of up to 10^3–10^4 K/min, but the electric field plays different roles in each process. In FS, it directly heats the samples through Joule heating generated by current flow and affects defect dynamics. For UHS, it heats the carbon felt, and the sample is indirectly heated through thermal radiation and conduction from the felt. This distinction enables the evaluation of thermal and non-thermal (electrical) effects during ECAS through comparative studies.

To perform such a comparative study, extensive experimental investigations of FS and UHS of 8YSZ samples have been carried out. The relative densities and grain sizes of the samples were measured after sintering. To understand the sintering temperatures during ECAS, multiphysics FEM models have been developed to simulate the process. Moreover, to exclude the effect of sintering atmosphere, conventional sintering (CS) experiments were conducted in both air and argon. By comparing CS with the two ECAS methods under the same atmosphere and sintering temperatures, it was revealed that both FS and UHS achieve notably higher densifications within the same or shorter dwell times compared to CS. Since the heating rate and sintering time are comparable for FS and UHS, it is evident that the enhanced densification can occur without the contribution of non-thermal effects. Furthermore, the fact that rapid densification takes place at temperatures similar to or even less than those in CS demonstrates that ECAS does not rely on extra-high sintering temperature to accelerate densification. From the above analysis, the ultra-high heating

rate was identified as the dominant influencing factor driving densification enhancement during ECAS.

The heating rate affects the densification process through the interplay of different mass transport mechanisms. Rapid heating bypasses the low temperature regime, where surface diffusion dominates but does not contribute to densification, and promotes grain boundary diffusion and volume diffusion at high temperatures to facilitate densification. Without sufficient surface diffusion that redistributes mass along the pore surface to promote neck growth and pore spheroidization, the microstructure remains in a skeleton-like, point-contacted shape. It is assumed that this structure preserves the driving force for sintering and leads to enhanced densification.

Although the electric field was found not to be the dominant factor contributing to densification during ECAS of 8YSZ, its polarity effect has been observed in the microstructure of flash-sintered samples, which exhibits a gradual decrease of grain size from the anode side to the cathode side. This microstructural asymmetry can be attributed to the formation of cation vacancies at the anode due to the local accumulation of free electrons. An increase in cation vacancies could reduce the activation energy for grain growth. Moreover, electrochemical reduction at the cathode side could also result in a smaller grain size, as the reduction in electrical resistance leads to less heat dissipation at the cathode, and consequently, a lower sintering temperature. By comparing the sintering trajectories of CS, FS, and UHS, it was concluded that the electric field induces more pronounced grain coarsening in the sample compared to sintering processes without its effect.

The development of the thermal-electrical-structural FEM models involved extensive isothermal sintering experiments and material characterization techniques, which were the basis for analyzing densification and grain growth kinetics. The sintering kinetic was analyzed through linear regression plots with reasonable accuracy. The results revealed that FS and UHS substantially lower the apparent activation energy for densification of 8YSZ compared to CS. Additionally, the activation energy for grain growth was found to increase from the anode to the cathode side of the flash-sintered dog bone samples. The derived kinetic parameters were incorporated into the Skorohod-Olevsky Viscous Sintering (SOVS) model combined with a grain growth law, enabling accurate predictions of densification and grain growth for different sintering experiments of 8YSZ. The temperature simulation using the developed FEM model for FS was validated by accurately predicting onset temperatures under different electric fields. For UHS, validation was achieved using

a combination of a pyrometer, a thermocouple, alloy wires, and the sample's melting behavior.

The study on 8YSZ identified the ultra-high heating rate as the dominant influencing factor driving accelerated densification during ECAS. This result was further verified using the material $SrTiO_3$ through comparative studies of CS and UHS. The effect of high heating rate on the pore structure during sintering was explicitly incorporated into the constitutive equations to modify the SOVS model and test its validity for predicting densification in UHS. The dihedral angle parameter θ was introduced in the expressions for viscosity modulus and sintering stress within the constitutive equations to quantify pore shapes. The model employs the activation energy for grain boundary diffusion Q_b obtained from sintering kinetic analysis. The results showed that by keeping Q_b unchanged and tuning θ, the modified model accurately simulates the densification behavior of both CS and UHS. The dihedral angle θ was adjusted from 180° (CS) to a defined density-dependent function (UHS), which maintains a small value during the early stages of sintering and gradually reaches 180° as the density approaches a critical threshold. The significant improvement in the model's accuracy for predicting densification of $SrTiO_3$ in UHS supports the theory that a high heating rate delays surface diffusion, postpones pore spheroidization, and preserves a highly reactive skeleton structure, which is crucial for the densification enhancement observed in UHS.

In conclusion, this work successfully evaluated the thermal and non-thermal effects on the sintering mechanisms of oxide ceramics during FS and UHS. The ultra-high heating rate was identified as the primary factor contributing to the enhanced densification for both FS and UHS, and its effect on sintering process was integrated into the developed FEM model, which can potentially be applied to other ultra-fast firing techniques. This study contributes valuable insights into the underlying mechanisms of ECAS, paving the way for industrial upscaling and achieving homogeneous densification and microstructure in ceramic materials.

8.2 Outlook

The scope of this dissertation includes the investigation of temperature distribution, densification, and grain growth during FS and UHS. However, several aspects at the microscopic scale remain to be further explored to achieve a deeper and more comprehensive understanding of the underlying processes:

1. The electrochemical reduction during FS was considered in the developed model through a case study. However, achieving more reliable predictions of the electrical

polarity-induced gradients in samples requires a more accurate representation in future models. Specifically, real-time measurements of local electrical conductivity in dog-bone samples during FS are essential to improving simulation accuracy. Such refinements are crucial for capturing the nuanced effects of electrochemical reduction on microstructural evolution in flash-sintered samples.

2. Although the identified densification enhancing factor and the proposed mechanism in this study align with the theoretical predictions and existing literature, direct experimental validation remains critical. Observing the hypothesized star-shaped pore structure under ultrafast heating conditions would be invaluable in confirming the proposed theory. However, significant practical challenges arise due to much longer cooling period during UHS compared to the heating time. This prolonged cooling allows surface diffusion to continue, altering the microstructure and making it difficult to accurately observe the true microstructure during UHS. Future work could focus on developing alternative ultra-fast firing technologies that incorporate rapid cooling capabilities. For instance, a quenching dilatometer modified for ceramic samples could capture the microstructure as it exists during UHS. Additionally, traditional tools such as SEM may prove insufficient for studying the star-shaped porosity, as 2D images cannot fully capture the degree of pore spheroidization. Techniques like atomic force microscopy (AFM), which can measure the dihedral angle in 3D with higher resolution, may provide a more suitable alternative.
3. While the modified SOVS model in this study accounted for the physical effect of pore shape, it remains largely phenomenological and is based on an idealized 2D grain-packing model. In reality, the pore structure during UHS is inherently more intricate, requiring advanced simulation tools to accurately model 3D microstructural evolution under ultra-high heating rates. Future work should explore more sophisticated microscopic simulation methods, such as Monte Carlo simulations and phase field modeling. These approaches could enable detailed tracking of microstructural changes in 3D and provide deeper insights into the densification and grain growth mechanisms during ECAS.

9 References

[1] S. Grasso, Y. Sakka, G. Maizza, Electric current activated/assisted sintering (ECAS): a review of patents 1906-2008, Sci. Technol. Adv. Mater. 10 (2009) 53001. https://doi.org/10.1088/1468-6996/10/5/053001.

[2] M. Cologna, B. Rashkova, R. Raj, Flash Sintering of Nanograin Zirconia in <5 s at 850°C, Journal of the American Ceramic Society 93 (2010) 3556–3559. https://doi.org/10.1111/j.1551-2916.2010.04089.x.

[3] C. Wang, W. Ping, Q. Bai, H. Cui, R. Hensleigh, R. Wang, A.H. Brozena, Z. Xu, J. Dai, Y. Pei, C. Zheng, G. Pastel, J. Gao, X. Wang, H. Wang, J.-C. Zhao, B. Yang, X.R. Zheng, J. Luo, Y. Mo, B. Dunn, L. Hu, A general method to synthesize and sinter bulk ceramics in seconds, Science 368 (2020) 521–526. https://doi.org/10.1126/science.aaz7681.

[4] R.M. German, Sintering theory and practice, Wiley New York, New York, 1996.

[5] M.N. Rahaman, Sintering of Ceramics, CRC Press, Boca Raton, Fla., 2007.

[6] J. Pan, Modelling sintering at different length scales, International Materials Reviews 48 (2003) 69–85. https://doi.org/10.1179/095066002225010209.

[7] K. Tsuruta, A. Omeltchenko, R.K. Kalia, P. Vashishta, Early stages of sintering of silicon nitride nanoclusters: a molecular-dynamics study on parallel machines, Europhys. Lett. 33 (1996) 441–446. https://doi.org/10.1209/epl/i1996-00359-2.

[8] H. Zhu, Sintering processes of two nanoparticles: A study by molecular dynamics simulations, Philosophical Magazine Letters 73 (1996) 27–33. https://doi.org/10.1080/095008396181073.

[9] P. Hohenberg, W. Kohn, Inhomogeneous Electron Gas, Phys. Rev. 136 (1964) B864-B871. https://doi.org/10.1103/PhysRev.136.B864.

[10] M. Orio, D.A. Pantazis, F. Neese, Density functional theory, Photosynth. Res. 102 (2009) 443–453. https://doi.org/10.1007/s11120-009-9404-8.

[11] A.A. Mahmood, M. Elektorowicz, A Review of Discrete Element Method Research on Particulate Systems, IOP Conf. Ser.: Mater. Sci. Eng. 136 (2016) 12034. https://doi.org/10.1088/1757-899X/136/1/012034.

[12] A. Wonisch, O. Guillon, T. Kraft, M. Moseler, H. Riedel, J. Rödel, Stress-induced anisotropy of sintering alumina: Discrete element modelling and experiments, Acta Materialia 55 (2007) 5187–5199. https://doi.org/10.1016/j.actamat.2007.05.038.

[13] F. Parhami, R.M. McMeeking, A network model for initial stage sintering, Mechanics of Materials 27 (1998) 111–124. https://doi.org/10.1016/S0167-6636(97)00034-3.

[14] M. Anderson, D. Srolovitz, G. Grest, P. Sahni, Computer simulation of grain growth—I. Kinetics, Acta Metallurgica 32 (1984) 783–791. https://doi.org/10.1016/0001-6160(84)90151-2.

[15] V. Tikare, J.D. Cawley, Numerical simulation of grain growth in liquid phase sintered materials-I. Model, Acta Materialia 46 (1998) 1333–1342. https://doi.org/10.1016/S1359-6454(97)00269-3.

[16] V. Tikare, M.A. Miodownik, E.A. Holm, Three‐Dimensional Simulation of Grain Growth in the Presence of Mobile Pores, Journal of the American Ceramic Society 84 (2001) 1379–1385. https://doi.org/10.1111/j.1151-2916.2001.tb00845.x.

[17] L. Zhang, M.R. Tonks, P.C. Millett, Y. Zhang, K. Chockalingam, B. Biner, Phase-field modeling of temperature gradient driven pore migration coupling with thermal conduction, Computational Materials Science 56 (2012) 161–165. https://doi.org/10.1016/j.commatsci.2012.01.002.

[18] Y.U. Wang, Computer modeling and simulation of solid-state sintering: A phase field approach, Acta Materialia 54 (2006) 953–961. https://doi.org/10.1016/j.actamat.2005.10.032.

[19] A. Kazaryan, Y. Wang, B.R. Patton, Generalized phase field approach for computer simulation of sintering: incorporation of rigid-body motion, Scripta Materialia 41 (1999) 487–492. https://doi.org/10.1016/S1359-6462(99)00179-7.

[20] R.L. Coble, Initial Sintering of Alumina and Hematite, Journal of the American Ceramic Society 41 (1958) 55–62. https://doi.org/10.1111/j.1151-2916.1958.tb13519.x.

[21] W.D. Kingery, M. Berg, Study of the Initial Stages of Sintering Solids by Viscous Flow, Evaporation-Condensation, and Self-Diffusion, Journal of Applied Physics 26 (1955) 1205–1212. https://doi.org/10.1063/1.1721874.

[22] G.C. Kuczynski, Self-diffusion in sintering of metallic particles, JOM 1 (1949) 169–178. https://doi.org/10.1007/BF03398090.

[23] R.L. Coble, Sintering Crystalline Solids. I. Intermediate and Final State Diffusion Models, Journal of Applied Physics 32 (1961) 787–792. https://doi.org/10.1063/1.1736107.

[24] D.L. Johnson, A General Model for the Intermediate Stage of Sintering, Journal of the American Ceramic Society 53 (1970) 574–577. https://doi.org/10.1111/j.1151-2916.1970.tb15969.x.

[25] W. Beere, The second stage sintering kinetics of powder compacts, Acta Metallurgica 23 (1975) 139–145. https://doi.org/10.1016/0001-6160(75)90079-6.

[26] S.C. Coleman, W.B. Beeré, The sintering of open and closed porosity in UO 2, Philosophical Magazine 31 (1975) 1403–1413. https://doi.org/10.1080/00318087508228691.

[27] J.D. Hansen, R.P. Rusin, M.-H. Teng, D.L. Johnson, Combined‐Stage Sintering Model, Journal of the American Ceramic Society 75 (1992) 1129‐1135. https://doi.org/10.1111/j.1151-2916.1992.tb05549.x.

[28] H. Su, D.L. Johnson, Master Sintering Curve: A Practical Approach to Sintering, Journal of the American Ceramic Society 79 (1996) 3211–3217. https://doi.org/10.1111/j.1151-2916.1996.tb08097.x.

[29] S. Shima, M. Oyane, Plasticity theory for porous metals, International Journal of Mechanical Sciences 18 (1976) 285–291. https://doi.org/10.1016/0020-7403(76)90030-8.

[30] R.J. Green, A plasticity theory for porous solids, International Journal of Mechanical Sciences 14 (1972) 215–224. https://doi.org/10.1016/0020-7403(72)90063-X.

[31] V.V. Skorohod, Rheological basis of the theory of sintering, Naukova Dumka, Kiev, 1972.

[32] E.A. Olevsky, Theory of sintering: from discrete to continuum, Materials Science and Engineering: R: Reports 23 (1998) 41–100. https://doi.org/10.1016/S0927-796X(98)00009-6.

[33] R.K. Bordia, G.W. Scherer, On constrained sintering—I. Constitutive model for a sintering body, Acta Metallurgica 36 (1988) 2393–2397. https://doi.org/10.1016/0001-6160(88)90189-7.

[34] C. van Nguyen, S. K. Sistla, S. van Kempen, N. A. Giang, A. Bezold, C. Broeckmann, F. Lange, A comparative study of different sintering models for Al_2O_3, J. Ceram. Soc. Japan 124 (2016) 301–312. https://doi.org/10.2109/jcersj2.15257.

[35] K. Shinagawa, Micromechanical modelling of viscous sintering and a constitutive equation with sintering stress, Computational Materials Science 13 (1999) 276–285. https://doi.org/10.1016/S0927-0256(98)00132-3.

[36] M. Ashby, HIP 6.0: Background Reading, Sintering and Isostatic Pressing Diagrams, Cambridge University Report, 1990.

[37] J.E. Burke, D. Turnbull, Recrystallization and grain growth, Progress in Metal Physics 3 (1952) 220–292. https://doi.org/10.1016/0502-8205(52)90009-9.

[38] M. Hillert, On the theory of normal and abnormal grain growth, Acta Metallurgica 13 (1965) 227–238. https://doi.org/10.1016/0001-6160(65)90200-2.

[39] D. Sohrabi Baba Heidary, M. Lanagan, C.A. Randall, Contrasting energy efficiency in various ceramic sintering processes, Journal of the European Ceramic Society 38 (2018) 1018–1029. https://doi.org/10.1016/j.jeurceramsoc.2017.10.015.

[40] M. Biesuz, S. Grasso, V.M. Sglavo, What's new in ceramics sintering? A short report on the latest trends and future prospects, Current Opinion in Solid State and Materials Science 24 (2020) 100868. https://doi.org/10.1016/j.cossms.2020.100868.

[41] R.M. German (Ed.), Sintering With External Pressure, Elsevier, 2014.

[42] H.V. Atkinson, S. Davies, Fundamental aspects of hot isostatic pressing: An overview. Metall Mater Trans A 31, 2981–3000 (2000). https://doi.org/10.1007/s11661-000-0078-2.

[43] M.N. Rahaman (Ed.), Ceramic processing and sintering, 2nd ed., Marcel Dekker, New York, 2003.

[44] K. Watari, H.J. Hwang, M. Toriyama, S. Kanzaki, Effective Sintering Aids for Low-temperature Sintering of AlN Ceramics, J. Mater. Res. 14 (1999) 1409–1417. https://doi.org/10.1557/JMR.1999.0191.

[45] K. Nur, T.P. Mishra, J.G.P. Da Silva, J. Gonzalez-Julian, M. Bram, O. Guillon, Influence of powder characteristics on cold sintering of nano-sized ZnO with density above 99 %, Journal of the European Ceramic Society 41 (2021) 2648–2662. https://doi.org/10.1016/j.jeurceramsoc.2020.11.007.

[46] M. Biesuz, V.M. Sglavo, Flash sintering of ceramics, Journal of the European Ceramic Society 39 (2019) 115–143. https://doi.org/10.1016/j.jeurceramsoc.2018.08.048.

[47] T.P. Mishra, R.R.I. Neto, R. Raj, O. Guillon, M. Bram, Current-rate flash sintering of gadolinium doped ceria: Microstructure and Defect generation, Acta Materialia 189 (2020) 145–153. https://doi.org/10.1016/j.actamat.2020.02.036.

[48] M.A. Janney, H.D. Kimrey, Diffusion-Controlled Processes in Microwave-Fired Oxide Ceramics, MRS Proc. 189 (1990) 215. https://doi.org/10.1557/PROC-189-215.

[49] R. Raj, M. Cologna, Prette, A.L.G. Sglavo, V. Patent US 20130085055 A1, US 20130085055 A1, 2013.

[50] O. Guillon, J. Gonzalez-Julian, B. Dargatz, T. Kessel, G. Schierning, J. Räthel, M. Herrmann, Field-Assisted Sintering Technology/Spark Plasma Sintering: Mechanisms, Materials, and Technology Developments, Adv. Eng. Mater. 16 (2014) 830–849. https://doi.org/10.1002/adem.201300409.

[51] Z.A. Munir, U. Anselmi-Tamburini, M. Ohyanagi, The effect of electric field and pressure on the synthesis and consolidation of materials: A review of the spark plasma sintering method, J Mater Sci 41 (2006) 763–777. https://doi.org/10.1007/s10853-006-6555-2.

[52] D.M. Hulbert, A. Anders, J. Andersson, E.J. Lavernia, A.K. Mukherjee, A discussion on the absence of plasma in spark plasma sintering, Scripta Materialia 60 (2009) 835–838. https://doi.org/10.1016/j.scriptamat.2008.12.059.

[53] D.M. Hulbert, A. Anders, D.V. Dudina, J. Andersson, D. Jiang, C. Unuvar, U. Anselmi-Tamburini, E.J. Lavernia, A.K. Mukherjee, 2008. The absence of plasma in “spark plasma sintering”. Journal of Applied Physics 104, 033305. https://doi.org/10.1063/1.2963701.

[54] M. Kermani, J. Dong, M. Biesuz, Y. Linx, H. Deng, V.M. Sglavo, M.J. Reece, C. HU, S. Grasso, Ultrafast high-temperature sintering (UHS) of fine grained α-Al2O3, Journal of the European Ceramic Society 41 (2021) 6626–6633. https://doi.org/10.1016/j.jeurceramsoc.2021.05.056.

[55] J. Dong, V. Pouchly, M. Biesuz, V. Tyrpekl, M. Vilémová, M. Kermani, M. Reece, C. HU, S. Grasso, Thermally-insulated ultra-fast high temperature sintering (UHS) of zirconia: A master sintering curve analysis, Scripta Materialia 203 (2021) 114076. https://doi.org/10.1016/j.scriptamat.2021.114076.

[56] A. Krell, P. Blank, H. Ma, T. Hutzler, M.P.B. Bruggen, R. Apetz, Transparent Sintered Corundum with High Hardness and Strength, Journal of the American Ceramic Society 86 (2003) 12–18. https://doi.org/10.1111/j.1151-2916.2003.tb03270.x.

[57] E. Zapata-Solvas, D. Gómez-García, A. Domínguez-Rodríguez, R.I. Todd, Ultra-fast and energy-efficient sintering of ceramics by electric current concentration, Sci. Rep. 5 (2015) 8513. https://doi.org/10.1038/srep08513.

[58] M. Bram, A.M. Laptev, T.P. Mishra, K. Nur, M. Kindelmann, M. Ihrig, J.G. Da Pereira Silva, R. Steinert, H.P. Buchkremer, A. Litnovsky, F. Klein, J. Gonzalez-Julian, O. Guillon, Application of Electric Current‐Assisted Sintering Techniques for the Processing of Advanced Materials, Adv. Eng. Mater. 22 (2020) 2000051. https://doi.org/10.1002/adem.202000051.

[59] O. Guillon, W. Rheinheimer, M. Bram, 2023. A Perspective on Emerging and Future Sintering Technologies of Ceramic Materials. Adv Eng Mater 25, 2201870. https://doi.org/10.1002/adem.202201870.

[60] R.I. Todd, E. Zapata-Solvas, R.S. Bonilla, T. Sneddon, P.R. Wilshaw, Electrical characteristics of flash sintering: thermal runaway of Joule heating, Journal of the European Ceramic Society 35 (2015) 1865–1877. https://doi.org/10.1016/j.jeurceramsoc.2014.12.022.

[61] Y. Zhang, J.-I. Jung, J. Luo, Thermal runaway, flash sintering and asymmetrical microstructural development of ZnO and ZnO–Bi2O3 under direct currents, Acta Materialia 94 (2015) 87–100. https://doi.org/10.1016/j.actamat.2015.04.018.

[62] D. Yadav, R. Raj, The onset of the flash transition in single crystals of cubic zirconia as a function of electric field and temperature, Scripta Materialia 134 (2017) 123–127. https://doi.org/10.1016/j.scriptamat.2017.02.015.

[63] R. Raj, M. Cologna, J.S.C. Francis, Influence of Externally Imposed and Internally Generated Electrical Fields on Grain Growth, Diffusional Creep, Sintering and Related Phenomena in Ceramics, Journal of the American Ceramic Society 94 (2011) 1941–1965. https://doi.org/10.1111/j.1551-2916.2011.04652.x.

[64] M. Schie, S. Menzel, J. Robertson, R. Waser, R.A. de Souza, Field-enhanced route to generating anti-Frenkel pairs in HfO2, Phys. Rev. Materials 2 (2018). https://doi.org/10.1103/PhysRevMaterials.2.035002.

[65] J.-M. Lebrun, C.S. Hellberg, S.K. Jha, W.M. Kriven, A. Steveson, K.C. Seymour, N. Bernstein, S.C. Erwin, R. Raj, In‐situ measurements of lattice expansion related to defect generation during flash sintering, J Am Ceram Soc 100 (2017) 4965‐4970. https://doi.org/10.1111/jace.15071.

[66] M. Jongmanns, D.E. Wolf, Element‐specific displacements in defect‐enriched TiO 2 Indication of a flash sintering mechanism, J Am Ceram Soc 103 (2020) 589‐596. https://doi.org/10.1111/jace.16696.

[67] M. Jongmanns, R. Raj, D.E. Wolf, Generation of Frenkel defects above the Debye temperature by proliferation of phonons near the Brillouin zone edge, New J. Phys. 20 (2018) 93013. https://doi.org/10.1088/1367-2630/aadd5a.

[68] D. Yadav, R. Raj, Two unique measurements related to flash experiments with yttria‐stabilized zirconia, J Am Ceram Soc 100 (2017) 5374‐5378. https://doi.org/10.1111/jace.15114.

[69] J.A. Downs, Mechanisms of Flash Sintering in Cubic Zirconia. Doctoral thesis, University of Trento, Trento, Italy, 2013.

[70] J. Janek, Electrochemical blackening of yttria-stabilized zirconia – morphological instability of the moving reaction front front, Solid State Ionics 116 (1999) 181–195. https://doi.org/10.1016/S0167-2738(98)00415-9.

[71] M. Biesuz, L. Pinter, T. Saunders, M. Reece, J. Binner, V.M. Sglavo, S. Grasso, Investigation of Electrochemical, Optical and Thermal Effects during Flash Sintering of 8YSZ, Materials (Basel) 11 (2018). https://doi.org/10.3390/ma11071214.

[72] D.L. Johnson (Ed.), Ultra-Rapid Sintering: Volume 16 Sintering and Heterogeneous Catalysis, Springer US, Boston, MA, 1984.

[73] C. Manière, C. Harnois, S. Marinel, Role of microstructure reactivity and surface diffusion in explaining flash (ultra-rapid) sintering kinetics, Journal of the European Ceramic Society 43 (2023) 2057–2068. https://doi.org/10.1016/j.jeurceramsoc.2022.12.006.

[74] W. Ji, B. Parker, S. Falco, J.Y. Zhang, Z.Y. Fu, R.I. Todd, Ultra-fast firing: Effect of heating rate on sintering of 3YSZ, with and without an electric field, Journal of the European Ceramic Society 37 (2017) 2547–2551. https://doi.org/10.1016/j.jeurceramsoc.2017.01.033.

[75] X. L. Phuah, J. Jian, H. Wang, X. Wang, X. Zhang, H. Wang, Ultra-high heating rate effects on the sintering of ceramic nanoparticles: an in situ TEM study. Materials Research Letters, 9.9 (2021): 373-381. https://doi.org/10.1080/21663831.2021.1927878.

[76] T.P. Mishra, S. Wang, C. Lenser, D. Jennings, M. Kindelmann, W. Rheinheimer, C. Broeckmann, M. Bram, O. Guillon, Ultra-fast high-temperature sintering of strontium

titanate, Acta Materialia 231 (2022) 117918. https://doi.org/10.1016/j.actamat.2022.117918.

[77] E.A. Olevsky, S. Kandukuri, L. Froyen, Consolidation enhancement in spark-plasma sintering: Impact of high heating rates, Journal of Applied Physics 102 (2007) 114913. https://doi.org/10.1063/1.2822189.

[78] R. Chaim, G. Chevallier, A. Weibel, C. Estournès, Grain growth during spark plasma and flash sintering of ceramic nanoparticles: a review, J Mater Sci 53 (2018) 3087–3105. https://doi.org/10.1007/s10853-017-1761-7.

[79] U. Anselmi-Tamburini, J.E. Garay, Z.A. Munir, Fundamental investigations on the spark plasma sintering/synthesis process, Materials Science and Engineering: A 407 (2005) 24–30. https://doi.org/10.1016/j.msea.2005.06.066.

[80] M. Yu, S. Grasso, R. Mckinnon, T. Saunders, M.J. Reece, Review of flash sintering: materials, mechanisms and modelling, Advances in Applied Ceramics 116 (2017) 24–60. https://doi.org/10.1080/17436753.2016.1251051.

[81] C.E.J. Dancer, Flash sintering of ceramic materials, Materials Research Express 3 (2016) 102001. https://doi.org/10.1088/2053-1591/3/10/102001.

[82] M. Cologna, J.S. Francis, R. Raj, Field assisted and flash sintering of alumina and its relationship to conductivity and MgO-doping, Journal of the European Ceramic Society 31 (2011) 2827–2837. https://doi.org/10.1016/j.jeurceramsoc.2011.07.004.

[83] T.P. Mishra, Electric Field Assisted Sintering of Gadolinium-doped Ceria. PhD Thesis, Forschungszentrum Jülich GmbH, 2020.

[84] S.K. Jha, K. Terauds, J.-M. Lebrun, R. Raj, Beyond flash sintering in 3 mol % yttria stabilized zirconia, J. Ceram. Soc. Japan 124 (2016) 283–288. https://doi.org/10.2109/jcersj2.15248.

[85] J.S.C. Francis, R. Raj, Influence of the Field and the Current Limit on Flash Sintering at Isothermal Furnace Temperatures, J. Am. Ceram. Soc. 96 (2013) 2754–2758. https://doi.org/10.1111/jace.12472.

[86] R. Raj, Analysis of the Power Density at the Onset of Flash Sintering, J. Am. Ceram. Soc. 99 (2016) 3226–3232. https://doi.org/10.1111/jace.14178.

[87] T.P. Mishra, V. Avila, R.R.I. Neto, M. Bram, O. Guillon, R. Raj, On the role of Debye temperature in the onset of flash in three oxides, Scripta Materialia 170 (2019) 81–84. https://doi.org/10.1016/j.scriptamat.2019.05.030.

[88] P. Debye, Zur Theorie der spezifischen Wärmen, Annalen der Physik 344 (1912) 789–839. https://doi.org/10.1002/andp.19123441404.

[89] P. Kumar M K, D. Yadav, J.-M. Lebrun, R. Raj, Flash sintering with current rate: A different approach, J Am Ceram Soc 93 (2018) 3556. https://doi.org/10.1111/jace.16037.

[90] T. Yamamoto, Improvements in Flash Sintering for Practical Application, Mater. Trans. 64 (2023) 2059–2068. https://doi.org/10.2320/matertrans.MT-Y2023003.

[91] R. Muccillo, M. Kleitz, E.N. Muccillo, Flash grain welding in yttria stabilized zirconia, Journal of the European Ceramic Society 31 (2011) 1517–1521. https://doi.org/10.1016/j.jeurceramsoc.2011.02.030.

[92] R. Baraki, S. Schwarz, O. Guillon, Effect of Electrical Field/Current on Sintering of Fully Stabilized Zirconia, J. Am. Ceram. Soc. 95 (2012) 75–78. https://doi.org/10.1111/j.1551-2916.2011.04980.x.

[93] S. Grasso, T. Saunders, H. Porwal, B. Milsom, A. Tudball, M. Reece, Flash Spark Plasma Sintering (FSPS) of α and β SiC, J. Am. Ceram. Soc. 99 (2016) 1534–1543. https://doi.org/10.1111/jace.14158.

[94] S. Grasso, T. Saunders, H. Porwal, O. Cedillos‐Barraza, D.D. Jayaseelan, W.E. Lee, M.J. Reece, Flash Spark Plasma Sintering (FSPS) of Pure ZrB2, J. Am. Ceram. Soc. 97 (2014) 2405‐2408. https://doi.org/10.1111/jace.13109.

[95] M. Biesuz, A. Galotta, A. Motta, M. Kermani, S. Grasso, J. Vontorová, V. Tyrpekl, M. Vilémová, V.M. Sglavo, Speedy bioceramics: Rapid densification of tricalcium phosphate by ultrafast high-temperature sintering, Mater. Sci. Eng. C Mater. Biol. Appl. 127 (2021) 112246. https://doi.org/10.1016/j.msec.2021.112246.

[96] R.-F. Guo, H.-R. Mao, Z.-T. Zhao, P. Shen, Ultrafast high-temperature sintering of bulk oxides, Scripta Materialia 193 (2021) 103–107. https://doi.org/10.1016/j.scriptamat.2020.10.045.

[97] M. Kermani, C. HU, S. Grasso, From pit fire to Ultrafast High-temperature Sintering (UHS): A review on ultrarapid consolidation, Ceramics International 49 (2023) 4017–4029. https://doi.org/10.1016/j.ceramint.2022.11.091.

[98] E. de Bona, C. Manière, V.M. Sglavo, M. Biesuz, Ultrafast high-temperature sintering (UHS) of ZrB2-based materials, Journal of the European Ceramic Society 44 (2024) 567–573. https://doi.org/10.1016/j.jeurceramsoc.2023.09.007.

[99] Y. Sun, L. Zhao, R.-F. Guo, P. Shen, Cr3C2 assisted ultrafast high-temperature sintering of TiC, Journal of the European Ceramic Society 43 (2023) 5458–5465. https://doi.org/10.1016/j.jeurceramsoc.2023.05.031.

[100] A. Alemayehu, M. Biesuz, K.Y. Javan, A. Tkach, P.M. Vilarinho, V.M. Sglavo, V. Tyrpekl, Ultrafast high-temperature sintering of gadolinia-doped ceria, Journal of the European Ceramic Society 43 (2023) 4837–4843. https://doi.org/10.1016/j.jeurceramsoc.2023.04.025.

[101] J. Wu, M. Kermani, D. Zhu, J. Li, Y. Lin, C. HU, S. Grasso, Carbon free ultra-fast high temperature sintering of translucent zirconia, Scripta Materialia 210 (2022) 114476. https://doi.org/10.1016/j.scriptamat.2021.114476.

[102] P. Jiang, G. Du, Y. Shi, F. She, P. Guo, G. Qian, X. Lu, F. Xie, X. Lu, Ultrafast sintering of Na3Zr2Si2PO12 solid electrolyte for long lifespan solid-state sodium ion batteries, Chemical Engineering Journal 451 (2023) 138771. https://doi.org/10.1016/j.cej.2022.138771.

[103] Le Fu, J. Wu, S.K.M. Sathyanath, B. Wang, K. Leifer, H. Engqvist, S. Grasso, W. Xia, Far from equilibrium ultrafast high‐temperature sintering of ZrO 2 –SiO 2 nanocrystalline glass–ceramics, J Am Ceram Soc. 106 (2023) 4005–4012. https://doi.org/10.1111/jace.19055.

[104] Z. Lin, X. Zhao, C. Wang, Q. Dong, J. Qian, G. Zhang, A.H. Brozena, X. Wang, S. He, W. Ping, G. Chen, Y. Pei, C. Zheng, B.C. Clifford, M. Hong, Y. Wu, B. Yang, J. Luo, P. Albertus, L. Hu, Rapid Pressureless Sintering of Glasses, Small 18 (2022) e2107951. https://doi.org/10.1002/smll.202107951.

[105] L. Spiridigliozzi, G. Dell'Agli, S. Esposito, P. Rivolo, S. Grasso, V.M. Sglavo, M. Biesuz, Ultra-fast high-temperature sintering (UHS) of Ce0.2Zr0.2Y0.2Gd0.2La0.2O2−δ fluorite-structured entropy-stabilized oxide (F-ESO), Scripta Materialia 214 (2022) 114655. https://doi.org/10.1016/j.scriptamat.2022.114655.

[106] R.-X. Luo, M. Kermani, Z.-L. Guo, J. Dong, C.-F. Hu, F. Zuo, S. Grasso, B.-B. Jiang, G.-L. Nie, Z.-Q. Yan, Q. Wang, Y.-L. Gan, F.-P. He, H.-T. Lin, Ultrafast high-temperature sintering of silicon nitride: A comparison with the state-of-the-art techniques, Journal of the European Ceramic Society 41 (2021) 6338–6345. https://doi.org/10.1016/j.jeurceramsoc.2021.06.021.

[107] W. Ping, C. Wang, R. Wang, Q. Dong, Z. Lin, A.H. Brozena, J. Dai, J. Luo, L. Hu, Printable, high-performance solid-state electrolyte films, Sci. Adv. 6 (2020). https://doi.org/10.1126/sciadv.abc8641.

[108] H. Xie, M. Qin, M. Hong, J. Rao, M. Guo, J. Luo, L. Hu, Rapid liquid phase-assisted ultrahigh-temperature sintering of high-entropy ceramic composites, Sci. Adv. 8 (2022) eabn8241. https://doi.org/10.1126/sciadv.abn8241.

[109] M. Ihrig, T.P. Mishra, W.S. Scheld, G. Häuschen, W. Rheinheimer, M. Bram, M. Finsterbusch, O. Guillon, Li7La3Zr2O12 solid electrolyte sintered by the ultrafast high-temperature method, Journal of the European Ceramic Society 41 (2021) 6075–6079. https://doi.org/10.1016/j.jeurceramsoc.2021.05.041.

[110] J. Wu, Y. Lin, M. Kermani, C. HU, S. Grasso, Ultra-fast high temperature sintering (UHS) of Li1.5Al0.5Ge1.5P3O12 electrolyte: A rationalization of the heating schedule, Ceramics International 48 (2022) 6356–6362. https://doi.org/10.1016/j.ceramint.2021.11.178.

[111] M. Kermani, D. Zhu, J. Li, J. Wu, Y. Lin, Z. Dai, C. HU, S. Grasso, Ultra-fast High-temperature Sintering (UHS) of translucent alumina, Open Ceramics 9 (2022) 100202. https://doi.org/10.1016/j.oceram.2021.100202.

[112] Y. Liang, S. Xiang, X. Zhang, Ultrafast high-temperature heating in air, Journal of the European Ceramic Society 42 (2022) 4030–4039. https://doi.org/10.1016/j.jeurceramsoc.2022.03.015.

[113] F. Zuo, Q. Wang, Z.-Q. Yan, M. Kermani, S. Grasso, G.-L. Nie, B.-B. Jiang, F.-P. He, H.-T. Lin, L.-G. Wang, Upscaling Ultrafast High-Temperature Sintering (UHS) to consolidate large-sized and complex-shaped ceramics, Scripta Materialia 221 (2022) 114973. https://doi.org/10.1016/j.scriptamat.2022.114973.

[114] W. Xu, A. Maksymenko, S. Hasan, J.J. Meléndez, E. Olevsky, Effect of external electric field on diffusivity and flash sintering of 8YSZ: A molecular dynamics study, Acta Materialia 206 (2021) 116596. https://doi.org/10.1016/j.actamat.2020.116596.

[115] F.B. Sweidan, H.J. Ryu, Kinetic Monte Carlo simulations of the sintering microstructural evolution in density graded stainless steel fabricated by SPS, Materials Today Communications 26 (2021) 101863. https://doi.org/10.1016/j.mtcomm.2020.101863.

[116] K. Vikrant, H. Wang, A. Jana, H. Wang, R.E. García, Flash sintering incubation kinetics, npj Comput Mater 6 (2020) 115. https://doi.org/10.1038/s41524-020-00359-7.

[117] J.A. Bejarano-Palma, B.M. Moshtaghioun, F.L. Cumbrera, D. Gómez-García, Flash sintering can induce an anisotropic microstructure in ceramics. A phase field modeling insight, Scripta Materialia 247 (2024) 116123. https://doi.org/10.1016/j.scriptamat.2024.116123.

[118] J.A. Bejarano-Palma, B.M. Moshtaghioun, F.L. Cumbrera, D. Gómez-García, On the role of the electric field in the last-stage sintering of ceramics: A phase-field modelling approach, Acta Materialia 262 (2024) 119422. https://doi.org/10.1016/j.actamat.2023.119422.

[119] Norimat, https://www.norimat.com/en/engemini-digital-twin, accessed: 2023.

[120] R. Raj, Joule heating during flash-sintering, Journal of the European Ceramic Society 32 (2012) 2293–2301. https://doi.org/10.1016/j.jeurceramsoc.2012.02.030.

[121] W. Qin, H. Majidi, J. Yun, K. van Benthem, Electrode Effects on Microstructure Formation During FLASH Sintering of Yttrium-Stabilized Zirconia, J. Am. Ceram. Soc. 99 (2016) 2253–2259. https://doi.org/10.1111/jace.14234.

[122] J.G. Pereira da Silva, J.-M. Lebrun, H.A. Al-Qureshi, R. Janssen, R. Raj, Temperature Distributions During Flash Sintering of 8% Yttria-Stabilized Zirconia, J. Am. Ceram. Soc. 98 (2015) 3525–3528. https://doi.org/10.1111/jace.13786.

[123] S. Grasso, Y. Sakka, N. Rendtorff, C. Hu, G. Maizza, H. Borodianska, O. Vasylkiv, Modeling of the temperature distribution of flash sintered zirconia, J. Ceram. Soc. Japan 119 (2011) 144–146. https://doi.org/10.2109/jcersj2.119.144.

[124] R. Serrazina, P.M. Vilarinho, A.M. Senos, L. Pereira, I.M. Reaney, J.S. Dean, Modelling the particle contact influence on the Joule heating and temperature distribution during FLASH sintering, Journal of the European Ceramic Society 40 (2020) 1205–1211. https://doi.org/10.1016/j.jeurceramsoc.2019.12.015.

[125] G. Bernard-Granger, A. Addad, G. Fantozzi, G. Bonnefont, C. Guizard, D. Vernat, Spark plasma sintering of a commercially available granulated zirconia powder: Comparison with hot-pressing, Acta Materialia 58 (2010) 3390–3399. https://doi.org/10.1016/j.actamat.2010.02.013.

[126] G. Bernard-Granger, C. Guizard, Spark plasma sintering of a commercially available granulated zirconia powder: I. Sintering path and hypotheses about the

mechanism(s) controlling densification, Acta Materialia 55 (2007) 3493–3504. https://doi.org/10.1016/j.actamat.2007.01.048.

[127] E.A. Olevsky *, B. Kushnarev, A. Maximenko, V. Tikare, M. Braginsky, Modelling of anisotropic sintering in crystalline ceramics, Philosophical Magazine 85 (2005) 2123–2146. https://doi.org/10.1080/14786430412331331989.

[128] E.A. Olevsky, D.V. Dudina, Field-Assisted Sintering, Springer International Publishing, Cham, 2018.

[129] E. Olevsky, L. Froyen, Constitutive modeling of spark-plasma sintering of conductive materials, Scripta Materialia 55 (2006) 1175–1178. https://doi.org/10.1016/j.scriptamat.2006.07.009.

[130] G. Lee, E.A. Olevsky, C. Manière, A. Maximenko, O. Izhvanov, C. Back, J. McKittrick, Effect of electric current on densification behavior of conductive ceramic powders consolidated by spark plasma sintering, Acta Materialia 144 (2018) 524–533. https://doi.org/10.1016/j.actamat.2017.11.010.

[131] J.G.P. Da Silva, H.A. Al-Qureshi, F. Keil, R. Janssen, A dynamic bifurcation criterion for thermal runaway during the flash sintering of ceramics, Journal of the European Ceramic Society 36 (2016) 1261–1267. https://doi.org/10.1016/j.jeurceramsoc.2015.11.048.

[132] K.S. Arya, A. Eqbal, P. Rai, D. Yadav, T. Chakrabarti, 2022. Investigation on the role of Joule heating on flash sintering using a combined experimental and modeling approach. J Am Ceram Soc., jace.18584. https://doi.org/10.1111/jace.18584.

[133] Y. Li, R. Torchio, S. Falco, P. Alotto, Z. Huang, R.I. Todd, Promoting core/surface homogeneity during flash sintering of 3YSZ ceramic by current path management: experimental and modelling studies, Journal of the European Ceramic Society 41 (2021) 6649–6659. https://doi.org/10.1016/j.jeurceramsoc.2021.06.001.

[134] W. Ji, J. Zhang, W. Wang, Z. Fu, R.I. Todd, The microstructural origin of rapid densification in 3YSZ during ultra-fast firing with or without an electric field, Journal of the European Ceramic Society 40 (2020) 5829–5836. https://doi.org/10.1016/j.jeurceramsoc.2020.07.027.

[135] W. Ji, H. Xu, W. Wang, Z. Fu, Sintering dense nanocrystalline 3YSZ ceramics without grain growth by plastic deformation as dominating mechanism, Ceramics International 45 (2019) 9363–9367. https://doi.org/10.1016/j.ceramint.2018.07.228.

[136] A.M. Locci, R. Orrù, G. Cao, Modeling of Electric Current Assisted Sintering: An extended fluid-like approach for the description of powders rheological behavior, Chemical Engineering Research and Design 154 (2020) 283–302. https://doi.org/10.1016/j.cherd.2019.12.001.

[137] T.P. Mishra, R. Singh, R. Mücke, J. Malzbender, M. Bram, O. Guillon, R. Vaßen, Influence of Process Parameters on the Aerosol Deposition (AD) of Yttria-Stabilized Zirconia Particles, J Therm Spray Tech 30 (2021) 488–502. https://doi.org/10.1007/s11666-020-01101-x.

[138] T. Morimoto, M. Nagai, Y. Minowa, M. Ashida, Y. Yokotani, Y. Okuyama, Y. Kani, Microscopic ion migration in solid electrolytes revealed by terahertz time-domain spectroscopy, Nat. Commun. 10 (2019) 2662. https://doi.org/10.1038/s41467-019-10501-9.

[139] M. Bäurer, H. Kungl, M.J. Hoffmann, Influence of Sr/Ti Stoichiometry on the Densification Behavior of Strontium Titanate, J Am Ceram Soc. 92 (2009) 601–606. https://doi.org/10.1111/j.1551-2916.2008.02920.x.

[140] W. Rheinheimer, M. Bäurer, H. Chien, G.S. Rohrer, C.A. Handwerker, J.E. Blendell, M.J. Hoffmann, The equilibrium crystal shape of strontium titanate and its relationship to the grain boundary plane distribution, Acta Materialia 82 (2015) 32–40. https://doi.org/10.1016/j.actamat.2014.08.065.

[141] Fabian Lemke, Wolfgang Rheinheimer, Michael J. Hoffmann, Sintering and grain growth in SrTiO3: impact of defects on kinetics, J. Ceram. Soc. Japan 124 (2016) P4-1-P4-4. https://doi.org/10.2109/jcersj2.124.P4-1.

[142] J. ZHAO, First-principles study of ferroelectricity in oxide superlattices. PhD thesis, France, 2013.

[143] Y. Xu, Y. Liang, Q. He, R. Xu, D. Chen, X. Xu, H. Hu, Review of doping SrTiO3 for photocatalytic applications, Bull Mater Sci 46 (2023). https://doi.org/10.1007/s12034-022-02826-x.

[144] K. Maca, V. Pouchly, A.R. Boccaccini, Sintering densification curve: A practical approach for its construction from dilatometric shrinkage data, Sci Sintering 40 (2008) 117–122. https://doi.org/10.2298/SOS0802117M.

[145] M.I. MENDELSON, Average Grain Size in Polycrystalline Ceramics, J American Ceramic Society 52 (1969) 443–446. https://doi.org/10.1111/j.1151-2916.1969.tb11975.x.

[146] P. Morgan, Carbon fibers and their composites, Taylor & Francis, Boca Raton, 2005. https://doi.org/10.1201/9781420028744.

[147] D.R. Gaskell, D.E. Laughlin, Introduction to the thermodynamics of materials, Sixth edition, CRC Press Taylor & Francis Group CRC Press is an imprint of Taylor & Francis Group an informa business, Boca Raton, New York, 2018.

[148] C.Y. Ho, R.W. Powell, P.E. Liley, Thermal Conductivity of the Elements, Journal of Physical and Chemical Reference Data 1 (1972) 279–421. https://doi.org/10.1063/1.3253100.

[149] G.K. White, S.J. Collocott, Heat Capacity of Reference Materials: Cu and W, Journal of Physical and Chemical Reference Data 13 (1984) 1251–1257. https://doi.org/10.1063/1.555728.

[150] O. Okhay, A. Tkach, Impact of Graphene or Reduced Graphene Oxide on Performance of Thermoelectric Composites, C 7 (2021) 37. https://doi.org/10.3390/c7020037.

[151] D. de Ligny, Richet, High-temperature heat capacity and thermal expansion of SrTiO3 and SrZrO3 perovskites, Phys. Rev. B Condens. Matter 53 (1996) 3013–3022. https://doi.org/10.1103/PhysRevB.53.3013.

[152] ABAQUS 5.8 Theory Manual, Hibbitt, Karlsson & Sorensen Inc, Pawtucket, USA, 1998.

[153] A. Zavaliangos, J. Zhang, M. Krammer, J.R. Groza, Temperature evolution during field activated sintering, Materials Science and Engineering: A 379 (2004) 218–228. https://doi.org/10.1016/j.msea.2004.01.052.

[154] J. Zhang, Z. Wang, T. Jiang, L. Xie, C. Sui, R. Ren, J. Qiao, K. Sun, Densification of 8 mol% yttria-stabilized zirconia at low temperature by flash sintering technique for solid oxide fuel cells, Ceramics International 43 (2017) 14037–14043. https://doi.org/10.1016/j.ceramint.2017.07.137.

[155] H. Tanaka, S. Sawai, K. Morimoto, K. Hisano, Measurement of Spectral Emissivity and Thermal Conductivity of Zirconia by Thermal Radiation Calorimetry, Journal of Thermal Analysis and Calorimetry 64 (2001) 867–872. https://doi.org/10.1023/A:1011538022439.

[156] A.J. Wright, C. Huang, M.J. Walock, A. Ghoshal, M. Murugan, J. Luo, Sand corrosion, thermal expansion, and ablation of medium‐ and high‐entropy

compositionally complex fluorite oxides, J American Ceramic Society 104 (2021) 448 – 462. https://doi.org/10.1111/jace.17448.

[157] J. Zhang, C. Lenser, N.H. Menzler, O. Guillon, Comparison of solid oxide fuel cell (SOFC) electrolyte materials for operation at 500 °C, Solid State Ionics 344 (2020) 115138. https://doi.org/10.1016/j.ssi.2019.115138.

[158] W.R. Wade, L. Aeronaut, Lab. NASA, Technical note 4206 (1958).

[159] K. Shinagawa, Finite Element Simulation of Sintering process (Microscopic Modelling of Powder Compacts and Constitutive Equation for Sintering), JSME international journal. Ser. A, Mechanics and material engineering 39 (1996) 565–572. https://doi.org/10.1299/jsmea1993.39.4_565.

[160] M. Renaux, D. Méresse, J. Pellé, A. Thuault, C. Morin, C. Nivot, C. Courtois, Mechanical modelling of microwave sintering and experimental validation on an alumina powder, Journal of the European Ceramic Society 41 (2021) 6617–6625. https://doi.org/10.1016/j.jeurceramsoc.2021.06.013.

[161] M.W. Reiterer, K.G. Ewsuk, J.G. Arguello, An Arrhenius-Type Viscosity Function to Model Sintering Using the Skorohod-Olevsky Viscous Sintering Model Within a Finite-Element Code, J American Ceramic Society 89 (2006) 1930–1935. https://doi.org/10.1111/j.1551-2916.2006.01041.x.

[162] R.L. Coble, A Model for Boundary Diffusion Controlled Creep in Polycrystalline Materials, Journal of Applied Physics 34 (1963) 1679–1682. https://doi.org/10.1063/1.1702656.

[163] A.L. Maximenko, E.A. Olevsky, Effective diffusion coefficients in solid-state sintering, Acta Materialia 52 (2004) 2953–2963. https://doi.org/10.1016/j.actamat.2004.02.042.

[164] M.N. Rahaman (Ed.), Sintering of ceramics, CRC; London Taylor & Francis [distributor], Boca Raton, Fla., 2008.

[165] C. Manière, C. Harnois, S. Marinel, Porous stage assessment of pressure assisted sintering modeling parameters: a ceramic identification method insensitive to final stage grain growth disturbance, Acta Materialia 211 (2021) 116899. https://doi.org/10.1016/j.actamat.2021.116899.

[166] J.M. VIEIRA, R.J. BROOK, Kinetics of Hot-Pressing: The Semilogarithmic Law, Journal of the American Ceramic Society 67 (1984) 245–249. https://doi.org/10.1111/j.1151-2916.1984.tb18840.x.

[167] G. Kerbart, C. Harnois, S. Marinel, C. Manière, Modeling the sintering trajectories of MgAl2O4 Spinel, Scripta Materialia 203 (2021) 114048. https://doi.org/10.1016/j.scriptamat.2021.114048.

[168] F. Lemke, W. Rheinheimer, M.J. Hoffmann, Sintering and grain growth in SrTiO3: impact of defects on kinetics, J. Ceram. Soc. Japan 124 (2016) 346–353. https://doi.org/10.2109/jcersj2.15265.

[169] Y. Kimura, T. Kushi, A. Unemoto, K. Amezawa, T. Kawada, Influence of Aging on Mechanical Properties of Yttria-Doped Zirconia, Ceramics 1 (2018) 287–303. https://doi.org/10.3390/ceramics1020023.

[170] X. Wang, A. Atkinson, Microstructure evolution in thin zirconia films: Experimental observation and modelling, Acta Materialia 59 (2011) 2514–2525. https://doi.org/10.1016/j.actamat.2010.12.056.

[171] S.K. Sistla, T.P. Mishra, Y. Deng, A. Kaletsch, M. Bram, C. Broeckmann, Polarity‐induced grain growth of gadolinium‐doped ceria under field‐assisted sintering technology/spark plasma sintering (FAST/SPS) conditions, J. Am. Ceram. Soc. 104 (2021) 1978‐1996. https://doi.org/10.1111/jace.17614.

[172] T.K. Gupta, R.L. Coble, Sintering of ZnO: I, Densification and Grain Growth*, J Am Ceram Soc. 51 (1968) 521–525. https://doi.org/10.1111/j.1151-2916.1968.tb15679.x.

[173] M.F. Yan, Microstructural control in the processing of electronic ceramics, Materials Science and Engineering 48 (1981) 53–72. https://doi.org/10.1016/0025-5416(81)90066-5.

[174] P.-L. Chen, I.-W. Chen, Role of Defect Interaction in Boundary Mobility and Cation Diffusivity of CeO2, J Am Ceram Soc. 77 (1994) 2289–2297. https://doi.org/10.1111/j.1151-2916.1994.tb04596.x.

[175] A. Kabir, H. Zhang, V. Esposito, Mass diffusion phenomena in cerium oxide, in: Cerium Oxide (CeO_2): Synthesis, Properties and Applications, Elsevier, 2020, pp. 169–210.

[176] S. Ubenthiran, M. Thanihaichelvan, R. Singh, Effect of Air and Argon Sintering Atmospheres on Properties and Hydrothermal Aging Resistance of Y-TZP Ceramics, J. of Materi Eng and Perform 27 (2018) 3574–3580. https://doi.org/10.1007/s11665-018-3428-1.

[177] W. Rheinheimer, J.P. Parras, J.-H. Preusker, R.A. de Souza, M.J. Hoffmann, Grain growth in strontium titanate in electric fields: The impact of space‐charge on the

grain‐boundary mobility, J Am Ceram Soc 102 (2019) 3779‐3790. https://doi.org/10.1111/jace.16217.

[178] M.P. Harmer, R.J. Brook, Fast Firing-Microstructural Benefits, J. Br. Ceram. Soc. 5 (1981) 147–148.

[179] B.-N. Kim, T.S. Suzuki, K. Morita, H. Yoshida, Y. SAKKA, H. Matsubara, Densification kinetics during isothermal sintering of 8YSZ, Journal of the European Ceramic Society 36 (2016) 1269–1275. https://doi.org/10.1016/j.jeurceramsoc.2015.11.041.

[180] K. Matsui, K. Tanaka, T. Yamakawa, M. Uehara, N. Enomoto, J. Hojo, Sintering Kinetics at Isothermal Shrinkage: II, Effect of Y 2 O 3 Concentration on the Initial Sintering Stage of Fine Zirconia Powder, J American Ceramic Society 90 (2007) 443–447. https://doi.org/10.1111/j.1551-2916.2006.01440.x.

[181] G. Suárez, N.M. Rendtorff, A.N. Scian, E.F. Aglietti, Isothermal sintering kinetic of 3YTZ and 8YSZ: Cation diffusion, Ceramics International 39 (2013) 261–268. https://doi.org/10.1016/j.ceramint.2012.06.020.

[182] R.R. Ingraci Neto, K.J. McClellan, D.D. Byler, E. Kardoulaki, Controlled current-rate AC flash sintering of uranium dioxide, Journal of Nuclear Materials 547 (2021) 152780. https://doi.org/10.1016/j.jnucmat.2021.152780.

[183] Y. Lin, N. Luo, E. Quattrocchi, F. Ciucci, J. Wu, M. Kermani, J. Dong, C. HU, S. Grasso, Ultrafast high-temperature sintering (UHS) of Li1.3Al0.3Ti1.7(PO4)3, Ceramics International 47 (2021) 21982–21987. https://doi.org/10.1016/j.ceramint.2021.04.216.

[184] O. Guillon, J. Langer, Master sintering curve applied to the Field-Assisted Sintering Technique, J Mater Sci 45 (2010) 5191–5195. https://doi.org/10.1007/s10853-010-4556-7.

[185] G. Sethi, S.J. Park, J.L. Johnson, R.M. German, Linking homogenization and densification in W–Ni–Cu alloys through master sintering curve (MSC) concepts, International Journal of Refractory Metals and Hard Materials 27 (2009) 688–695. https://doi.org/10.1016/j.ijrmhm.2008.11.005.

[186] J. Hötzer, V. Rehn, W. Rheinheimer, M.J. Hoffmann, B. Nestler, Phase-field study of pore-grain boundary interaction, J. Ceram. Soc. Japan 124 (2016) 329–339. https://doi.org/10.2109/jcersj2.15266.

[187] V. Rehn, J. Hötzer, W. Rheinheimer, M. Seiz, C. Serr, B. Nestler, Phase-field study of grain growth in porous polycrystals, Acta Materialia 174 (2019) 439–449. https://doi.org/10.1016/j.actamat.2019.05.059.

[188] R.J. Brook, Pore-Grain Boundary Interactions and Grain Growth, J Am Ceram Soc. 52 (1969) 56–57. https://doi.org/10.1111/j.1151-2916.1969.tb12664.x.

[189] K. Vikrant, W. Rheinheimer, H. Sternlicht, M. Bäurer, R.E. García, Electrochemically-driven abnormal grain growth in ionic ceramics, Acta Materialia 200 (2020). https://doi.org/10.1016/j.actamat.2020.08.027.

[190] W. Rheinheimer, M. Bäurer, C.A. Handwerker, J.E. Blendell, M.J. Hoffmann, Growth of single crystalline seeds into polycrystalline strontium titanate: Anisotropy of the mobility, intrinsic drag effects and kinetic shape of grain boundaries, Acta Materialia 95 (2015) 111–123. https://doi.org/10.1016/j.actamat.2015.05.019.

[191] H.-Y. Chang, K.-S. Liu, I.-N. Lin, Modification of PTCR behavior of (Sr0·2Ba0·8)TiO3 materials by post-heat treatment after microwave sintering, Journal of the European Ceramic Society 16 (1996) 63–70. https://doi.org/10.1016/0955-2219(95)00081-X.

[192] L.C. Pathak, S.K. Mishra, D. Bhattacharya, K.L. Chopra, Synthesis and Sintering Characteristics of SrTiO3 Powder Prepared by Coprecipitation Process, Transactions of the Materials Research Society of Japan 24 (1999) 525–529.

[193] R. Raj, D.E. Wolf, C.N. Yamada, S.K. Jha, J.-M. Lebrun, On the confluence of ultrafast high‐temperature sintering and flash sintering phenomena, J Am Ceram Soc. 106 (2023) 3983‐3998. https://doi.org/10.1111/jace.19070.

[194] S.K. Jha, R. Raj, The Effect of Electric Field on Sintering and Electrical Conductivity of Titania, J. Am. Ceram. Soc. 97 (2014) 527–534. https://doi.org/10.1111/jace.12682.

[195] S.-W. Kim, S.G. Kim, J.-I. Jung, S.-J.L. Kang, I.-W. Chen, Enhanced Grain Boundary Mobility in Yttria-Stabilized Cubic Zirconia under an Electric Current, J. Am. Ceram. Soc. 94 (2011) 4231–4238. https://doi.org/10.1111/j.1551-2916.2011.04800.x.

[196] S. Bhandari, T.P. Mishra, O. Guillon, D. Yadav, M. Bram, Accessing the role of Joule heating on densification during flash sintering of YSZ, Scripta Materialia 211 (2022) 114508. https://doi.org/10.1016/j.scriptamat.2022.114508.

10 Appendix

10.1 Thermophysical properties

Table 10.1 Temperature dependent properties of 8YSZ used in simulations: Specific heat, Young's modulus, and the coefficient of thermal expansion (CTE)

Temperature [°C]	Specific Heat [J/kgK]	Temperature [°C]	Young's Modulus [GPa]	Temperature [°C]	CTE [1/K]
44	528.13	28	229.62	40	7.20E-06
80	521.91	85	228.64	78	7.95E-06
100	528.49	106	228.08	114	8.32E-06
120	534.16	161	226.52	148	8.56E-06
140	543.65	197	225.56	182	8.67E-06
180	555.54	242	223.47	218	8.80E-06
200	561.92	285	216.84	253	8.91E-06
250	577.91	339	209.56	288	9.02E-06
300	596.55	399	193.55	323	9.12E-06
350	588.90	456	184.31	358	9.21E-06
400	594.07	493	175.29	393	9.29E-06
450	616.17	563	162.99	428	9.37E-06
500	626.99	640	151.58	463	9.43E-06
550	635.83	698	154.42	498	9.49E-06
600	644.68	825	166.08	533	9.55E-06
650	633.80	889	160.52	568	9.61E-06
700	669.53	1014	173.71	603	9.67E-06
750	677.61	1094	179.44	638	9.74E-06
800	675.40	1119	178.95	673	9.80E-06
850	684.17			708	9.86E-06
900	696.87			743	9.93E-06
950	697.42			778	9.99E-06
1000	716.94			813	1.01E-05
1100	776.95			848	1.01E-05
1200	848.78			883	1.02E-05
1300	871.70			918	1.03E-05
1400	877.01			953	1.03E-05

				988	1.04E-05
				1023	1.05E-05
				1058	1.05E-05
				1093	1.06E-05
				1128	1.07E-05
				1163	1.07E-05
				1198	1.08E-05
				1220	1.08E-05

Table 10.2 Temperature dependent properties of 8YSZ used in simulations: Thermal conductivity and elctrical conductivity [157]. Thermal conductivity is also density dependent, and both property data above 900°C are extrapolated from the values below 900°C.

Relative Density [-]	Temperature [°C]	Thermal Conductivity [W/mK]	Temperature [°C]	Electrical Conductivity [S/m]
0.60	25	0.82	299	0.00E+00
0.60	100	0.80	300	4.96E-04
0.60	200	0.82	320	1.03E-03
0.60	300	0.86	340	2.02E-03
0.60	400	0.86	360	3.72E-03
0.60	500	0.92	380	6.71E-03
0.60	600	0.99	400	1.17E-02
0.60	700	1.06	420	1.96E-02
0.60	799	1.12	440	3.12E-02
0.60	900	1.28	460	4.92E-02
0.60	1000	1.37	480	7.49E-02
0.60	1100	1.51	500	1.11E-01
0.60	1200	1.65	550	2.74E-01
0.60	1300	1.81	600	5.84E-01
0.60	1400	1.99	650	1.11E+00
0.60	1500	2.18	700	2.02E+00
0.65	26	1.01	750	2.88E+00
0.65	100	0.99	800	4.11E+00
0.65	300	1.05	850	5.41E+00

0.65	500	1.10	900	6.34E+00
0.65	903	1.37	950	7.62E+00
0.83	25	1.54	1000	9.26E+00
0.83	200	1.47	1050	1.10E+01
0.83	400	1.50	1100	1.30E+01
0.83	500	1.69	1150	1.50E+01
0.83	600	1.76	1200	1.72E+01
0.83	700	1.88	1250	1.94E+01
0.83	800	2.16	1300	2.18E+01
0.97	20	2.16	1350	2.43E+01
0.97	100	2.01	1400	2.68E+01
0.97	200	2.06	1450	2.94E+01
0.97	300	2.11	1500	3.20E+01
0.97	400	2.18		
0.97	500	2.32		
0.97	600	2.46		
0.97	700	2.61		
0.97	800	2.86		

Table 10.3 Temperature dependent properties of $SrTiO_3$ used in simulations: Thermal conductivity and specific heat [150,151]. The thermal conductivity data above 900°C are extrapolated from the values below 900°C.

Temperature [°C]	Thermal Conductivity [W/mK]	Temperature [°C]	Specific Heat [J/kgK]
26	9.09	25	530.00
101	7.63	127	544.99
201	6.34	327	588.59
301	5.46	527	610.39
400	4.83	727	626.74
501	4.33	927	643.09
927	3.08	1127	653.99
1227	2.58	1327	664.89
1527	2.24	1527	675.79
1727	2.06		
2027	1.85		

Table 10.4 Temperature dependent properties of carbon felt used in simulations: Specific heat [147], thermal conductivity [146], and electrical conductivity. The electrical conductivity was experimentally measured using UHS test runs without any sample at the maximum currents ranging from 5 to 24 A, and the temperatures were estimated through pyrometer and thermocouple measurements.

Temperature [°C]	Specific Heat [J/kgK]	Temperature [°C]	Thermal Conductivity [W/mK]	Temperature [°C]	Electrical Conductivity [S/m]
29	673.80	13	0.06	593	897.77
63	777.95	66	0.08	695	949.74
86	831.90	126	0.09	785	1002.51
113	897.34	180	0.09	869	1034.85
129	935.89	243	0.11	1548	1145.72
161	1012.99	309	0.12	1721	1170.49
188	1066.86	374	0.13	1908	1191.10
211	1109.23	454	0.15	2093	1208.50
235	1159.27	542	0.17	2297	1223.70
268	1213.05	681	0.20		
301	1270.75	748	0.22		
334	1316.79	825	0.24		
367	1362.92	949	0.27		
405	1412.79	1020	0.29		
440	1462.74	1128	0.32		
475	1501.04	1199	0.34		
506	1523.94	1267	0.37		
540	1577.72	1380	0.41		
569	1596.70	1476	0.47		
607	1631.09	1599	0.54		
636	1665.64	1703	0.61		
671	1700.02	1781	0.66		
706	1711.26	1854	0.72		
742	1745.65	1921	0.77		
779	1760.72	1991	0.83		
815	1787.44	2053	0.89		
851	1806.34	2103	0.93		
892	1836.82	2190	1.02		

939	1847.89	2230	1.07		
966	1870.79	2270	1.11		
1009	1881.94	2305	1.16		
1038	1893.18	2341	1.21		
1069	1900.59	2365	1.26		
1095	1911.83	2396	1.33		
1125	1923.15				
1166	1926.48				
1204	1957.04				
1239	1956.62				
1282	1967.70				
1327	1971.03				

Table 10.5 Temperature dependent properties of Cu used in simulations: Thermal conductivity and specific heat [148,149]

Temperature [°C]	Thermal Conductivity [W/mK]	Temperature [°C]	Specific Heat [J/kgK]
27.90	387.00	27.90	384.00
57.90	386.00	57.90	387.00
107.90	385.00	107.90	393.00
157.90	384.00	157.90	399.00
207.90	383.00	207.90	404.00
257.90	381.00	257.90	409.00
307.90	379.00	307.90	414.00
357.90	377.00	357.90	418.00
407.90	374.00	407.90	422.00
457.90	371.00	457.90	426.00
507.90	368.00	507.90	430.00
557.90	364.00	557.90	433.00
607.90	360.00	607.90	438.00
657.90	357.00	657.90	442.00
707.90	353.00	707.90	447.00
757.90	350.00	757.90	452.00
807.90	347.00	807.90	459.00

857.90	343.00	857.90	466.00
907.90	340.00	907.90	475.00
957.90	337.00	957.90	486.00
1007.90	334.00	1007.90	498.00

10.2 Determination of densification kinetic parameters

The fitting strategy for determining the densification parameters for FS is as follows: First, density curves were fitted for each dwell time, as represented by black dashed lines in **Figure 10.1a**. Density values at 1000°C, 1100°C and 1200°C were extracted from these curves for subsequent analysis. Next, the extracted relative densities were plotted against dwell time at each temperature to determine the densification rate, as shown in **Figure 10.1b**. Finally, the parameter m and the apparent activation energy for densification Q_d were determined. This was achieved using linear regression plots, as illustrated in **Figure 10.1c** and **Figure 10.1d,** following the procedure described in section 6.1.3.

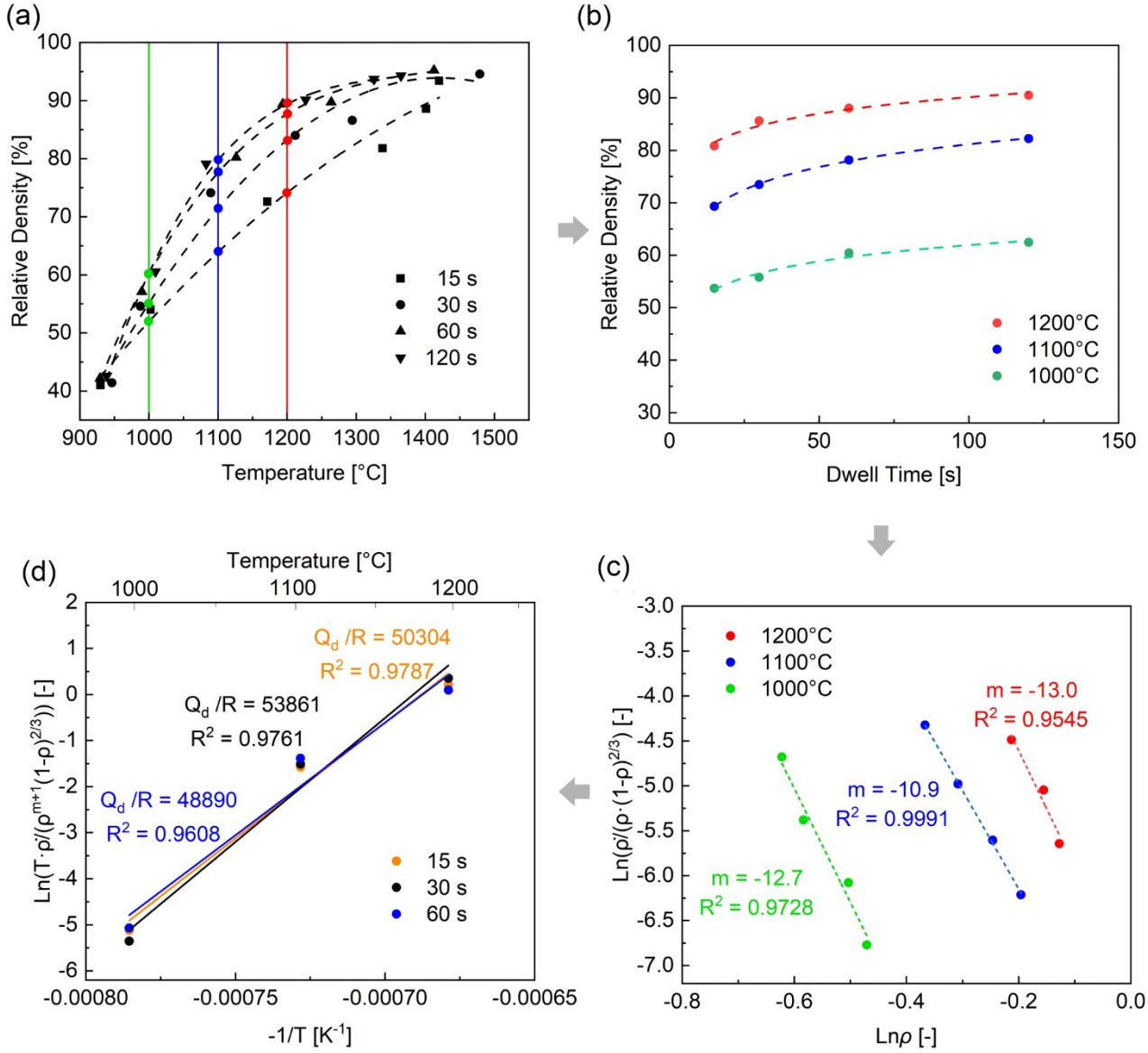

Figure 10.1 Determination of densification kinetic parameters for FS: (a) densification curve fitting and data extraction at 1000°C, 1100°C, and 1200°C; (b) extracted relative densities as function of dwell times; (c) determination of parameter m; (d) determination of parameter Q_d.